

MICROBIAL COMMUNITY COMPOSITION AND COMPETITIVE DYNAMICS WITHIN SQUID  
SYMBIOSES

Stephanie Smith

A dissertation submitted to the faculty at the University of North Carolina at Chapel Hill in partial fulfillment  
of the requirements for the degree of Doctor of Philosophy in the Department of Marine Sciences in the  
College of Arts and Sciences.

Chapel Hill  
2023

Approved by:

Alecia Septer

Scott Gifford

Andreas Teske

Todd Gray

Mark Mandel

© 2023  
Stephanie Smith  
ALL RIGHTS RESERVED

## ABSTRACT

Stephanie Smith: Microbial community composition and competitive dynamics within squid symbioses  
(Under the direction of Alecia Septer)

Animals evolved surrounded by bacteria, resulting in widespread symbioses in which host and symbiont often form specialized partnerships that are essential for host development, reproduction, or survival. During host-colonization, bacteria are often forced together within a physical space, providing opportunities for competitive and cooperative interactions that ultimately shape the microbial community within a given host. The first three chapters of this dissertation use the light organ symbiont *Vibrio fischeri* as a model bacterium for studying these complex microbial interactions. *V. fischeri* encodes a strain-specific T6SS, a contact-mediated killing mechanism found broadly distributed among host-associated bacteria. I designed a microscopy workflow to quantify contact-dependent competition at the single-cell level and applied this technique to study competitive interactions between lethal and non-lethal *V. fischeri* strains *in vitro*. Then, I used this assay in combination with a subcellular biomechanical model for T6SS to investigate killing dynamics within lethal-lethal interactions. This study revealed that strains with the ability to activate T6SS more quickly under host-like conditions outcompete slower-activating strains, even if both isolates are lethal. In addition to T6SS, *V. fischeri* encodes both conserved and strain-specific mechanisms for horizontal gene transfer (HGT). Using an experimental evolution assay designed to detect transfer of selectable chromosomal markers, I found that *V. fischeri* exchanges chromosomal DNA in coculture in a manner inconsistent with any HGT mechanism that has been previously described in *V. fischeri*. Although squid light organs represent an important model for bacterial interactions, we currently lack a fundamental understanding of the natural microbial community across other squid body sites. In the final chapter of this dissertation, I characterized the microbial community of mantle, gill, sub-mantle tissue, and accessory nidamental glands of wild-caught *Lolliguncula brevis* squid using a combination of culture-based techniques, microscopy, and amplicon sequencing. I found that *L. brevis* hosts multiple

species of culturable *Vibrios*, a core community of *Bradyrhizobium* that is conserved across body sites, and a surprisingly diverse gill community. Taken together, this dissertation provided new tools for evaluating interactions between symbiotic bacteria, and also introduced *L. brevis* as an exciting system that warrants further study into the complexity of squid microbiomes.

## **ACKNOWLEDGEMENTS**

To Alecia, thank you for taking a chance on me. No one has ever believed in me the way that you do, and I don't really know how to express how much your mentorship has meant to me over the years. You've pushed me when you know I can do more, given me pep talks when I need them, and allowed me every opportunity to dream big in my research. You're a mentor and a friend who has been a part of every big life event that has happened to me since I was a baby undergrad who didn't know anything about microbiology and you took me in anyway. I appreciate you. Keep proving them wrong every single day.

To my committee members, Scott Gifford, Mark Mandel, Todd Gray, and Andreas Teske, thank you for all of your ideas, support, and feedback over the years. Your thoughtful questions have shaped this dissertation into something I am very proud of.

To my wife, Kaci Dilday, thank you is not enough. Who would have guessed that we would be married before I finished my PhD? Thank you for being patient while I write this dissertation, for so many late-night office nights, for listening to me grumble about going in for experiments, and for loving me even when I'm stressed and sad. You've taught me how good life can be and I can't wait for our next big adventure. I love you endlessly.

To Lauren Speare, Mel Cohn, Travis Wilson, Mark Ciesielski, and John Malito, I could not have gotten through this PhD without you. I am so grateful for your friendship, comradery, and support. You've all been with me for some really hard times and some really great times, and we've managed to keep having fun through it all. Lauren, no one will ever understand my science the way that you do. Mel, you're a part of the family and I appreciate all of the many days you've let me drag you to Lanza's to write and gossip. Travis, thank you for always being the person that I can count on for advice, a board game, and a good time. Mark and John, I am so grateful that we've managed to stay as close as we have even though you've both moved away – I live vicariously through you both. I love you all so much.

To Garrett and Andrea, thank you for the many, many times you have listened to me give practice talks and complain about my research not going the way I expected. You are both amazing friends and scientists, and I can't wait to see where we all end up next.

To all of the many undergraduate researchers who have worked with me over the years, you have truly made this dissertation possible. In particular, Coby Dorsey, Christina Lim, Iris Chien, and Brian Smith made significant contributions to these dissertation chapters both in troubleshooting assays and collecting data. I am proud of all of you and am honored to say that we collaborated on these projects.

To Lanza's, thanks for all the coffee and for putting all of your tables next to outlets. Most of this dissertation was written while sipping on a latte.

To Gooby (Yodi), Chonkey-Monkey (Oliver), Biscuit (Sketti), and Pretty-Pretty Princess (Mouse), you're the best coworkers I could possibly ask for. Any portion of this dissertation that wasn't written while sipping on a latte was written with one of you in my lap. You're perfect, never change.

## TABLE OF CONTENTS

LIST OF TABLES.....	x
LIST OF FIGURES .....	xi
INTRODUCTION.....	1
CHAPTER 1 – Quantification of interbacterial competition using single-cell fluorescence imaging <sup>1</sup> .....	4
1.1 Introduction .....	4
1.2 Protocol.....	5
1.3 Representative Results .....	12
1.4 Discussion. ....	15
1.5 Figures. ....	18
CHAPTER 2 – A subcellular biomechanical model for T6SS dynamics reveals winning competitive strategies <sup>2</sup> .....	22
2.1 Introduction. ....	22
2.2 Results... ..	26
Competition outcomes differ due to intraspecific variations in T6SS killing dynamics.....	26
Quantifying strain-specific differences in T6SS activation dynamics. ....	28
Model predictions and comparison with experimental data. ....	32
Spatial environment of competition affects target survival.....	34
Cost determines the competitive fitness of T6SS production strategies. ....	35
2.3 Discussion. ....	37
2.4 Material and Methods. ....	39
Media and growth conditions. ....	39

Coincubation assays. ....	39
Fluorescence microscopy.....	39
2.5 Figures.....	41
CHAPTER 3 – <i>Vibrio fischeri</i> coculture results in horizontal gene transfer .....	47
3.1 Introduction. ....	47
3.2 Results.....	51
Experimental Evolution Assay Design. ....	51
Transfer frequency is not dependent on the location of chromosomal markers in ES114.....	51
Selectable markers are transferred between ES114 and distantly related <i>Vibrios</i> (KB8).....	53
Conditions for transfer are not consistent with any reported HGT mechanisms in <i>V. fischeri</i> .....	53
3.3 Discussion. ....	56
3.4 Material and Methods. ....	59
Media and growth conditions. ....	59
Molecular techniques. ....	59
Experimental evolution assays. ....	60
3.5 Figures... ..	61
CHAPTER 4 – Characterization of the <i>Loliguncula brevis</i> microbiome across body sites.....	66
4.1 Introduction. ....	66
4.2 Results... ..	68
<i>L. brevis</i> collection and identification. ....	68
<i>L. brevis</i> dissection and body site selection .....	69
Multiple <i>Vibrio</i> species are cultured from <i>L. brevis</i> gill and sub-mantle tissue .....	69
Sub-mantle tissue isolates are unable to colonize <i>E. scolopes</i> .....	71
Sub-mantle tissue does not have characteristics typical of light organs.....	71



Amplicon Sequencing .....	74
Body site selection and sample collection. ....	74
Bacterial community bioinformatics pipeline. ....	74
Community composition based on <i>hsp60</i> amplicon sequences. ....	75
<i>hsp60</i> rarefaction and alpha diversity measures. ....	76
<i>L. brevis</i> samples are distinct from seawater and kitcon samples at the community-level. ....	76
<i>L. brevis</i> hosts a distinct, conserved microbial community. ....	77
Core microbiome of <i>L. brevis</i> is dominated by <i>Nitrobacteraceae</i> , <i>Vibrionaceae</i> , and unidentified bacteria. ....	77
4.3 Discussion. ....	79
4.4 Materials and Methods. ....	81
Animal collection. ....	81
Bacterial isolation from squid. ....	82
Isolate identification based on <i>hsp60</i> sequence. ....	82
Luminescence curves of <i>L. brevis</i> isolates. ....	82
Luminescence measurements of <i>L. brevis</i> tissue. ....	82
Microscopy of <i>L. brevis</i> sub-mantle tissue. ....	83
4.5 Figures... ..	84
CONCLUDING REMARKS.....	102
REFERENCES.....	103

## LIST OF TABLES

Table 3.1. Transfer frequency summary across experiments. ....	65
Table 4.1. Squid COI NCBI BLAST hits. ....	98
Table 4.2. Squid sample breakdown. ....	99
Table 4.3. Cultured isolates <i>hsp60</i> NCBI BLAST hits.....	100
Table 4.4. <i>hsp60</i> read counts tracked through DADA2 processing steps. ....	101

## LIST OF FIGURES

Figure 1.1. Agarose pad preparation and slide setup for coincubation assays .....	18
Figure 1.2. Time lapse images of coincubation spots in either crowded or dispersed conditions .....	19
Figure 1.3. FIJI analysis workflow .....	20
Figure 1.4. Sample data for assessing whether target strain is inhibited .....	21
Figure 2.1. Schematics of experimental and computational systems used in this study .....	41
Figure 2.2. Competition outcomes vary due to intraspecific variations in T6SS killing dynamics .....	42
Figure 2.3. <i>V. fischeri</i> exhibits strain-specific T6SS dynamics over time during surface activation.....	43
Figure 2.4. The effect of activation rate on lethal vs. target competition is consistent when other T6SS parameters are perturbed .....	44
Figure 2.5. Target strains survive longer when competing against slow activating lethal strains in a range expansion .....	45
Figure 2.6. Competitive outcomes and surviving mechanisms are affected by the cost of T6SS production.....	46
Figure 3.1. Experimental evolution assay .....	61
Figure 3.2. Transfer frequency is not dependent on the location of chromosomal markers in ES114 .....	62
Figure 3.3. <i>V. fischeri</i> exchanges selectable markers with <i>Vibrio</i> sp. KB8 .....	63
Figure 3.4. Conditional requirements for DNA transfer in <i>V. fischeri</i> .....	64
Figure 4.1. <i>L. brevis</i> collection and identification .....	84
Figure 4.2. <i>L. brevis</i> dissection and body site selection.....	85
Figure 4.3. Phylogeny of <i>Vibrionaceae</i> species cultured from <i>L. brevis</i> gill and sub-mantle tissue. ....	86
Figure 4.4. Vibrios isolated from <i>L. brevis</i> sub-mantle tissue are unable to colonize juvenile <i>E. scolopes</i> .....	87
Figure 4.5. Sub-mantle tissue is not characteristic of other light organs .....	88
Figure 4.6. Amplicon sequencing and bioinformatic processing workflow.....	89
Figure 4.7. Community composition based on hsp60 amplicon sequences .....	90
Figure 4.8. Rarefaction and alpha diversity measures for <i>hsp60</i> amplicon samples.....	91
Figure 4.9. <i>L. brevis</i> samples are distinct from seawater and kitcon samples at the community -level. ....	92
Figure 4.10. <i>L. brevis</i> hosts a distinct, conserved microbial community.....	93
Figure 4.11. Core microbiome of <i>L. brevis</i> .....	94

Figure 4.12. Top 100 taxa across all <i>hsp60</i> amplicon samples.....	96
---	----

## INTRODUCTION

Symbioses can be defined as “the living together of unlike organisms” [1], and as the first life forms on earth, microbes are central to many of these interactions. Nearly all animals and plants have evolved in the presence of microbes, resulting in strong symbiotic associations that provide essential functions to host reproduction, development, or survival. Some bacterial symbionts provide critical nutrients to their host; for example, some species of *Osedax* worms rely so completely on their endosymbionts for nutrition that they lack a traditional mouth or gut [2, 3]. Eukaryotes lack the ability to biologically fix nitrogen, and certain species of marine sponges, insects, and legumes rely on symbiotic bacteria as their primary source of fixed nitrogen [4-6]. Symbioses are often mutually beneficial, and host environments provide an important niche for symbionts to obtain nutrients and to exchange genetic information. Many of these symbioses are horizontally transmitted, meaning that with each new generation of hosts, bacteria must be acquired from the surrounding environment.

During this colonization process environmental bacteria are often forced into close physical contact with one another, providing ample opportunities for both cooperative and competitive interactions as they vie for prime spots within a host niche. One such mechanism is the type VI secretion system (T6SS): a contact-dependent killing mechanism by which a lethal cell injects deadly toxins into neighboring cells [7-9]. T6SSs are found in an estimated 25% of gram-negative bacteria and are broadly distributed among both beneficial and pathogenic microbes [10-14]. T6SS is thought to have been initially acquired from phage, and the T6SS apparatus resembles an inverted phage that can be used to deliver proteins into adjacent bacteria, eukaryotic host cells, or to release proteins into the environment [15]. Close-quarters doesn't always mean warfare in bacteria – physical contact with other cells also means that host-colonization sites are a reservoir of genetic diversity and important drivers of bacterial gene transfer [16, 17]. Traditional mechanisms for horizontal gene transfer are often classified as either transduction, transformation, or conjugation. While transduction and transformation involve the uptake of

DNA from viruses or free DNA from the surrounding environment, conjugation requires physical contact between live cells [18, 19]. Although most early work in conjugation focused on plasmid transfer between bacterial cells, we now know that some conjugative mechanisms result in extensive transfer of chromosomal DNA between bacteria [20-23].

The Hawaiian bobtail squid, *Euprymna scolopes*, has long been used as a simple model for understanding host-colonization processes [24-27]. Most of this research has centered around the light organ, a symbiotic structure found broadly in fish and squid, including *E. scolopes* [28, 29]. Bacteria housed in these organs are thought to provide light that the host uses for predator deterrence, prey attraction, or communication [26, 27, 30]. Despite making up only < 0.1% of the bacterial seawater population, *V. fischeri* is the only species of bacteria known to colonize the light organs of *E. scolopes*, and a great body of research has gone into understanding factors that drive such a specialized partnership [31-37].

*V. fischeri* encodes a strain-specific T6SS that has been shown to activate under host-like viscosity conditions and to be an important factor in host-colonization outcomes in the *E. scolopes* light organ [38, 39]. Genomic analysis of more than 73 squid isolates revealed that the *V. fischeri* T6SS is encoded within a genomic island with high genomic plasticity [14]. Moreover, recent work identified the transcriptional regulator TasR and structural proteins TssM and TssA as being required for activation of T6SS in *V. fischeri* [40]. All three of these proteins are encoded within the T6SS genomic island in *V. fischeri*, suggesting that the ability to self-regulate may be a strategy to activate T6SS expression upon horizontal transfer of the T6SS genomic island into a new bacterial host [40].

In addition to competition mediated by T6SS, multiple mechanisms for horizontal gene transfer have been reported in *V. fischeri*. The ability to acquire DNA via natural transformation is conserved in *V. fischeri* and requires the *tfoX* and *tfoY* genes along with induction by chitin oligosaccharides such as chitohexaose [41]. This mechanism provides an important genetic tool for transferring targeted mutations across strains, but also has broad implications for how *V. fischeri* evolves by acquiring free DNA from the surrounding environment. Some *V. fischeri* strains, including the commonly studied light organ isolate strain ES114, also encode a functional conjugative plasmid which has been shown to promote the transfer of other plasmids between *V. fischeri* strains [42].

The *E. scolopes* light organ symbiosis has proven itself to be an incredible model system for studying factors mediating host-colonization within a simplified microbiome. Multiple competitive and cooperative mechanisms have been described in *V. fischeri*, allowing researchers to study complicated intraspecies interactions within the context of a genetically tractable symbiosis. This dissertation contributes (1) a novel fluorescence microscopy workflow for imaging and quantifying contact-dependent competition at the single cell level, and (2) combines this workflow with a subcellular model for T6SS interactions to investigate factors that drive competitive outcomes between lethal-lethal interactions. This study revealed that strains with the ability to activate T6SS more quickly upon transition to host-like conditions will dominate a competitive arena. Further, this dissertation (3) describes an experimental evolution assay that was used to select for the transfer of chromosomal markers between *V. fischeri* strains in coculture and revealed that the mechanism of horizontal gene transfer observed is inconsistent with any previously reported gene transfer mechanisms in *V. fischeri*. Finally, this dissertation expands our current knowledge of cephalopod-bacteria interactions by (4) characterizing the mantle, gill, sub-mantle tissue, and ANG microbiomes of the Atlantic brief squid, *Lolliguncula brevis*, using a combination of culture-based assays, microscopy, and amplicon sequencing. This study revealed that although *L. brevis* microbiomes include *Vibrio* species, *Bradyrhizobium* species are dominant, and further identified a surprisingly diverse gill community that could be manipulated to study more complex interspecies bacterial interactions in the future.

## CHAPTER 1 – Quantification of interbacterial competition using single-cell fluorescence imaging<sup>1</sup>

### 1.1 Introduction

This article outlines a method for quantifying bacterial competition at the single-cell level using fluorescence microscopy. The structure and function of microbial communities is often shaped by competitive interactions among microbes, and in many cases characterizing these interactions requires observing different bacterial strains in coincubation [38, 43-49]. Traditionally, bacterial competition is quantified at the population level by counting colony forming units (CFUs) of inhibitor and target strains before and after a coincubation period [43, 50]. Mechanisms for microbial competition are broadly distributed among bacteria and may rely on either diffusion or cell-cell contact to inhibit target cells [51-60].

Although bacterial strains are often observed in coincubation at the population level, this manuscript outlines an assay for single-cell quantification of bacterial competition. Further, this work includes suggestions for adapting the protocol for the use with other bacterial species. While the specific techniques in this article are used to study contact-dependent intraspecific competition between strains of the symbiotic bacterium *Vibrio fischeri* [30, 61, 62], they can be adapted for competition between many organisms. This article provides instructions for slide setup on both upright and inverted microscopes, and all analysis is described using the open-source software FIJI [63] so that the method can be used by researchers with access to different imaging setups and analysis programs. Given the importance of studying microbial competition at both the population and single-cell level, this method will be a valuable resource for researchers to quantify competitive interactions, particularly those that do not have access to proprietary analysis software.

---

<sup>1</sup>This chapter was previously published as an article in *Journal of Visualized Experiments*. The original citation is as follows: Smith S, Septer AN. Quantification of Interbacterial Competition using Single-Cell Fluorescence Imaging. J Vis Exp. 2021 Sep 2;(175):10.3791/62851. doi: 10.3791/62851. PMID: 34542540; PMCID: PMC8944913.



## 1.2 Protocol

### Optimization of bacterial strains

1. Choose two bacterial strains for single-cell bacterial competition assays. Here, two strains of *V. fischeri* are used: a target strain (ES114 [64]) and an inhibitor strain (MJ11 [65]) that is known to kill the target strain using the type VI secretion system on chromosome II (T6SS2) [38], which is a contact-dependent killing mechanism.
2. Determine the appropriate controls for the experiment. In this example, the appropriate control is to incubate both the wild-type and the T6SS inhibitor mutant strains with the target strain to quantify the effect of T6SS-mediated killing.
  - a. NOTE: Additional controls can include a target strain that expresses the necessary immunity gene(s) to prevent T6SS-dependent killing or an inhibitor mutant strain expressing wild-type copies of the mutated genes *in trans* to restore T6SS activity [38].
3. When possible, transform strains with stable plasmids encoding genes for different fluorescent proteins (e.g., GFP or RFP) to visually distinguish strain types on the microscope. Here, the inhibitor strain is tagged with a GFP-encoding plasmid (pVSV102), and the target strain is tagged with a dsRed-encoding plasmid (pVSV208) [66].
  - a. NOTE: If it is not possible to use stable plasmids, fluorescent tags can be introduced onto the bacterial chromosome for visualization [67, 68].
4. During the initial optimization period, image clonal cultures of the tagged strains under each of the fluorescent filters that will be used during the experiment to ensure that cells are only visible in the intended channel. For example, ensure that a GFP-tagged strain is only visible in the FITC channel.

### Agarose pad preparation

1. Prepare agarose pad solution by dissolving 2% low-melt agarose (w/v) into mPBS. Heat the solution briefly in the microwave and vortex until the agarose is completely dissolved. Keep this solution warm by placing it in a 55°C water bath until ready to use. See the Discussion section for more information about preparing agarose pads.

- a. NOTE: Here, mPBS was prepared by adding 20 g/L to standard 1X PBS.
2. Wrap a piece of lab tape around a glass slide five times. Repeat this process a second time on the same slide so that the distance between the two pieces of tape is slightly smaller than the width of a coverslip (Figure 1.1A). For example, if using 25 mm<sup>2</sup> coverslips, the pieces of tape should be spaced approximately 20 mm apart.
  - a. NOTE: While the number of times the tape is wrapped around the slide can be modified to adjust the thickness of the agarose pad, it is important that the layers of tape are the same height on both sides of the slide so that the agarose pad remains flat.
3. Pipette warm agarose solution between the two pieces of tape and immediately top with a coverslip so that it rests on the pieces of tape. This will ensure that the surface of the agarose pad remains flat. The volume of agarose solution pipetted in this step should be enough that the coverslip makes contact with the liquid and pushes out any bubbles in the agarose solution. For this particular setup, 200 µL of warm agarose is sufficient.
4. Let the agarose pad solidify at room temperature for at least 1 h prior to the coincubation assay. Step 2 will produce an agarose pad of approximately 20 mm<sup>2</sup>.
5. Cut this agarose pad with a razor blade into four, 5 mm<sup>2</sup> pads to be used for imaging.
  - a. NOTE: Agarose pads can be made up to one week prior to the experiment and stored at 4°C in an empty, sterile, Petri plate sealed with parafilm to prevent drying.

#### Prepare strains for co-incubation

1. Streak out each strain to be used in the coincubation assay from -80°C stocks onto LBS agar plates supplemented with the appropriate antibiotics and incubate overnight at 24°C. For this example, three strains are used: the wild-type inhibitor strain, the type VI secretion system mutant, and the target strain.
2. The next day, start overnight cultures in biological duplicate by picking two colonies from each strain and resuspending them in LBS medium supplemented with the appropriate antibiotics and incubate overnight at 24°C with shaking at 200 rpm.

3. On the following morning, subculture each biological replicate 1:1000 into fresh LBS medium without antibiotics and incubate at 24°C with shaking for 4-5 h or until cells reach an OD<sub>600</sub> of ~1.5.
  - a. NOTE: The timing of steps 1, 2, and 3 may need to be optimized for different bacterial species as their growth rate may vary substantially. For this assay, cells were aimed to be in mid-log phase at the start of the coinubation assay.

#### Coinubate bacterial strains

1. Starting with mid-log cultures from the previous step, measure and record the optical density at 600 nm (OD<sub>600</sub>) for all samples.
2. Normalize each sample to an OD<sub>600</sub> = 1.0, which corresponds to approximately 10<sup>9</sup> CFU/mL for *V. fischeri*, by diluting the culture with LBS medium.
3. Mix the two competing strains together at a 1:1 ratio based on volume by adding 30 µL of each normalized strain to a labeled 1.5 mL tube. Vortex the mixed-strain culture for 1-2 s.
  - a. NOTE: In some cases, it may be appropriate to mix cocultures in different ratios. For example, when one strain grows much faster than the other, it may be necessary to start the slower growing strain at a numerical advantage in order to observe the competition. Optimization may also be required if OD<sub>600</sub> does not correspond to similar CFU/mL for both strains.
4. Repeat step 3 for each biological replicate and treatment. In the example shown here, this will result in a total of four mixed-strain tubes: two biological replicates with the wild-type inhibitor strain mixed with the target strain and two biological replicates with the type VI secretion system mutant strain mixed with the target strain.
5. To ensure competing cells are sufficiently dense for contact-dependent killing in the coinubation on the agar pad, concentrate each mixed culture 3-fold by centrifuging the mixed culture in a standard 1.5 mL centrifuge tube for 1 min at 21,130 x g, discarding the supernatant, and resuspending each cell pellet in 20 µL LBS medium. Repeat for each sample.
  - a. NOTE: Some bacterial cells are sensitive to damage by centrifugation at high rcf; in such cases the mixed culture can be centrifuged for 3 min at 4600 x g [69]. Additionally, when

quantifying contact-dependent competition, it is important to ensure sufficient cell density on the slide to observe killing. In this article, “crowded” treatments, where killing is observed, had approximately 10 cells/20  $\mu\text{m}^2$ ; see the Discussion section for more information.

#### Slide setup

1. When using an upright microscope, place a  $\sim 5 \text{ mm}^2$  agarose pad onto a standard 1 mm glass slide. Spot 2  $\mu\text{L}$  of a mixed culture onto the agarose pad and place a #1.5 coverslip ( $25 \text{ mm}^2$ ) over the spot. See Figure 1.1B for an example.
2. When using an inverted microscope, spot 2  $\mu\text{L}$  of a mixed culture onto the #1.5 coverslip bottom of a 35 mm Petri dish and place a  $\sim 5 \text{ mm}^2$  agarose pad over the coincubation spot. Place a 12 mm circular glass coverslip over the agarose pad. See Figure 1.1C for an example.
3. Repeat step 1 or 2, depending on the microscope setup used, for the remaining three mixed cultures, resulting in four slides or dishes to be imaged.
4. Allow slides to sit on the benchtop for approximately 5 min before proceeding to the next step. This allows cells to settle on the agar pad and eliminates movement during the imaging process.

#### Fluorescence microscopy

1. Begin by focusing on cells using white light (phase contrast or DIC) to minimize the effects of photo-bleaching. Based on the average size of a single bacterial cell, use a 60x or 100x oil objective.
2. Adjust the exposure time and acquisition settings for each channel so that cells are visible in the appropriate channel with minimal background detection.
  - a. NOTE: It is appropriate to use different exposure times for different channels, but the same exposure time should be used across all biological replicates and treatments for a given channel.
3. For each sample, select at least five fields of view (FOV) and acquire images in each appropriate channel using the acquisition settings from step 2 (See examples in Figure 1.2). Save the XY points from each FOV so that the same FOV can be imaged during the final time point. Imaging

the same FOV at each time point is necessary to determine the proportion of area occupied by target or inhibitor cell during the analysis steps.

- a. NOTE: In this example, the fluorescence of GFP is detected using a filter with an excitation wavelength of 467 – 498 nm and an emission filter of 513 – 556 nm and is false-colored green. Fluorescence of dsRed is detected using a filter with an excitation wavelength of 542 – 582 nm and an emission filter of 603 – 678 nm and is false-colored magenta.
4. After 2 h, repeat step 3 for each sample using the previously saved XY points (Fig 1.2).
  - a. NOTE: The timing of subsequent images may need to be optimized for organisms with different growth rates or competitive mechanisms.

#### Image analysis in FIJI

1. Download and install the FIJI image processing software using the instructions found here: <https://imagej.net/Fiji/Downloads>
2. Open FIJI and import image files for analysis.
  - a. NOTE: In most cases, .TIFF files will be used for image analysis, although some image acquisition software will export using proprietary file types. FIJI can recognize most proprietary file types and images can be imported and analyzed as follows.
3. For each image acquired above, convert the image to grayscale, separate the channels, and begin by thresholding (Ctrl + Shift + T) and creating a binary mask of the preprocessed image (Figure 1.3A,B).
  - a. NOTE: Here, the default thresholding settings in FIJI are used. In some cases, it may be necessary to change those settings, in which case the same settings should be used for all images in that experiment.
4. Set scale on the image (**Analyze | Set Scale**) using the appropriate values for the microscopy setup [63].
5. Set measurements (**Analyze | Set Measurements**) and select **Area**.
  - a. NOTE: Other measurements can be added if they are appropriate for the experiment. Only the **Area** measurement is required for the example analysis shown here.

6. Analyze particles (**Analyze | Analyze Particles**) using the default settings (Figure 1.3C). If there are debris in the sample, it may be necessary to adjust the size or circularity to filter out non-cell particles. Select **Show | Outlines** so that the output of this analysis will include a numbered outline of all particles analyzed (Figure 1.3D).
  - a. NOTE: Comparing the outline in Figure 1.3D to the initial image is especially important in the optimization step to ensure that (1) all cells are being analyzed, and (2) that any debris is excluded from the analysis.
7. Export the measurements from step 7.4 (Figure 1.3E) into a spreadsheet software for further analysis and graphing.
8. Repeat steps 1-5 for all channels and images acquired during the experiment.

#### Calculating the percent of initial target area over time

1. For each field of view analyzed in the previous section, ensure that the exported files contain an individual area measurement for each particle that was analyzed. Beginning with the target strain's fluorescence channel, calculate the sum particle area for each individual field of view. For two biological replicates with five FOV each, this should result in ten sum areas per treatment at each time point.
2. Calculate the percent of initial target area over time for each FOV using the following equation:

$$\left( \frac{(\text{final sum area})}{(\text{initial sum area})} * 100 \right)$$

3. Repeat this calculation for all treatments and graph the percent of initial target area (result of the equation from step 2) for each treatment (Figure 1.4A).
4. Determine whether there is a net increase in the target population (indicating growth), a net decrease in the target population (indicating death), or no change (indicating no growth or death) for each treatment.
  - a. NOTE: Percent of initial target area with values greater than 100 indicate net target growth, and values lower than 100 indicate net target death. Percent of initial target values that remain at 100 indicate no net change in target population. See discussion for suggested follow-up experiments.

#### Calculating the percent of initial inhibitor area over time

1. Repeat steps 1 to 3 from the previous section, this time using the measurements collected from the inhibitor strain's fluorescence channel (Figure 1.4B).
2. Determine whether there was a net increase in inhibitor population (growth); a net decrease in inhibitor population (death); or no change for each treatment. Values greater than 100 indicate net inhibitor growth, and values lower than 100 indicate net inhibitor death.

### 1.3 Representative Results

To visualize and quantify competitive interactions between bacteria at the single-cell level, a protocol was developed and optimized for *V. fischeri* by modifying our well-established CFU-based assay [38, 43]. This method utilizes GFP- and dsRed-encoding stable plasmids to visually distinguish different strains of *V. fischeri*. The competitive outcome of these interactions can be quantified by analyzing the images acquired from this assay using the open-source software FIJI. As an example, the following experiment was performed using *V. fischeri* isolates. An inhibitor strain harbored a plasmid that encodes GFP, and a target strain harbored a plasmid that encodes dsRed. Given that the T6SS2 encoded by the inhibitor strain is a contact-dependent killing mechanism, treatments were included where cells were either crowded (high cell-cell contact) or dispersed (low cell-cell contact) on a slide to highlight the impact of experimental setup on the final results of this assay. In the sample data, competing strains were mixed at a 1:1 ratio and incubated on an agarose pad for 2 h, and both initial and final (2 h) images were taken. As a control, a T6SS2 mutant strain was also incubated with the target strain in both crowded and disperse conditions. Cultures of each strain were prepared and coincubated as described above and slides were prepared as shown in Figure 1.1.

Figure 1.2 shows representative fluorescence microscopy images of each experimental treatment with the same field of view imaged at an initial and final time point. For each treatment, either a wild-type inhibitor or T6SS mutant strain harboring a GFP-encoding plasmid was mixed at a 1:1 ratio with the target strain harboring a dsRed-encoding plasmid. During a 2 h coincubation period with this experimental setup, growing *V. fischeri* cells may go through 1-2 divisions (Figure 1.2; **gray arrows**). In Figure 1.2A, cell-cell contact was forced between the target and inhibitor by concentrating the mixed culture before spotting onto the slide. Multiple target cells are observed to become rounded and/or disappear over the course of 2 h, consistent with target cells being eliminated by inhibitor cells (Figure 1.2; **white arrows**). See the Discussion for more information on interpreting rounding or lysing target cells. In Figure 1.2B, the same coincubation was spotted onto a slide, this time without concentrating the mixed culture so that the cells remained dispersed and there was minimal contact between strains on the slide. Here, no target cells are observed to disappear or to round, suggesting that the target strain was not inhibited in this treatment. Figure 1.2C and Figure 1.2D show the same crowded and dispersed treatments described



above, this time using a T6SS mutant as the inhibitor strain. Target cells were not observed to disappear or round when coincubated with a T6SS mutant in either crowded or dispersed conditions, again suggesting that the target was not inhibited in either treatment.

Figure 1.3 shows the FIJI analysis workflow used to quantify competition in this protocol. A representative image from the target channel was selected (Figure 1.3A) and a binary mask was created using the default threshold settings in FIJI (Figure 1.3B). The image scale was set appropriately for this microscopy setup. Particles were analyzed using the size parameter = 0 – infinity, circularity parameter = 0.00 – 1.00, and **Show Outlines** was selected (Figure 1.3C). The results of this particle analysis are shown as both a numbered outline of each particle (Figure 1.3D), and as a table with columns for the particle number, file name (label), and particle area in  $\mu\text{m}^2$  (area) (Figure 1.3E).

In Figure 1.3, data obtained from Figure 1.3E is graphed and analyzed. In Figure 1.4A, the percent of initial target area at the final timepoint is presented for each treatment. If the percent of initial target area is greater than 100, this represents net increase in target (i.e., growth) and is observed in conditions where the target population is not significantly inhibited. However, if the percent of initial target area is lower than 100, this result indicates a net decrease in target (i.e., death) and is observed in conditions where the target population is significantly inhibited. When the target was coincubated with a wild-type inhibitor in crowded conditions, the data show a net decrease in the target area. By contrast, when the target was coincubated with either a wild-type inhibitor in disperse conditions or a T6SS mutant in crowded or disperse conditions, the data show a net increase in the target area. The percent of initial target area when the target was coincubated with a wild-type inhibitor in crowded conditions was below 100 and significantly lower than all the other treatments according to a one-way ANOVA followed by a Tukey's multiple comparisons test across all treatments ( $p < 0.0001$ ). These data indicate that the target cell death is dependent on a functional T6SS in the inhibitor and underscores the importance of an experimental setup that allows sufficient cell-cell contact, in order to detect cell death from a contact-dependent killing mechanism.

Figure 1.4B presents the percent of initial inhibitor area at the final timepoint for each treatment. In this example, net growth of the inhibitor strain was observed across all treatments. However, the percent of initial inhibitor area was significantly higher when a wild-type inhibitor was coincubated with the target

in crowded conditions compared to all other treatments according to a one-way ANOVA followed by a Tukey's multiple comparisons test across all treatments ( $p < 0.0001$ ). Initially, we considered that the net increase in inhibitor area may be driven by the increase in available space to grow into as target cells are eliminated. However, this same increase in inhibitor growth was not observed in disperse treatments, where inhibitor cells had room to grow from the beginning of the coincubation. Alternatively, this result could suggest that nutrients released from lysing target cells allow for a greater increase in the inhibitor population. Taken together, these results suggest that the inhibitor strain eliminates the target in a T6SS-dependent manner only when high cell-cell contact is forced by crowding cells on the slide.

## 1.4 Discussion.

The protocol described above provides a powerful tool for quantifying and characterizing interbacterial competition at the single-cell level. This assay, which was developed by modifying our CFU-based competition assay on agar plates [38, 43], allowed for the visualization of single-cell competition among *V. fischeri* isolates and suggestions are provided for optimizing the method for a wide range of systems and microscopy setups. Although the method described here was optimized for the light-organ symbiont *V. fischeri*, it can be easily modified to accommodate many diverse, culturable microbes. It is important to note that competitive mechanisms can be regulated by any number of environmental variables, including temperature, salinity, and viscosity [39, 70-73]. Previous work has confirmed that *V. fischeri* competes using a contact-dependent Type VI Secretion System that is active on surfaces [39], making the conditions described in this assay suitable for studying competition between the example strains. It is also important to consider the initial density of cells on the slide when quantifying bacterial competition. Given that contact between target and inhibitor cells is often required for killing to occur, the mixed culture should be concentrated such that cell-cell contact is maximized and cells remain in a single plane on the slide. Cell cultures should be grown to a similar optical density (mid-log phase) and then concentrated to force contact rather than simply growing cultures to a higher optical density due to the physiological changes of cells in different growth phases. In other systems, culture conditions and the experimental setup may need to be modified to ensure that the competitive mechanism is active and can be detected in the coincubation condition.

The agarose pads used in this assay provide several benefits: they provide stabilization so that cells do not move around freely, and they prevent the culture from drying out over the course of the experiment. Additionally, if chemical inducers, such as isopropyl- $\beta$ -D-thiogalactoside (IPTG), are required for the experiment, they can easily be added to the agarose solution. However, it is important to note that the agarose solution will likely need to be adjusted for different systems. In the example described above, the agarose pad was prepared by dissolving 2% agarose (w/v) into 20 psu mPBS, which is the standard salinity used in *V. fischeri* growth medium. Furthermore, in some cases a carbon source may need to be added to the agarose pad in order for cells to grow and compete over longer experiments. In such a case,

the mPBS in agarose pads can be replaced with any growth medium, although the nutrients in growth medium may come with the tradeoff of additional background fluorescence.

Without proprietary image analysis software, it can be very difficult to get individual cell counts when cell-cell contact is high, which as we show here is required to observe contact-dependent killing. This assay was designed to provide an alternative method for quantification that does not rely on individual cell counts. Instead, the total cell area for each fluorescence channel is used to quantify the extent of killing between co-incubated strains. Because this method relies on area rather than individual cell counts, default threshold settings are typically sufficient for outlining the total cell area. The accuracy of thresholding can be verified by dividing the total object area for a representative field of view by the average cell size for the model organism and comparing this estimated cell number to a manual cell count for the same image.

In co-incubations between one inhibitor and one target (nonkiller) strain, net growth of the inhibitor is predicted. As seen in Figure 1.4, inhibitor growth may be significantly higher in treatments where killing is observed, compared to treatments where killing is not observed, perhaps because nutrients released by lysing target cells allow the inhibitor strain to grow more quickly. In the example shown here, net target death is observed because T6SS-mediated competition results in target cell lysis where the target is physically eliminated. However, it is important to note that not all competitive mechanisms result in the physical elimination of target cells. If a target is incapacitated by a toxin that causes growth inhibition, the protocol outlined here may result in the visible target population remaining stable over time as target cells no longer grow but also do not lyse. In such a case, it would be appropriate to compare the results of this assay with follow up tests for target cell viability, such as plating for colony forming units (CFUs) or by performing live-dead assays by staining with propidium iodide or SYTOX green [74, 75].

Compared to co-incubation assays that rely on CFU counts, this assay makes it possible to observe and quantify the spatial structure of competition between strains and track changes in target cell morphology over time. For example, inhibitor cells that kill using a T6SS are known to encode LysM-domain proteins that degrade the target cell wall, resulting in initial cell rounding and then lysis [54], which we observed in the example shown in Figure 1.2A. Further, this protocol can be used to track competition at high resolution over very short time scales. In the example shown here, a significant decrease in the target

area is observed after only two hours when cells are crowded, and cell-cell contact is forced between strains (Figure 1.4). The image analysis described here could also be performed using confocal microscopy, which would make it possible to study bacterial competition *in vivo* or in complex biofilms, without disrupting the spatial distribution of coincubated strains.

In summary, the assay described here aims to provide an accessible and easily modified approach for visualizing and quantifying bacterial competition at the single-cell level using fluorescence microscopy. This method can be applied to diverse bacterial isolates and can be used to visualize bacterial competition even in complex environments such as within a host or biofilm matrix.

## 1.5 Figures.

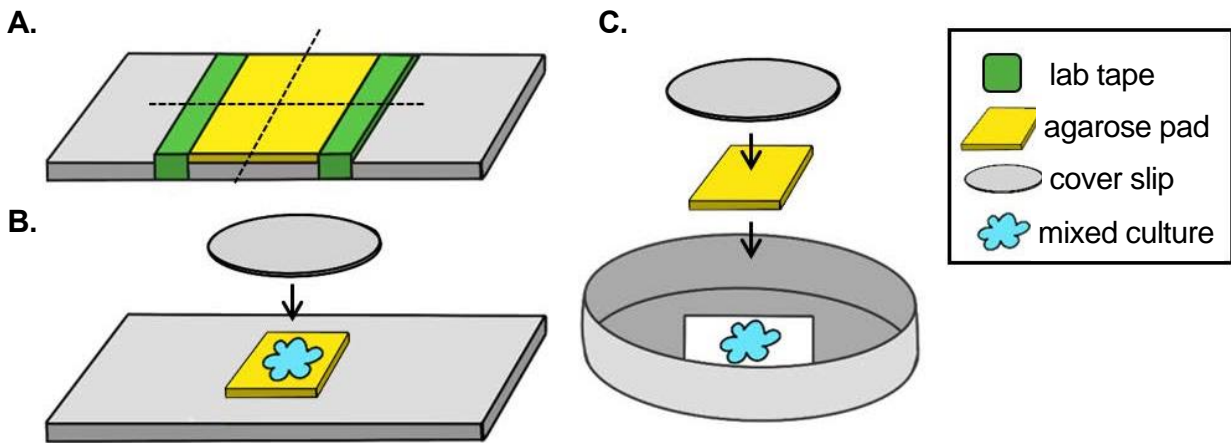


**Figure 1.1. Agarose pad preparation and slide setup for coincubation assays.** (A) Setup for making 2% agarose pads. Five layers of lab tape (green) are wrapped around a cover slip at two points approximately 20 mm apart. Next, warm 2% agarose in mPBS (yellow) is pipetted between the pieces of tape and immediately covered with a 25 mm<sup>2</sup> cover slip and allowed to solidify for at least 1 h at room temperature. Use a razor blade to cut the agarose pad into ~5 mm<sup>2</sup> pieces and use tweezers to transfer the pad to a new slide for imaging. (B) When imaging on an upright microscope, place the 5 mm<sup>2</sup> agarose pad directly onto the slide, followed by the mixed culture (blue) and a 12 mm circular #1.5 cover slip. (C) When imaging on an inverted microscope, spot the mixed culture directly onto the #1.5 glass cover slip bottom of a 35 mm Petri dish, and place an agarose pad on top of the culture followed by a second 12 mm circular cover slip to flatten the agarose pad.

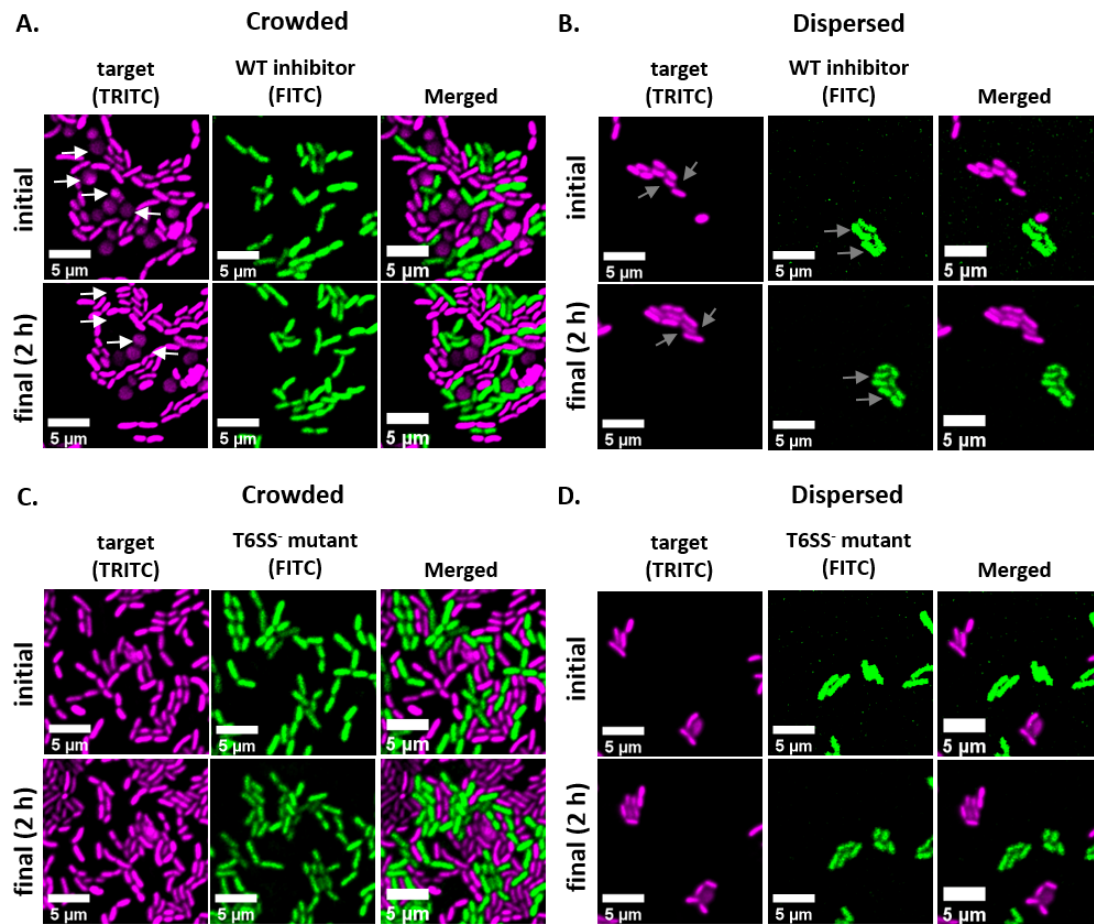


**Figure 1.2. Time lapse images of coincubation spots in either crowded or dispersed conditions.**

(A) Representative images at initial and final time points where a mixed culture of target and wild-type inhibitor was concentrated 3x prior to spotting on the slide to force cell-cell contact between strains. White arrows in TRITC channel indicate examples of target cells that round or lyse throughout the course of the experiment. (B) Representative images where a mixed culture of target and wild-type inhibitor was spotted without concentrating so that cells are dispersed and there is minimal cell-cell contact between strains. Gray arrows in FITC and TRITC channels indicate examples of cell division throughout the course of the experiment. (C) Representative images where mixed culture of target and T6SS<sup>-</sup> mutant was concentrated 3x prior to spotting on the slide to force contact between strains. (D) Representative images where mixed culture of target and T6SS<sup>-</sup> mutant was spotted without concentrating so that cells are dispersed and there is minimal cell-cell contact between strains. Scale bars = 5 μm and are consistent across all images; TRITC channel is false-colored magenta, FITC channel is false-colored green. Deconvolution was performed on all images; background was subtracted, and brightness/contrast adjusted uniformly across all images.

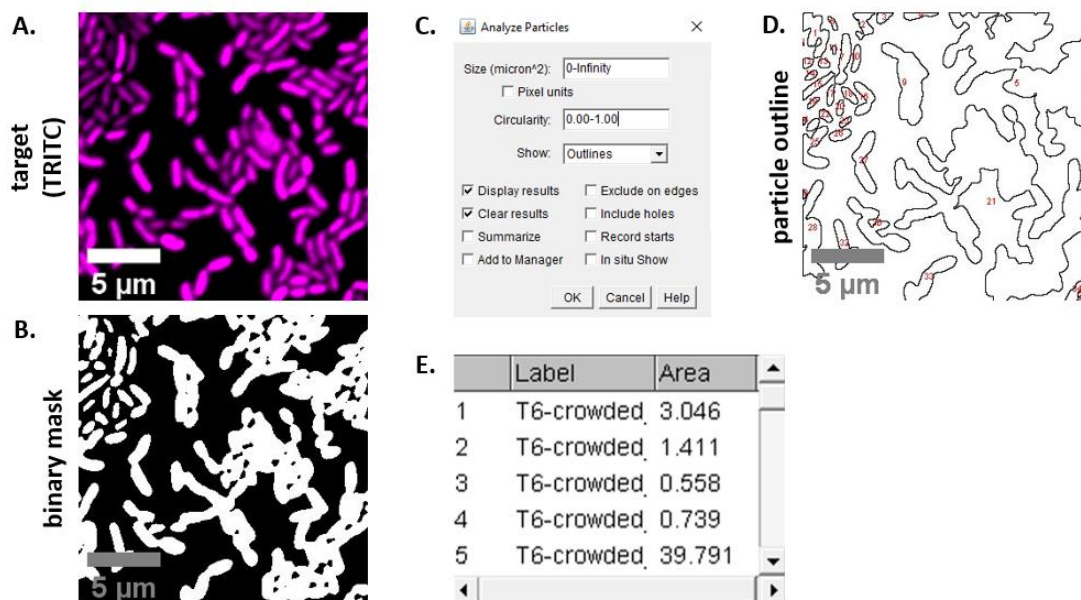


**Figure 1.3. FIJI analysis workflow.** (A) Representative image for analysis. This workflow is repeated for both channels across all fields of view and samples. Scale bars = 5  $\mu$ m and are consistent across all images; TRITC channel is false-colored magenta. (B) Binary mask created by thresholding the image using the default settings in FIJI. (C) Example of settings for particle analysis used in this manuscript. Size range = 0 – infinity  $\mu$ m<sup>2</sup>; circularity = 0.00 – 1.00; show = outlines. (D) Particle outline created as an output of particle analysis in (C). The particle outline in (D) should be compared to the original image (A) to ensure that all cells were captured in the particle analysis. (E) Results table created as an output from particle analysis in (C). Object number (column 1) corresponds to individual particles (one or more cells) outlined and labeled in red in panel (D). Label = file name of analyzed image; Area = total particle in  $\mu$ m<sup>2</sup>.



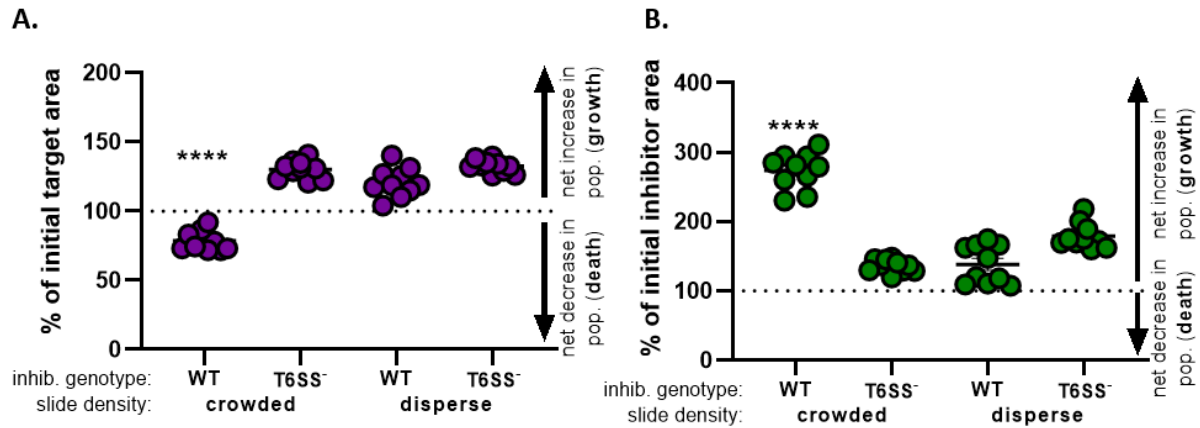


**Figure 1.4. Sample data for assessing whether target strain is inhibited.** The percent change in area between initial and final time points for the target strain **(A)** and inhibitor strain **(B)**, at different initial cell densities. Slide density indicates either a starting cell density that is crowded (high cell contact between strains), or more disperse (low cell contact between strains) as described in Figure 2. Inhibitor genotype indicates that either a wild-type or the T6SS mutant (T6SS<sup>-</sup>) strain was coincubated with the target strain. Asterisks indicate a significant different in % change comparing all treatments (one-way ANOVA followed by a Tukey's multiple comparisons test comparing all treatments; ( $p < 0.0001$ )). Dashed line indicates no net change in strain area between the initial and final timepoint; a % change > 100 indicates net increase (i.e. growth) and % change < 100 indicates net decrease (i.e. cell death).

## CHAPTER 2 – A subcellular biomechanical model for T6SS dynamics reveals winning competitive strategies<sup>2</sup>

### 2.1 Introduction.

All life forms compete with one another in what Charles Darwin referred to as “the struggle for life” [76]. Indeed, fierce battles for limited space and resources can be observed across biological complexity, from single cell organisms to humans. These battles often determine which population will proliferate, and which will be excluded. Therefore, organisms at all size scales have evolved diverse strategies to wage war on their rivals and increase the probability of their own success.

Microbial genomes encode an incredible arsenal of interbacterial weaponry [9], and some, e.g., the broadly distributed type VI secretion system (T6SS), have been shown to be useful in competing for colonization sites within a hot niche [11, 26, 38, 71, 77-80]. T6SSs resemble a molecular syringe and are thought to have evolved from bacteriophage contractile tails [81, 82]. T6SS-containing cells build a sheath-and-tube structure that extends the width of a cell and is anchored into the cell wall and membrane [83]. When a T6SS<sup>+</sup> cell comes in contact with a target cell, the sheath is contracted, the inner tube and toxins are propelled into the neighboring cell, resulting in cell death and lysis of the competitor [54, 84-87]. Although genome sequencing allows us to identify the bacterial strains that harbor T6SS interbacterial weapons [88], we are unable to predict which microbial population will dominate in an ecologically relevant battle based on genetic data alone [89]. To do so requires a more detailed and holistic understanding of the T6SS function, dynamics, its regulation, and how these factors, combined with environmental ones, influence competitive outcomes. The goal of this work is to gain insight into how differences in T6SS function at the individual cell level can influence survival of that genotype at the population level when facing another T6SS-armed competitor.

---

<sup>2</sup>This chapter was previously published as an article in *bioRxiv*. The original citation is as follows: Yuexia Luna Lin, Stephanie N. Smith, Eva Kanso, Alecia N. Septer, Chris H. Rycroft. bioRxiv 2021.07.17.452664; doi: <https://doi.org/10.1101/2021.07.17.452664>

Numerous works contribute to uncovering the diversity in the regulation of T6SS expression, as well as its function and behavior in various bacteria [7, 35, 48, 84, 90-98]. Other studies investigate the effect of T6SS-mediated competition on spatial organization and population dynamics both *in vivo* and *in vitro* [34, 35, 38, 39, 99, 100]. In natural niches like the light organ of the Hawaiian bobtail squid, *Euprymna scolopes*, T6SS<sup>+</sup> *Vibrio fischeri* has been shown to eliminate unarmed competitors and singularly colonize entire crypt spaces [26, 34, 35, 38, 40, 87, 101]. *In vitro*, studies of T6SS-dependent competition find that mutually armed strain pairing often result in coexistence through formation of coarse, spatially separated microcolonies in which T6SS attacks occur on the borders between strains [38, 99, 100].

Indeed, recent work has shown how T6SS function can be influenced by a number of biochemical factors. For example, studies have shown that availability of T6SS structure proteins affects the number, form, and function of the T6SS apparatus [94, 96, 102], and the speed of cell lysis induced by T6SS effectors can fine-tune the effectiveness of the T6SS apparatus as a lethal weapon [54, 92, 103]. Many of these works combine experiments with computational approaches, such as agent-based modeling, to study complex living systems. Agent-based models (ABMs) have been widely applied to studying population dynamics and spatial organization in a broad range of contexts [104-110]. When applied to modeling T6SS-dependent competitions between bacterial populations [54, 92, 93, 99, 111-113], ABMs have yielded insightful results regarding the survival of target populations under T6SS attack [54, 111] and the evolution of T6SS attack strategies such as tit-for-tat [93, 113].

Existing T6SS ABMs have established well-accepted interaction rules among T6SS-dueling cells [54, 92, 93, 99, 100, 111, 113]. For example, T6SS weapons are fired at a given rate and they hit a target cell with some probability; after receiving a certain number of attacks the target cell dies and subsequently lyses. These interactions are often modeled as probabilistic events at the cellular level. For example, to model firing, a random number is drawn from a Poisson distribution [54, 113] or a uniform distribution [99] to represent the number of firing events within a time interval. However, to date we are not aware of any experimental evidence supporting these distributions. Bacteria are also known to regulate T6SS activity according to environmental stimuli [7, 39, 40, 101, 114-116], however, this aspect has largely been neglected in modeling. Together, this underscores the lack of a unified mathematical

framework to model how T6SS structure numbers and firing frequencies are regulated that is also based on experimental data.

Here, we use *V. fischeri* as a model organism to fill this knowledge gap and connect physiologically-relevant T6SS biochemical factors to competitive outcomes (Fig 2.1A). Our study builds on previous findings showing that when two T6SS-armed *V. fischeri* strains compete, one is eventually eliminated, albeit not as quickly as an unarmed population [38]. This finding revealed that (1) strain-specific differences exist among T6SS<sup>+</sup> populations and affect competitive outcomes, and (2) *V. fischeri* serves as a tractable model system to study how strain-level diversity influences T6SS-mediated killing between natural competitors. In this work, we performed assay experiments on *V. fischeri* light organ isolates from *E. scolopes*, which are natural competitors in the squid light organ niche and conditionally express a T6SS encoded on chromosome II (T6SS2) [26, 35, 38, 61]. Upon entering a high viscosity or surface-associated environment, *V. fischeri* can activate and engage T6SS2 to kill under laboratory conditions [39, 40, 101]. Because the T6SS2 of *V. fischeri* can be controlled by culture conditions, we were able to quantify the strain-specific differences in speed of T6SS activation, number of sheaths per cell, and killing rates.

Although any of these factors could tip the balance in favor of one strain in competition, we are unable to manipulate each factor, alone or in combination, in biological experiments. Therefore, we leveraged detailed microscopy data to build a model of subcellular T6SS dynamics and map experimental measurements to model parameters. We then integrate this subcellular model in an off-lattice ABM (Fig 2.1B) and validate the ABM against experimental data. An ABM is particularly suitable for investigating the connection between the subcellular dynamics of T6SS and the competitive strength of a T6SS<sup>+</sup> population because it bridges the scale of individual cells and that of the population as a whole. The choice of using an ABM also helps define the scale at which we approach modeling of the subcellular dynamics. We restrict our model to the scale of individual T6SS structures, which has the dual benefits of being easily tracked in individual cells in the ABM, and easily visualized *in vitro* using live-cell fluorescence microscopy. By systematically varying the T6SS parameters in the ABM, we investigate how competitive outcomes depend on T6SS activation level, the number of T6SS structures cells harbor, how

fast structures can be built and utilized, the cost of building structures, as well as the spatial geometry of the competition arena.

## 2.2 Results.

### Competition outcomes differ due to intraspecific variations in T6SS killing dynamics.

The ability of lethal strains of *V. fischeri*, which encode a strain-specific T6SS genomic island (T6SS2), to produce T6SS structures and kill target cells is dependent on environmental stimuli [39, 40, 101]. In liquid culture, *V. fischeri* T6SS2 is functionally inactive, while the exposure to a high viscosity medium such as hydrogel or an agar surface causes the cells to activate T6SS protein expression and structure formation [39]. We hypothesized that the response time to surface activation may differ among lethal strains of *V. fischeri*, and that these variations may affect competition outcomes between two lethal strains (Fig 2.1A). To begin testing this hypothesis, we coincubated the T6SS2-encoding *V. fischeri* strains ES401 and FQ-A002 (7) on LBS agar plates following two different preparations: clonal cultures of each strain were first incubated for 6 h either in (1) LBS liquid medium where T6SS2 activity is low, or (2) on LBS agar plates where T6SS2 activity is increased. Treatments where strains were incubated in liquid are referred to as “unprimed” because both strains come from a “T6SS off” condition and must activate T6SS at the start of their coincubation on agar surfaces, whereas strains incubated on agar are referred to as “primed” because these strains have fully activated T6SSs when they begin their coincubation on agar surfaces. We predicted that if the response time to surface activation is different between these two strains, then the strain that can more quickly activate T6SS to begin killing its competitor will dominate in the unprimed condition.

When unprimed wildtype ES401 and FQ-A002 were coincubated on LBS agar plates, microscopy images and colony forming unit (CFU) counts revealed that ES401 outcompeted FQ-A002 at the population level and only small microcolonies of FQ-A002 remained after 24 h of coincubation (Fig 2.2AD). Percentages of occupied area are calculated using the microscopy images; ES401 occupies 99.3% of the total area, compared to only 0.7% occupied by FQ-A002. However, when primed wildtype ES401 and FQ-A002 were coincubated, the two strains coexisted with comparable CFU counts and formed coarse, spatially separated microcolonies (Fig 2.2BD). The percentages of occupied area are 46.6% and 53.4%, for ES401 and FQ-A002, respectively. To determine whether this effect was dependent on T6SS2 activity, we used ES401 and FQ-A002 strains with a disruption in the *vasA\_2* gene, which encodes a baseplate protein in the T6SS2 complex and is required for T6SS-dependent killing [38,

39]. These *vasA* mutant (*vasA*<sup>-</sup>) strains were then coincubated in both primed and unprimed conditions. Regardless of coincubation conditions, both *vasA*<sup>-</sup> strains coexisted and were well-mixed, with no spatial separation between strains (Fig 2.2CD). The percentages of occupied area from each *vasA*<sup>-</sup> strain in both conditions are ~49% and ~51%, for ES401 *vasA*<sup>-</sup> and FQ-A002 *vasA*<sup>-</sup>, respectively. These findings reveal that one lethal strain (ES401) can dominate over another (FQ-A002) when both competitors have inactive T6SSs at the onset of competition, and the results support our hypothesis that surface activation timing affects competitive outcomes and warrant further investigation.

Based on the above findings, we reasoned that ES401 may activate its T6SS and begin killing target cells before FQ-A002, thus providing it an advantage in competition. To isolate the killing dynamics of both strains under unprimed conditions, and to see whether differences in killing rates after T6SS activation could be driving the observed dominance of ES401, we directly quantified their ability to eliminate a nonlethal target population over time. Specifically, we hypothesized that an unarmed target population could survive longer and in larger numbers when coincubated with a slower activating lethal strain. To test this hypothesis, we competed either (1) wildtype FQ-A002 vs. ES401 *vasA*<sup>-</sup>, or (2) wildtype ES401 vs FQ-A002 *vasA*<sup>-</sup> strains by spotting unprimed mixtures of each treatment on LBS agar pads and obtaining CFU counts of the lethal (wildtype) and the unarmed target (*vasA*<sup>-</sup>) strains every hour during a 5 h coincubation period. When the target strain CFUs were plotted over time for each coincubation, we observed that there was an approximately 10-fold drop in target CFUs between 1 h-2 h in coincubations between wildtype ES401 vs FQ-A002 *vasA*<sup>-</sup> target, whereas the ES401 *vasA*<sup>-</sup> target CFUs were maintained between 1 h-2 h in coincubation with the wildtype FQ-A002 (Fig 2.2E), suggesting that ES401 begins killing target populations before FQ-A002. From 2 h onward, we observed that the target populations in both treatments declined exponentially at approximately the same rate, i.e.,  $\sim \exp(-1.6t)$ , where  $t \in [2 \text{ h}, 5 \text{ h}]$  is time after spotting (Fig 2.2E), suggesting both of the wildtype ES401 and FQ-A002 lethal strains kill at comparable rates after T6SS activation. When the CFUs of wildtype ES401 and wildtype FQ-A002 were plotted, we found that both strains exhibit an initial decline during 0 h – 1 h, similar to what was observed for the *vasA*<sup>-</sup> target strains, suggesting this initial drop in CFU counts is independent of T6SS killing, and perhaps due to transition from liquid to surface growth (Fig 2.2E, SI Appendix Fig 2.S2). Moreover, the wild-type ES401 and FQ-A002 strains had similar growth rates under

these conditions (SI Appendix Fig 2.S2); thus, a difference in growth rate does not account for the differences in the target populations between treatments.

Taken together, these results suggest that when unprimed, wildtype ES401 is more effective in eliminating nonlethal targets compared to wildtype FQ-A002. Combined with our previous observation that wildtype ES401 outcompetes wildtype FQ-A002 in an unprimed competition, these results support our hypothesis that variations in competitive outcomes are driven by a strain-specific T6SS activation response to surfaces. To investigate this surface response in *V. fischeri*, we performed further experiments to quantify the percentage of cells in a population with T6SSs and the number of structures per cell over time.

#### **Quantifying strain-specific differences in T6SS activation dynamics.**

In a T6SS complex, VipAB/TssBC multimers comprise the outer component of sheath structure; thus, VipA has been used in multiple systems as a target for visualization of sheath dynamics through the use of a fluorescently-tagged VipA-TssB fusion construct [85, 94, 117], including an IPTG-inducible VipA-GFP expression vector in *V. fischeri* [38, 90]. To visualize T6SS activation dynamics, we grew overnight cultures of wildtype ES401 or FQ-A002 strains harboring the VipA-GFP expression vector to an OD<sub>600</sub> ~1.5 and spotted them onto an agarose pad supplemented with 0.5 mM IPTG immediately prior to imaging. We then took green fluorescence images of VipA-GFP expressed in either ES401 or FQ-A002 for our analyses (Fig 2.3A). Note that the color of each strain was altered for post-processing in the microscopy images for visualization. We categorized a cell as “T6SS activated” when we observed at least one sheath within the cell. To quantify the rate for T6SS activation for each strain, we measured the proportion of activated cells in the green fluorescence images taken at regular intervals between 0.5 h and 3 h after initial spotting (Fig 2.3B). These measurements revealed that the proportion of activated cells in both ES401 and FQ-A002 remained stable at low levels for approximately 1 h after plating. Directly from the liquid cultures, approximately 10% of ES401 cells and 5% of FQ-A002 cells have visible T6SS sheaths. After this initial waiting period, we observed the activated proportion increased over time in both ES401 and FQ-A002 but the rate of increase was approximately twice as high in ES401 compared to FQ-A002, suggesting that ES401 activates T6SS structure assembly more quickly than FQ-A002.



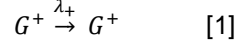
We reasoned that the number of T6SS structures in the T6SS arsenal of a strain may also impact competition outcomes in either positive or negative ways, as more T6SS structures might allow a strain to kill faster, but this advantage could come at an energetic cost. Therefore, we next quantified the number of sheaths per cell over time after *V. fischeri* cells are spotted on agar surfaces. We incubated ES401 and FQ-A002 clonally on an agarose surface as described above. For each strain, we counted the number of sheaths per cell for a given population in the green fluorescence images at an early stage after plating (2 h) and at a late stage (6 h) and plotted the frequency of having 0-7 sheaths at each time point (Fig 2.3C). For both strains, the average number of sheaths per cell increased between 2 h and 6 h on surfaces: ES401 went from an average of 1.1 sheaths per cell at 2 h to 2.8 sheaths per cell at 6 h, and FQ-A002 went from 0.5 at 2 h to 3.9 sheaths per cell at 6 h.

The sheath distributions of ES401 and FQ-A002 at 6 h are shown to be statistically different (Fig 2.3C). We found that experimental sheath distribution of ES401 at 6 h is similar to a Poisson distribution, which have been used in previous computational models of T6SS [54, 113] to represent the number of firing events. However, each of the other experimental sheath distributions in Fig 2.3C is statistically different from the Poisson distribution with the corresponding mean.

Taken together, these results suggest that the subcellular T6SS dynamics in *V. fischeri*, including baseline activation levels in liquid, the rate of surface activation, and likely the number of sheaths per cell, exhibit strain-specific variations. Moreover, a Poisson distribution is not sufficient to represent the sheath distribution in all strains and all activation states. The reasons may be attributed to the complex couplings between activation, assembly, and firing, as well as cell cycle and other regulatory factors. To systematically understand the effects of the strain-specific variations in T6SS-related factors on the outcomes of intraspecific competition, we turn to mathematical and computational modeling. A two-stage subcellular biochemical model of T6SS dynamics.

We develop a biochemical model of T6SS, which consists of stochastic processes in two stages: (1) activation, and (2) structure assembly and deployment. This type of multistage model based on stochastic processes is an established approach for modeling transcription and translation [118-121], and eukaryotic organelle synthesis [122], but it has not been applied to subcellular T6SS structures.

**Activation stage.** We define activation as the cell being in a state ready to assemble T6SS structures. We denote the state of T6SS activation with  $G$ , such that  $G^-$  and  $G^+$  indicate the inactive and active states, respectively. A cell in the inactive state  $G^-$  can be switched on at a constant rate  $\lambda_+$ ,



Here, we have abstracted into a single stochastic process the myriad processes that induce a T6SS activated state in a cell, e.g., sensing environmental signals which, depending on the system, could include certain chemical species, temperature, colonization of macrophages or viscosity [7, 39, 114-116], as well as translation and accumulation of T6SS proteins [94, 95]. We have also neglected the effect of cell cycle on DNA copy number, cell volume, or chemical concentration [118-120]. Cell cycle also affects the activation state of cells and T6SS structures per cell. Although we did not directly test whether daughter cells inherit their mother's activation state, our results in Fig 2.3 suggest this is likely the case as only a small percentage of cells (5%-10%) at 6 h have no observed sheaths. In addition, division reduces the structure number distribution in a population. To circumvent these issues and gain analytical insight, we consider an infinitely large population of simple cell-like reactors that do not grow or divide, each of which independently undergoes activation as described by Eq [1]. Based on experimental measurements in unprimed cultures (Fig 2.3B), we introduce two additional parameters:  $\rho_0$ , which accounts for the initial proportion of activated cells, and  $\tau_+$ , which accounts for the initial waiting period. At  $t = 0$ , each reactor has a probability  $\rho_0$  to be T6SS activated, and an inactive reactor waits  $\tau_+$  before commencing stochastic switching. The activated percentage of the population  $P(t)$  at time  $t \geq 0$  is:

$$P(t) = \begin{cases} \rho_0 & \text{if } t < \tau_+ \\ \rho_0 + (1 - \rho_0) (1 - e^{-(t-\tau_+)\lambda_+}) & \text{if } t \geq \tau_+ \end{cases} \quad [2]$$

For both ES401 and FQ-A002, the measurements of activated population percentage at 0.5 h and 1 h in Fig 2.3B are averaged to obtain their respective  $\rho_0$  values, and all measurements are used in least square regressions to estimate their respective  $\lambda_+$  and  $\tau_+$  (all values reported in Fig 2.3 caption).

**Structure assembly and deployment stage.** The second stage in the T6SS biochemical model describes T6SS structure assembly and deployment. Previous studies in T6SS<sup>+</sup> strains of *Pseudomonas aeruginosa*, *V. cholerae*, and *Acinetobacter baylyi* have shown that the effects of T6SS structural proteins on T6SS assemblies can be categorized in two ways: (1) the number of T6SS is driven by the abundance

of proteins such as the spike protein VgrG and effector proteins, which are present in low copy numbers, (2) the length of the sheath in a functional structure mainly depends on the abundance of multimeric proteins such as Hcp and VipAB [94, 95, 102, 115]. To incorporate these observations in our model, we attribute new T6SS assemblies to the appearance of a low abundance structural protein, which we assume is synthesized at a constant rate,  $\lambda_s$ . We further assume that being in the activated state, all other component proteins are sufficiently abundant, and thus do not limit the assembly. In terms of deployment, we consider that each T6SS structure can be independently fired at a constant rate,  $\lambda_f$ . Since each functional T6SS structure has a sheath apparatus, henceforth, the term sheath is used interchangeably with T6SS structure. Thus, we have the following stochastic processes for the number of sheaths  $N$ ,

$$\begin{aligned} N &\xrightarrow{\lambda_s} N + 1, \\ N &\xrightarrow{\lambda_f N} N - 1. \end{aligned} \quad [3]$$

In a large population of cell-like reactors undergoing both stages of the T6SS reactions (Eqs [1]-[3]), probability mass density function of number of sheaths per cell tends toward a steady state at the long time-limit. The rate of approaching steady state is determined by  $\lambda_+$  and  $\lambda_f$  (SI Appendix Section 3 & 4). In a T6SS<sup>+</sup> bacteria population with low initial T6SS activation, the model predicts the average sheath number increases over time. The steady state average number of sheaths is  $\overline{N_\infty} = \lambda_s / \lambda_f$ . We cannot determine  $\lambda_s$  or  $\lambda_f$  separately in our experiments. Instead, we estimate  $\overline{N_\infty}$  to be the same for both strains:  $\overline{N_\infty} = 3.5$ . Note that equation [1] focuses only on the activation process, and equations [3] neglect T6SS degradation processes independent of deployment. However, T6SS deactivation and degradation could be added in future work if required.

**The agent-based model (ABM) with internal T6SS model.** T6SS activity at the subcellular level directly affects the ability of T6SS<sup>+</sup> populations to kill, and thus influences the spatial structures on the length scale of the microbial colony [54, 92, 99, 100, 113]. To investigate the multi-scale interplay between subcellular T6SS dynamics, cellular growth, and intercellular interactions, we integrate the T6SS biochemical model into an ABM. We chose our in-house ABM primarily for the ease of developing and testing the internal dynamics of the cells. While our ABM is restricted to two-dimensions, it suffices for our present purpose of applying the internal model of T6SS to mono-layer colonies. In addition to imposing

T6SS-dependent interaction rules among dueling cells similar to those established in existing ABMs [54, 92, 113], each cell in our ABM undergoes internal stochastic reactions (Eqs [1] & [3]) governing the assembly and deployment of the T6SS arsenal (Fig 2.1B). We represent each cell as a spherocylinder (a cylinder with hemispherical ends) growing in a monolayer on a viscous substrate. Cell growth is modeled as elongation along the cylinder axis according to the adder model [123], while the radius of the cell is kept constant. As the cells grow and come into contact with one another, the mechanical interactions cause them to move and rotate and potentially restrict their growth.

Each cell maintains the internal state variables  $G$  and  $N$ , T6SS activation state and sheath number, respectively, and carries out internal stochastic reactions (Eqs [1] & [3]) at each time step in the simulation. If a cell fires a sheath, the target is randomly selected among the neighboring cells in contact. It is also possible for the cell to miss the neighbors and fire into the intercellular milieu. If the target is a clonemate, it survives; if the target is a nonclonal competitor cell, it ceases cellular function but participates in the mechanistic interactions for a time  $\tau_{lys}$  until it completes lysis and disintegrates. At division, the daughter cells inherit the mother cell's T6SS activation state  $G$ , and the mother cell randomly distributes its sheaths with equal probability to the two daughters. The internal T6SS reactions are also coupled to a cell's physiology via growth. In maintaining a T6SS arsenal, we assume that the energetic cost of T6SS protein expression and assembly is dominant over the cost of firing structures and maintaining the T6SS genes in the genome. A T6SS active cell has a penalized growth rate  $r'_0$  that decreases linearly with T6SS production rate  $\lambda_s$ , i.e.,  $r'_0 = r_0 - c\lambda_s$ , where  $r_0$  is the base growth of the strain if it did not produce T6SS and  $c$  is the cost coefficient. More details of our ABM are provided in SI Appendix Section 4.

### **Model predictions and comparison with experimental data.**

**Slow activation rate limits T6SS effectiveness.** Results in the previous sections indicate that the relatively slower surface activation rate in FQ-A002 is an important factor that led to the observation that wildtype FQ-A002 is outcompeted by wildtype ES401 under unprimed conditions (Fig 2.2A-D). To test whether our model captures this experimental observation, we simulate competitions between ES401 and FQ-A002 and between their *vasa* mutants under unprimed and primed conditions, as in experiments presented in Fig 2.2A-D. We create different computational strains to represent ES401, FQ-A002, and

their *vasA*<sup>-</sup> counterparts, based on previously estimated parameters with several adjustments. T6SS parameters for simulated wildtype ES401 are  $(p_0, \lambda_+, \lambda_s, \lambda_f, \tau_{lys}) = (10\%, 0.6 \text{ h}^{-1}, 21 \text{ h}^{-1}, 6 \text{ h}^{-1}, 0.5 \text{ h})$ , and parameters for simulated wildtype FQ -A002 are  $(p_0, \lambda_+, \lambda_s, \lambda_f, \tau_{lys}) = (5\%, 0.25 \text{ h}^{-1}, 21 \text{ h}^{-1}, 6 \text{ h}^{-1}, 0.5 \text{ h})$ . To simulate a *vasA*<sup>-</sup> strain, we set  $\lambda_f = 0$  in corresponding wildtype strain so that the mutant cells cannot attack using T6SS but still pay a growth penalty for expressing T6SS proteins. More details on ABM parametrization in **Materials and Methods** and SI Appendix Section 4.

Using a square periodic domain, we simulate the interior of the colony in a wildtype ES401 vs. FQ-A002 coinubation in both unprimed and primed conditions for an equivalence of 24 h. These simulations exhibit spatial characteristics qualitatively similar to both unprimed and primed biological assays (Fig 2.2A-B). Averaging 100 simulations, under unprimed conditions, ES401 occupies  $99.7\% \pm 0.37\%$  of the total area, compared to 99.3% in experiment. In primed simulations, ES401 occupies  $50.1\% \pm 9.84\%$  of the total area, compared to 46.6% in experiment. Simulated coinubations of ES401 *vasA*<sup>-</sup> vs. FQ-A002 *vasA*<sup>-</sup> also capture the well-mixed spatial structure as observed in the corresponding biological assays (Fig 2.2C).

We observed that the slower surface activation leads to FQ-A002 being less effective than ES401 in eliminating nonlethal targets. To show this in the ABM, we simulate wildtype vs. *vasA*<sup>-</sup> pairs under unprimed conditions, similar to the experiments in Fig 2.2E. As shown in Fig 2.4, the *vasA*<sup>-</sup> strain coinubated with a slower activating lethal strain grows to a higher peak population, maintains a higher population, and survives for a longer time, compared to that growth with a faster activating lethal strain. At later times, as the lethal population reaches full activation and the contact among cells is fully established, the *vasA*<sup>-</sup> strains in both coinubations exhibit similar declining trends in the population. To test if the effect of activation speed persists when other T6SS parameters are perturbed, we perform additional simulations by keeping the respective activation rates for both slower and faster activating strains, and varying parameters  $\lambda_s$ ,  $\lambda_f$ , and  $\tau_{lys}$ .

When the lysis time is varied (Fig 2.4A), the initial increase and the peak of the target strain populations remain very similar ( $T \lesssim 2 \text{ h}$ ). Afterwards, the populations decline faster as  $\tau_{lys}$  decreases. This is because at the early stage of the coinubation, cells are randomly distributed, resulting in random contact between lethal and target cells. This is different from the later stage of the competition when the

colony is crowded and microcolonies have formed, when  $\tau_{lys}$  determines how long the dead cells stay intact and shield target cells from further T6SS attack. When  $\lambda_f$  and  $\lambda_s$  are varied (Fig 2.4B-C), we find that the slower activating lethal strain still gives the target strain a more favorable condition, allowing it to survive for longer and in higher numbers. However, under these parameter variations, the initial increase and the peak of the target populations exhibit a broad range of responses, unlike the case when  $\tau_{lys}$  is varied. After reaching the peak value, the target populations decline faster as either  $\lambda_f$  or  $\lambda_s$  increases. Taken together, these findings suggest that, for initially inactive, mutually lethal competitors, having a faster activation rate is a superior competitive strategy compared to having slower activation rate, regardless of variations in the lysis time, or the speed of sheath production and firing.

**Spatial environment of competition affects target survival.** Bacteria compete in many different arenas, including environments where cells have space to expand their range as competition occurs, and those where competition is limited to a confined space, e.g., host colonization sites. In simulating wildtype vs. *vasA*<sup>-</sup> competitions, we observe that the spatial environment plays a significant role in determining the survival of the target strain. In a confined spatial geometry, the target population eventually becomes completely eliminated by the wildtype strain (Fig 2.4). However, if the coincubation is allowed to grow in a range expansion, we find that a small population of target cells remain even after several hours of coincubation (Fig 2.5A). Even though the lethal cells can eliminate all target cells in the interior of the colony, a small number of target cells can survive at the edge of the coincubation spot because only target cells at the boundary of these microcolonies come into contact with lethal cells, allowing the target cells bordered by clonemates to grow into open territory and reproduce (Fig 2.5B, top).

The survival of target cells at the edge of a colony has also been consistently observed in the laboratory assays of lethal vs. target coincubation (Fig 2.5B, bottom), albeit at different size and time scales from the simulations. By performing a series of simulations of increasing system size, we show that the edge survival phenomenon can be consistently observed. However, as we expected, the numbers and sizes of the target strain microcolonies, and their temporal dynamics, vary depending on the initial conditions and likely other simulation parameters (SI Appendix Section 2). Importantly, these findings demonstrate the utility of our ABM to replicate competitive outcomes under different spatial restrictions that are ecologically relevant.

**Cost determines the competitive fitness of T6SS production strategies.** Variations in growth rates among bacterial strains can have significant impacts on competitive outcomes. While natural variations are common across bacterial strains, in this section, we focus our attention on isolating the effect of a growth penalty due to T6SS activity. We consider intraspecific competitions among two fully activated lethal strains with identical cost coefficient  $c$  and base growth rate  $r_0$ , but different T6SS production rate  $\lambda_s$ . We may expect a trade-off between the cost of T6SS production and its benefit in eliminating competitors.

We perform a parameter sweep using the ABM to understand the competitive fitness landscape in the context of the T6SS growth cost. We simulate a lethal resident strain with a fixed T6SS production rate of  $\lambda_{s, \text{res}} = 20 \text{ h}^{-1}$ , and a competitor strain with  $\lambda_{s, \text{comp}}$  varying in the range  $[0, \lambda_{s, \text{res}}]$ . To measure lethality of the competitor strain, we use a dimensionless parameter  $\beta = \lambda_{s, \text{comp}} / (\lambda_{s, \text{res}} + \lambda_{s, \text{comp}})$ . For the range of  $\lambda_{s, \text{comp}}$  that we consider,  $\beta \in [0, 0.5]$ . We also rescale the cost coefficient as  $\hat{c} = \frac{c}{c_{\text{max}}} \in [0, 1]$ , where  $c_{\text{max}} = r_0 / \lambda_{s, \text{res}}$ . To configure the competitor strain, we uniformly sample the parameter space of  $\{\beta, \hat{c} \mid 0 \leq \beta \leq 0.5, 0 \leq \hat{c} \leq 1\}$ . We assess the competitive outcome by  $\phi = (N_{\text{res}} - N_{\text{comp}}) / (N_{\text{res}} + N_{\text{comp}})$ , where  $N_{\text{res}}$  and  $N_{\text{comp}}$  are final cell counts of the resident and competitor strain, respectively.  $\phi = 1, 0, -1$  indicate resident strain dominance, coexistence, and competitor strain dominance, respectively.

In Fig 2.6A, we show competitive outcome  $\phi$  as a function of  $\beta$  and  $\hat{c}$ . In regions along the diagonal of parameter space of  $\{\beta, \hat{c}\}$ , the two competing strains can have different  $\lambda_s$  values but still coexist because they strike a similar balance in the growth vs. T6SS production trade-off. Above this diagonal region, the competitor strain (low producer) dominates, and below this diagonal, the resident strain (high producer) dominates. When  $\beta \approx 0.5$ , both strains coexist at any value of  $\hat{c}$  due to comparable T6SS production levels.

Comparing simulations from across the parameter space (Fig 2.6B), we find that there are various mechanisms through which one strain can dominate or coexistence can be achieved. When the cost of producing T6SS is low, the resident strain dominates by having a higher T6SS production, suppressing the faster growing competitor that maintains a smaller T6SS arsenal (Fig 2.6B, lower left). With cost being low, when two strains coexist, cells grow and interact in T6SS-dependent manners to

form spatially separated microcolonies, similar to what we observed in primed coinfections of wildtype ES401 vs. wildtype FQ-A002 (Fig 2.2B; Fig 2.6B, center to lower right). When the cost is high, the competitor strain dominates by outgrowing the resident strain, which pays a heavy price for producing many T6SS structures (Fig 2.6B, top left to center). With cost being high, cell growth can become extremely slow in high producers; thus, two competing strains coexist because the initial population barely grows to establish intercellular contacts (Fig 2.6B, top right).



## 2.3 Discussion.

Built upon *in vitro* experimental data, the biochemical model contains the most important variables in subcellular T6SS dynamics: (1) the speed of T6SS activation, and (2) the speed at which structures are built and fired during competition. Experimentally, we show that *V. fischeri* exhibits strain-specific variations in the speed of T6SS activation upon entering a viscous environment, and in the average number of T6SS structures cells harbor. We hypothesized that the difference in activation speed plays a dominant role in strain competition and survival: the faster activator (ES401) has a competitive advantage by taking the first shots. Using *in vitro* and *in silico* experimental data, we provide evidence to corroborate this hypothesis (Figs 2.2-2.5). When populations are fully activated at the start of competition, competing factors such as the speed at which T6SS structures are being generated and fired, and the cost of T6SS production, balance against one another in determining the competition outcome (Fig 2.6).

Although engineering lab mutants has become standard research practice, there are yet limitations in practical feasibility and controllability when probing a biological system. To systematically investigate the effects of the aforementioned T6SS-related factors on competition, we integrate the biochemical model into an ABM, and use it to generate and test hypotheses about T6SS activity that would be difficult to address experimentally. We systematically vary T6SS-related parameters in the ABM to study the trade-off between the biological cost of T6SS structure production and its competitive benefits (Fig 2.6). Although there have been estimates of the energetic cost of firing T6SS [57], the growth penalty of expressing T6SS remains unknown. However, the phase diagram in Fig 2.6 could be used as a tool to either predict the competitive outcome of two lethal strains if the growth cost of T6SS can be quantified or to predict the growth cost based on observed coinoculation results. Growth rate is only one potential cost of utilizing T6SS [94, 124]. Our model allows for the incorporation of different forms of cost, such as the arrested cell-cycle due to uptake of DNA of lysed prey cells [94], and DNA damage in T6SS expressing cells in the presence of environmental stressors [124].

Our ABM, combined with internal T6SS models, can be a very flexible investigative tool. It can take into account other T6SS activation mechanisms such as iron-dependent gene expression, appropriate temperatures, and quorum sensing [7] by incorporating diffusion and intercellular communication. It can also be modified to generate T6SS-related behavior such as the tit-for-tat strategy

[48, 113], reusing secreted proteins in sister cells [95], and feedback control of T6SS assembly via sensing intracellular levels of Hcp [125]. In addition to probing the biochemical parameters of T6SS, our model can be adapted to explore how bacteria may survive an encounter with a T6SS<sup>+</sup> competitor. Although several reports have described observations of protection against T6SS attacks [49, 87, 126-129], defensive mechanisms have yet to be parameterized in ABMs. Our model can be used to investigate T6SS resistance by including factors that lead to the emergence of diverse protective capabilities, which include those derived from heritable mechanisms, e.g. point mutations, gene amplification, and horizontal gene transfer, as well as physiological differences within a clonal population that are stochastic or influenced by hysteresis [130-132].

The ABM also enables us to investigate variables in competition not related to T6SS, such as changes in the geometry of the competition arena. The differences in target survival when competition occurs in a confined space and when it is in a range expansion (Fig 2.5) provide some insight into competitions occurring within a host. The simulation results suggest that if multiple strains enter a confined host colonization site, the target population may be quickly eliminated because it cannot avoid contact with the lethal strain. These results underscore the importance of considering the geometry of the competitive environment, which significantly influences the outcomes in addition to T6SS dynamics.

As a concluding remark, we have designed the T6SS biochemical model to be general and parsimonious, so that it can be adapted and applied to T6SSs in other microorganisms, serving as the foundation on which more complex T6SS biochemistry can be investigated. Combined with the ABM, our model can incorporate with ease new facets of T6SS-related mechanisms as they are discovered in this active area of research.

## 2.4 Material and Methods.

### Media and growth conditions.

*V. fischeri* strains were grown in LBS medium at 24°C, and antibiotics were added to media for *V. fischeri* selection as described previously [133]. For selection in *V. fischeri* cultures, chloramphenicol, kanamycin, and erythromycin were added to LBS medium at final concentrations of 2 µg mL<sup>-1</sup>, 100 µg mL<sup>-1</sup>, and 5 µg mL<sup>-1</sup>, respectively.

### Coincubation assays.

*V. fischeri* strains containing the indicated plasmid or chromosomal markers were grown overnight on LBS agar plates supplemented with the appropriate antibiotic at 24°C. For each biological replicate, overnight cultures were started from a single colony and grown overnight in LBS supplemented with the appropriate antibiotics. Prior to the start of coincubation assays, cultures were either subcultures once more into liquid LBS for 6 h (unprimed treatments) or spotted onto an LBS agar plate for 6 h (primed treatments) as indicated. For each coincubation, strains were normalized to an OD<sub>600</sub> of 1.0, mixed at a 1:1 ratio, and 5 µL of the mixture was spotted on LBS agar plates and incubated at 24°C. At the indicated time points, coincubation spots were either imaged using fluorescence microscopy, or total CFU counts were quantified using serial dilutions spotted onto media selective for the desired strain.

### Fluorescence microscopy.

Fluorescence microscopy images of coincubation spots were imaged with a trinocular zoom stereo microscopy equipped with a Nightsea fluorescence adapter kit for green and red fluorescence detection. Images were taken using an OMAX 14MP camera with OMAX TouPView camera control software. Single-cell images of VipA<sub>2</sub>-GFP sheaths were taken either on an upright Olympus BX51 microscope outfitted with a Hamamatsu C8484-03G01 camera and a 100X/ 1.3 Oil Ph3 objective lens with cells prepped on a standard 1 mm glass slide (Fig 2.3A), or on an inverted Nikon Ti2 microscope outfitted with a Hamamatsu ORCA Fusion sCMOS camera and a CFI plan apo lambda 100x oil objective lens with cells prepped on a 35 mm glass-bottomed dish (Fig 2.3B) [134]. Brightness and contrast adjustments were made uniformly across all images in a given experiment and color changes were made by adjusting the LUT value to either “green” for ES401 or “magenta” for FQ-A002 in FIJI. Parametrization of simulated ES401 and FQ-A002 in the ABM.

We use  $\tau_+ = 1$  h for both simulated ES401 and FQ-A002 strains because the activated percentage in either biological ES401 or FQ-A002 population starts to increase after 1 h, and the different in  $\tau_+$  estimates for the two strains is below our experimental time resolution (Fig 2.3B). The rate of surface activation in a biological strain depends on the experimental conditions. The particular experiments used to quantify this parameter made use of a sealed Petri dish for imaging (Fig 2.3B), which likely limited oxygen supply to the bacteria. As the experimental setups in Fig 2 and Fig 3AC are different from this, we increase the estimated activation rates of both ES401 and FQ-A002 (Fig 2.3) by five-fold while maintaining the ratio between the two. We base the value of  $\lambda_f \approx 21$  h<sup>-1</sup> in our computational strains on publicly available microscopy video data that visualize sheath assembly and firing in *V. cholerae* (21). The strain specific firing rates are determined by  $\lambda_f = \lambda_s / \bar{N}_\infty$ . We use the estimate  $\bar{N}_\infty = 3.5$  for both ES401 and FQ-A002, and the firing rates for the two strains are identically  $\lambda_f = 6$  h<sup>-1</sup>. For  $\tau_{lys}$ , we use an intermediate value, 0.5 h, which is between the limiting values in a previous study that investigates the effect of lysis speed on T6SS effectiveness [54]. Furthermore, we let  $\lambda_s$  and  $\tau_{lys}$  be identical in both simulated ES401 and FQ-A002 strains, because the two biological strains exhibit similar killing rates in coinoculation with nonlethal targets (Fig 2.2E). To simulate unprimed cells, after seeding the initial population at the start of the simulation, we randomly set a cell to be activated with probability  $\rho_0$ , and let the inactivated cells undergo stochastic switching as described in Eq. [1]. In contrast, to simulate primed cells, we set every cell in the initial population to be activated at the start. The base growth rate  $r'_0$  of the lethal strains are similar to those of biological strains ES401 and FQ-A002 [38]. The simulation domain in Fig 2.2A-C is 388  $\mu$ m x 388  $\mu$ m and has periodic boundary conditions; however, we only use the central domain of 200  $\mu$ m x 200  $\mu$ m to compute percentage of area occupied, in order to avoid edge effect. For a summary of ABM parameters, see SI Appendix Table 2.S1. For specific parameters used in Figs 2.2 & 2.6, see SI Appendix Tables 2.S2 & 2.S4, respectively. For specific parameters used in Figs 2.4 & 2.5, see SI Appendix Table 2.S3.

## 2.5 Figures.

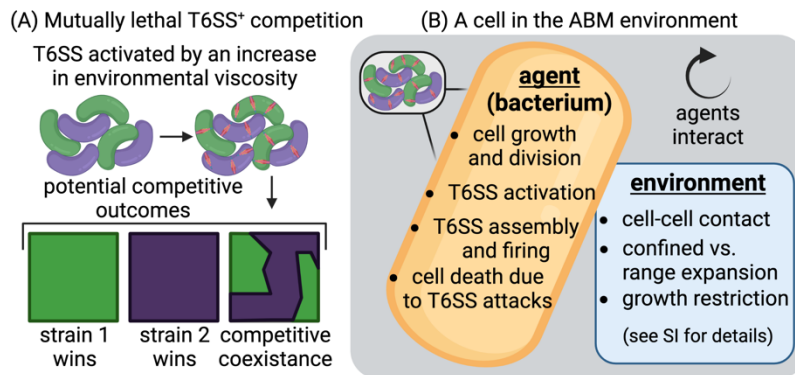


**Figure 2.1. Schematics of experimental and computational systems used in this study. (A)** A schematic of a coinoculation between two mutually lethal T6SS<sup>+</sup> strains of *V. fischeri* on agarose pads. Cells raised in liquid culture first undergo surface activation after plating. The competitive outcome depends on intraspecific physiological variations, such as activation rate, and the speed at which cells build and fire T6SS apparatuses. **(B)** A schematic of a computational cell in the in-house ABM environment. Besides cellular growth and division, a cell (or an agent) also undergoes internal reactions governed by the subcellular T6SS model, while subject to environment factors such as cell-cell contact, spatial confinement, growth restriction due to availability of space and nutrients. For more details of the ABM see SI Appendix Section 3 & 4. Figure was created using BioRender with a publication license.

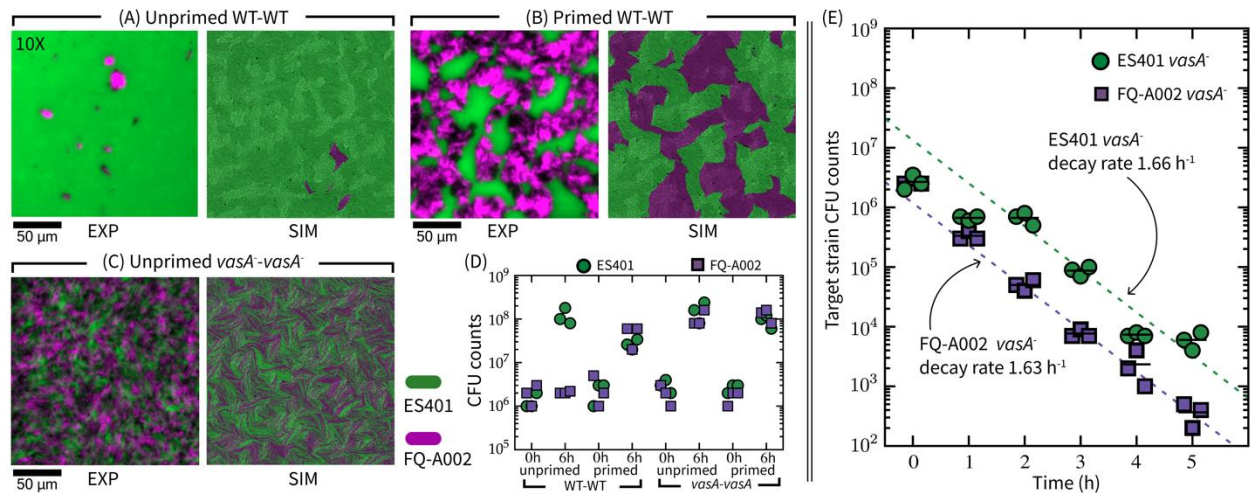


**Figure 2.2. Competition outcomes vary due to intraspecific variations in T6SS killing dynamics.**

**(A) – (C)** Fluorescence microscopy images of ES401 and FQ-A002 strains at 24 h following coincubation on LBS agar, compared side by side with representative ABM simulation images. The ES401 strain harbored the GFP-encoding plasmid pVSV102 (green) and the FQ-A002 strain harbored the dsRed-encoding plasmid pVSV208 (magenta). Microscopy images were taken at 10X; scale bars are 50  $\mu\text{m}$  for all microscopy and simulation images. **(A)** Wildtype (WT) vs. wildtype pair under unprimed treatment. In the microscopy images, ES401 occupied 99.3% of total area, and FQ-A002 0.7%. In simulations, ES401 occupied 99.7%, and FQ-A002 0.3%. **(B)** WT vs. WT pair under primed treatment. In the microscopy images, ES401 occupied 46.6% of the total area, and FQ-A002 53.4%. In simulations, ES401 occupied 50.1%, and FQ-A002 49.9%. **(C)** *vasA*<sup>-</sup> vs. *vasA*<sup>-</sup> pair under primed treatment gives similar outcomes to **(C)** experimentally; in simulation it is identical to *vasA*<sup>-</sup> vs. *vasA*<sup>-</sup> under unprimed treatment, hence not repeated. All experiments were performed three times; all simulations were repeated 100 times.

Additional experimental and simulation data can be found in SI Appendix Section 1, SI movies S1 & S2. Simulation parameters, see SI Appendix Tables 2.S1 & 2.S2. **(D)** Total colony forming unit (CFU) counts of each strain in coincubation at 0 h and 6 h following coincubation on LBS agar. **(E)** Total target strain CFU counts taken each hour for 5 h in unprimed coincubation between either wildtype FQ-A002 and ES401 *vasA*<sup>-</sup>, or wildtype ES401 and FQ-A002 *vasA*<sup>-</sup>. CFU data taken after time  $T \geq 2$  h of either strain is fit to an exponential decay model  $a \exp(-bt)$  with  $a$ ,  $b$  as fitting parameters. Data points at 0 h and 1 h are excluded. Decay rate  $b$  is reported for both strains.

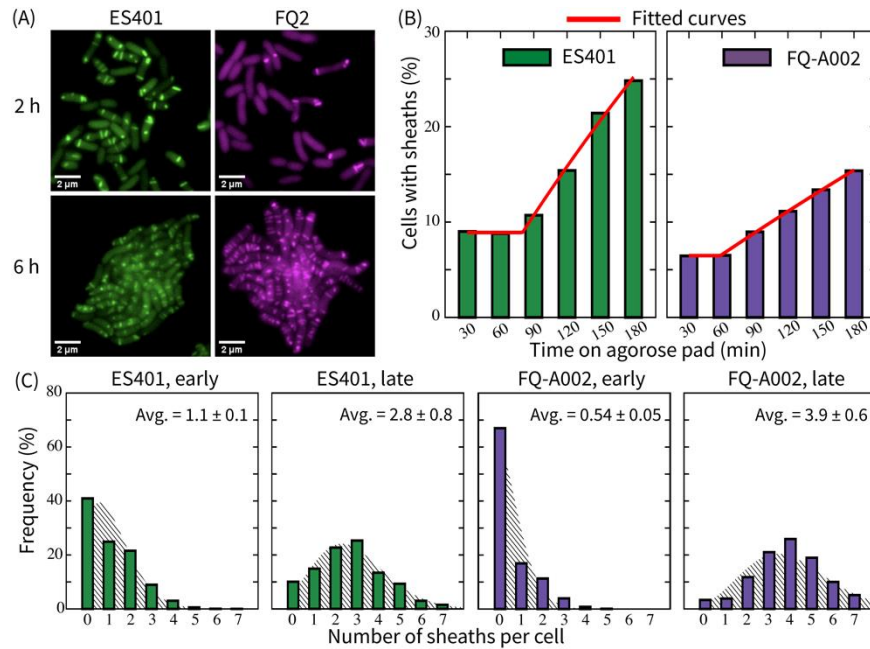


**Figure 2.3. *V. fischeri* exhibits strain-specific T6SS dynamics over time during surface activation.**

**(A)** Representative fluorescence microscopy images of ES401 (green) and FQ-A002 (magenta) cells harboring VipA-GFP expression vector after incubation on an agarose pad for either 2 h or 6 h. **(B)** Percentage of ES401 or FQ-A002 cells that contain at least one sheath at 30 min intervals for 3 h. A minimum of 680 total cells were analyzed for each treatment across five fields of view for two biological replicates. All combined data is shown. Parameters in Eq. [2] are estimated to be  $(\rho_0, \tau_+, \lambda_+) = (10\%, 1.34 \text{ h}, 0.118 \text{ h}^{-1})$  for ES401, and  $(\rho_0, \tau_+, \lambda_+) = (5\%, 1 \text{ h}, 0.05 \text{ h}^{-1})$  for FQ-A002. **(C)** Distribution of the number of VipA-GFP sheaths per cell in either ES401 or FQ-A002 at early (2 h) or late (6 h) stages of incubation on an agarose pad. These data are overlaid with a Poisson distribution with the corresponding mean. Chi-squared tests comparing the experimental distribution and the Poisson distribution yield, from left to right,  $P < .001$ ,  $P = .271$ ,  $P < .001$ ,  $P < .001$ . Chi-squared test comparing the two 6 h distributions yield  $P < .001$ . At least 2700 cells are analyzed for sheath distributions at 2 h, at least 260 cells are analyzed at 6 h. All agarose pads were made by supplementing liquid LBS with 2% agarose and 0.5 mM IPTG (isopropyl- $\beta$ -D-thiogalactopyranoside). **(A)** and **(C)** show data from the same experiments, repeated twice and all combined data are shown; **(B)** shows data from a separate experiment; for details see **Materials and Methods**.

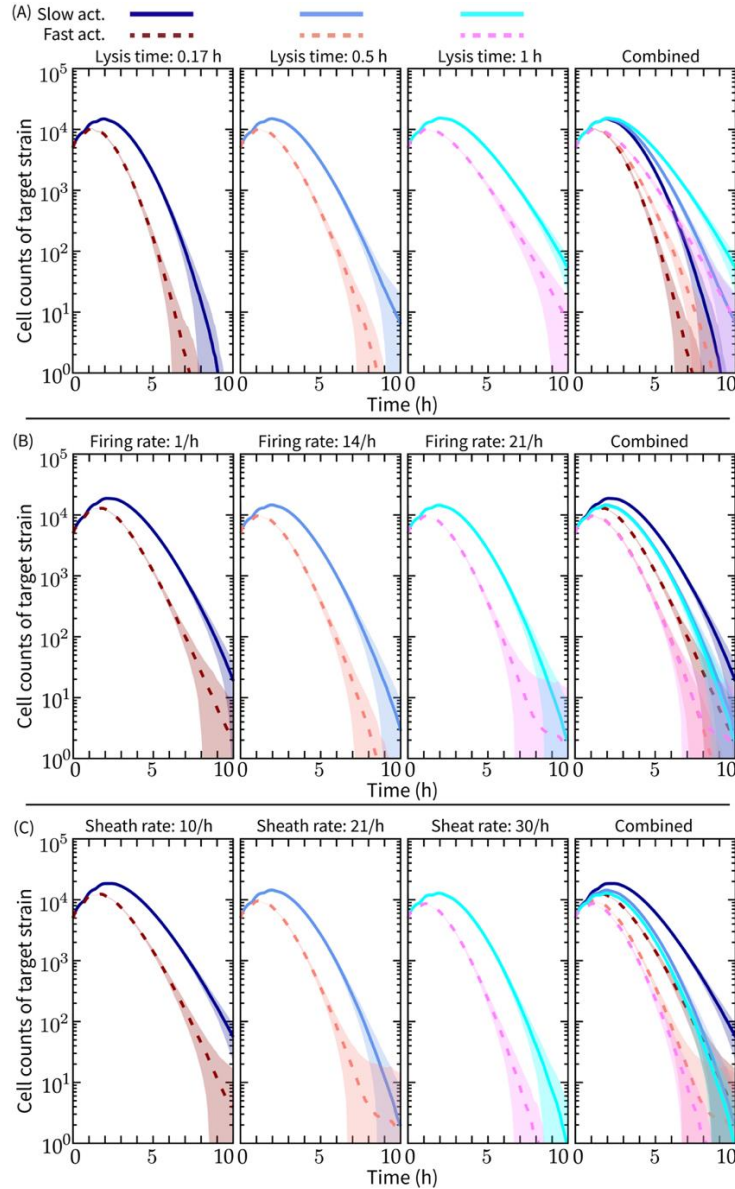


**Figure 2.4. The effect of activation rate on lethal vs. target competition is consistent when other T6SS parameters are perturbed.** A series of lethal vs. target co-cultures is simulated under unprimed conditions in confined spaces. In each scenario, two co-cultures are simulated and the target strain populations are compared: one co-culture has a faster activating lethal strain ( $\lambda_+ = 0.6 \text{ h}^{-1}$ ), and the other has a slower activating lethal strain ( $\lambda_+ = 0.25 \text{ h}^{-1}$ ). Only the target population curves are shown. All curves are averaged over 50 independent simulations. (A) While keeping  $\lambda_s = 21 \text{ h}^{-1}$ ,  $\lambda_f = 7 \text{ h}^{-1}$ , lysis time is varied  $\tau_{lys} = 0.17, 0.5, 1 \text{ h}$ , for 1<sup>st</sup>, 2<sup>nd</sup>, and 3<sup>rd</sup> subfigure, respectively. The last subfigure shows combined data. (B) While keeping  $\lambda_s = 21 \text{ h}^{-1}$ ,  $\tau_{lys} = 0.5 \text{ h}$ , firing rate is varied  $\lambda_f = 1, 14, 21 \text{ h}^{-1}$  across the first three subfigures, from left to right. (C) While keeping  $\tau_{lys} = 0.5 \text{ h}$ , sheath rate is varied  $\lambda_s = 10, 21, 30 \text{ h}^{-1}$ , across the first three subfigures, left to right. The last figure shows combined data. We set  $\lambda_f = \lambda_s$  in each scenario. For other simulation parameters, see SI Appendix Tables 2.S1 & 2.S3.



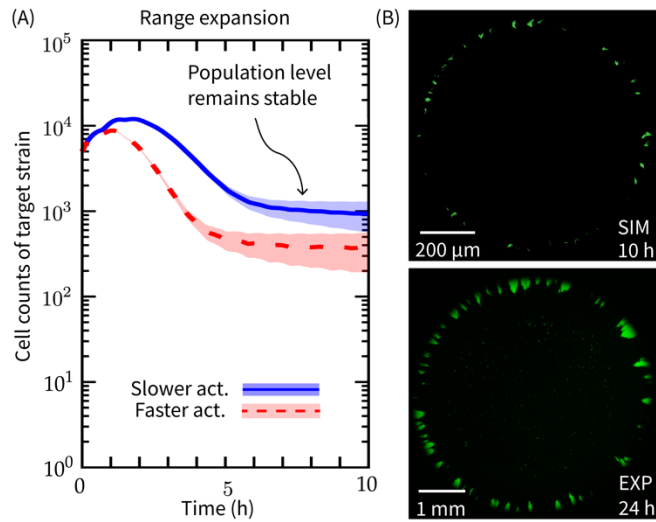


**Figure 2.5. Target strains survive longer when competing against slow activating lethal strains in a range expansion.** (A) The cell counts of a target strain over time when it is competed against two lethal strains in a range expansion; all results are averaged over 50 simulations. Colors correspond to the activation rate of the lethal strain in the co-cultivation: blue = lethal strain activates slower with ( $\lambda_+ = 0.25 \text{ h}^{-1}$ ), red = lethal strain activates faster with ( $\lambda_+ = 0.6 \text{ h}^{-1}$ ). The shaded region on each curve shows  $\pm 1$  standard deviation. (B) Top: a representative simulation image of the slow activating ( $\lambda_+ = 0.25 \text{ h}^{-1}$ ) lethal (hidden) vs. target (green) co-cultivation in range expansion. Scale bar is 200  $\mu\text{m}$ . Bottom: a fluorescence microscopy image of the ES114 target strain following a co-cultivation with the ES401 inhibitor strain; scale bar is 2 mm. Unprimed strains were mixed at a 1:1 ratio and co-cultivated for 24 h on LBS agar plates. For more details and simulation parameters, see SI Appendix Section 2, SI movie S3, and SI Tables 2.S1 & 2.S3.

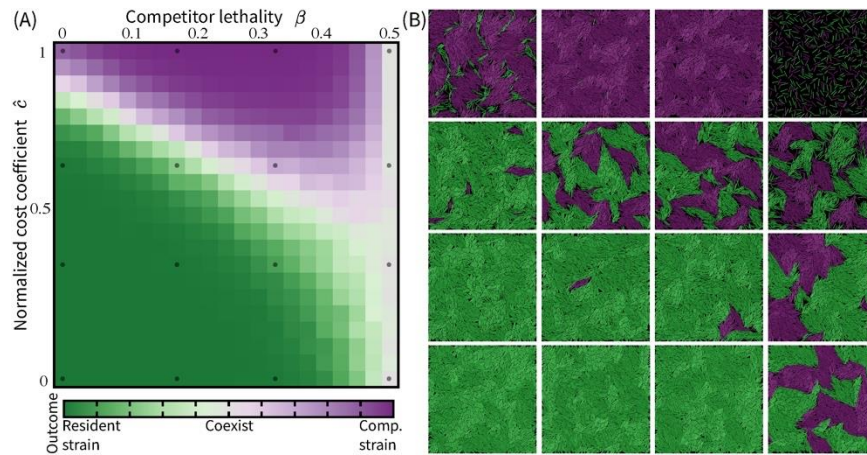


**Figure 2.6. Competitive outcomes and surviving mechanisms are affected by the cost of T6SS production.** (A) Phase space of competitive outcome in mutually lethal competitions as a function of two dimensionless parameters,  $\hat{\epsilon}$  and  $\beta$ , where  $\hat{\epsilon}$  is the normalized cost coefficient and  $\beta$  characterizes the lethality of the competitor strain. All simulations are run for an equivalence of 10 h. Final cell counts  $N_{\text{res}}$  and  $N_{\text{comp}}$ , for the resident and competitor strain, respectively, are collected and averaged over 50 independent trials for each parameter combination  $\{\beta, \hat{\epsilon}\}$ . The competitive outcome is determined by  $\phi = (N_{\text{res}} - N_{\text{comp}})/(N_{\text{res}} + N_{\text{comp}})$ , with  $\phi = 1, 0, -1$  indicating resident strain dominance, coexistence, and competitor strain dominance, respectively. (B) Representative simulation images from across the parameter space. For simulation parameters see SI Appendix Tables 2.S1 & 2.S4.

## CHAPTER 3 – *Vibrio fischeri* coculture results in horizontal gene transfer

### 3.1 Introduction.

Whether the interactions between microbe and host are beneficial or pathogenic, bacteria evolve to colonize new hosts through similar processes: DNA changes through either mutations or horizontal gene transfer, and the host environment selects for genotypes with the ability to colonize that host. Specific genes are often required for bacteria to colonize a given host, and it is predicted that these genes can be transferred between bacteria through the exchange of genetic material [135]. Horizontal gene transfer (HGT) mediates gene flow between bacterial populations through conserved mechanisms including transformation, transduction, and conjugation [18]. In particular, conjugation systems are distributed among diverse groups of bacteria and have been shown to play an important role in bacterial evolution [136, 137].

Conjugation broadly refers to the unidirectional transfer of DNA from a donor to a recipient and is characterized by the requirement for direct contact between live cells [138]. *oriT*-mediated conjugation systems are typically plasmid-encoded and rely on relaxase proteins to nick the origin of transfer (*oriT*) on the conjugative plasmid and transfers single-stranded DNA into the recipient cell [139]. When the conjugative plasmid integrates into the donor chromosome, this results in High-frequency recombination (Hfr) strains with the ability to donate chromosomal DNA, as has been described in *Escherichia coli* and other systems [140]. Traditional Hfr transfer is relaxase-dependent, initiates at the *oriT* site encoded by the conjugative plasmid, and transfers DNA from 5' to 3' into the recipient cell, resulting in continuous DNA strand that is transferred and recombined into the recipient chromosome [139]. This leads to transfer biases around the genome where only genes proximal and 3' to *oriT* are transferred at high frequencies [139]. Further, recipients of Hfr transfer do not typically inherit the entire conjugative plasmid, and as such, transconjugants do not acquire the ability to act as a DNA donor themselves [139]. Recently, several similar, but seemingly distinct, mechanisms of conjugation have been described in

*Mycobacterium* [21, 141-143]. In contrast to classical Hfr chromosomal DNA transfer, *Mycobacterium smegmatis* utilizes the type VII secretion system apparatus ESX-1 in both the donor and recipient rather than plasmid-encoded conjugative machinery [142]. Additionally, there is no obvious regional transfer bias; genomic markers are transferred as small, discontinuous sequences at similar frequencies regardless of their chromosomal location [144].

The specific genes required for either pathogenic or symbiotic interactions are often encoded on the chromosome as genomic islands, or “pathogenicity islands” that are presumed to have been acquired by horizontal gene transfer [145, 146]. Nakamura *et al.* used bioinformatics approaches to show that pathogenicity-related genes make up a disproportionately high percentage of horizontally-acquired genes in prokaryotes [147]. In order for any horizontally-acquired gene to be maintained in a bacterial population, it must confer an advantage to the recipient cell that is maintained under positive selection. This begs the question – how does bacterial gene transfer drive the evolution of symbiotic partnerships? One possibility is that the transfer of specific host-colonization factors can allow bacteria to rapidly adapt to colonize new hosts. Operational genes involved in competitive interactions, biofilm formation, and symbiosis are often encoded in transferrable elements. Although previous work has identified important roles for these same processes during host-colonization, little is known about how HGT and the evolution of symbiotic partnerships are intertwined. Furthermore, identifying the mechanisms by which bacteria evolve to colonize new hosts will make it possible to predict genetic risk factors for host-transition of both potential pathogens and beneficial microbes.

To better understand these fundamental mechanisms, we take advantage of the well-characterized light organ association between the Hawaiian bobtail squid, *Euprymna scolopes*, and its bioluminescent symbiont, *Vibrio fischeri* [148]. Although *V. fischeri* makes up < 0.1% of the bacterial seawater population, they are the only bacteria that encode genes required to colonize the Hawaiian bobtail squid host [149]. In exchange for nutrients, luminescence provided by *V. fischeri* in the light organ is thought to obscure the squid’s silhouette to protect it from predators who hunt at night [150]. Given that *V. fischeri* is the only species of bacteria to have been isolated from the Hawaiian bobtail squid light organ, this symbiosis provides a natural, simplified microbial community that makes it possible to answer fundamental questions about the relationships between host and symbiont. Importantly, this symbiosis

must be established with each generation of squid; juveniles hatch without their symbionts, which are quickly acquired from the surrounding seawater [149]. Environmental acquisition of symbionts means that with each generation of squid hatched in the wild, newly evolved bacteria have the opportunity to compete for colonization of the light organ.

Although *V. fischeri* is the only bacterial species that has been cultured from the light organs of adult *E. scolopes*, not all strains of this species are capable of colonizing the Hawaiian squid host. For example, *V. fischeri* strain MJ11, a light organ symbiont of the Japanese pinecone fish *Monocentris japonica*, lacks essential host specificity factors that are required for colonization of the Hawaiian squid host. Two independent studies used different approaches to introduce genetic changes to MJ11 that allowed it to colonize the Hawaiian squid. Mandel et al. found that expressing an allele of the regulatory protein RscS allowed MJ11 to fully colonize the squid host [31]. The RscS regulator, found in all squid-colonizing *V. fischeri* isolates, turns on expression of the *syp* biofilm regulator, which was previously shown to be essential for forming aggregates on the surface of the light organ during the initial colonization process [151]. More recently, Pankey et al. clonally evolved MJ11 cells in repeated exposures to the Hawaiian squid host and selected for natural mutations that permitted host colonization. This study found that juvenile squid selected for MJ11 cells contained point mutations in a repressor of the *syp* locus, resulting in enhanced biofilm formation required for colonizing the squid host [152]. These studies revealed that even small genomic changes in *V. fischeri* can alter gene expression to facilitate colonization of a new host.

The studies described above were important to show that non-native *V. fischeri* strains can be genetically engineered or clonally evolved to colonize a new host; however, they did not use natural DNA exchange mechanisms to account for how HGT within a population may allow bacteria to alter or expand their host range. Previous work has described two mechanisms by which *V. fischeri* strains can exchange DNA through either natural transformation or plasmid-mediated conjugation [41, 42, 66]. Natural transformation machinery is conserved in *V. fischeri*, although it requires the addition of chitin or overexpression of the *tfoX* gene to induce competence in culture [41]. Conjugative plasmids have been shown to be strain-specific in *V. fischeri*; while the squid isolate MJ11 lacks a conjugative plasmid, the

commonly used squid isolate *V. fischeri* ES114 encodes a native conjugative plasmid that is referred to as pES100 [42, 153, 154].

Here, we design and implement an experimental evolution assay to select for the horizontal transfer of selectable antibiotic resistance markers between *V. fischeri* strains ES114 and MJ11. We propose that this assay could be optimized and used as a tool in future work to select for evolved genotypes that have acquired different phenotypic traits, including the ability to colonize new hosts. Further, we present preliminary evidence that *V. fischeri* exchanges DNA markers through an unidentified mechanism of gene transfer in conventional coculture conditions.

## 3.2 Results.

### Experimental Evolution Assay Design.

We first asked whether we could detect the transfer of selectable markers between live cells during an experimental evolution assay. Although previous work has described the ability of *V. fischeri* to exchange chromosomal DNA via natural transformation, and plasmid DNA via *oriT*-mediated conjugation, it was unknown whether DNA could also be exchanged during typical interactions between live cells in coculture [41, 42]. We designed an experimental evolution assay that would detect the transfer of selectable antibiotic-resistance markers between *V. fischeri* strains ES114 and MJ11 (Fig 3.1). While ES114 is a native light organ symbiont of the Hawaiian bobtail squid (*Euprymna scolopes*), MJ11 was isolated from the light organ of a Japanese pinecone fish, *Monocentris japonica*, and is unable to naturally colonize squid.

Both strains encode genes required for natural transformation, although previous work has shown that competence of *V. fischeri* requires either chitin or overexpression of the regulatory gene *tfoX*, and is not induced under the media conditions used here [41]. This experimental setup was designed to exclude natural competence so that we could study DNA exchange mechanisms that may not have been identified yet in *V. fischeri*. Importantly, ES114 harbors a native conjugative plasmid, pES100, which encodes a functional type IV secretion system (T4SS) [42, 154], that is absent in strain MJ11 [31]. In rare events, conjugative plasmids are known to integrate into the host bacterial chromosome and promote transfer of chromosomal DNA into a recipient cell [23, 155]. During these events, conjugative plasmids typically integrate into a stable location in the host chromosome, resulting in variable rates of transfer of selectable markers that are introduced around the donor chromosome. While the conjugal transfer of plasmid DNA has been reported in *V. fischeri*, we have not previously observed chromosomal DNA exchange in coculture [42]. We hypothesized that if ES114 donates chromosomal DNA via the chromosomal integration of pES100, we would observe variable transfer frequencies of selectable markers at different locations around ES114's chromosome I and II.

### Transfer frequency is not dependent on the location of chromosomal markers in ES114.

To test this, we first introduced an *Erm*<sup>R</sup> selectable marker onto the chromosome of ES114 via a Campbell insertion at four different locations across chromosomes I and II, resulting in strains SS101,

SS112, SS113, and SS104 (Fig 3.2A). To determine whether the Campbell insertion impacts transfer frequency, we also included strain DMA420, an ES114 transposon mutant with an *Erm<sup>R</sup>* marker in the same location as strain SS101 (Fig 3.2A) [156]. We next introduced the *Cam<sup>R</sup>* plasmid pVSV208 into strain MJ11. Overnight cultures of each strain were grown up clonally under the appropriate antibiotic selection prior to the experimental evolution assay. For each treatment, 2  $\mu$ L of Strain 1 and Strain 2 overnight cultures were used to inoculate 1 mL of liquid LBS medium and coincubated for 24 h at 24°C without shaking (Fig 3.1), where live cells had the opportunity to interact and exchange selectable markers. Following the experimental evolution period, serial dilutions of mixed cultures were plated onto three different antibiotic selections: (1) LBS + *Erm*, to quantify total Strain 1 CFUs; (2) LBS + *Cam*, to quantify total Strain 2 CFUs; and (3) LBS + *Erm* + *Cam*, to quantify and isolate evolved genotypes that had acquired the opposite selectable marker (Fig 3.1). As controls to test for spontaneous antibiotic resistance, each donor and recipient strain was also incubated clonally and serial dilutions were plated onto the same antibiotic selections described above. No colonies were detected on the double-antibiotic selection from treatments where Strain 1 or Strain 2 was incubated clonally, indicating that spontaneous antibiotic resistance was below the level of detection used in our experimental setup (Fig 3.2B; Table 3.1).

If DNA transfer in *V. fischeri* depends on the chromosomal integration of the conjugative plasmid pES100 followed by *oriT*-mediated conjugation, then we would expect to see different rates of transfer when ES114 (Strain 1) is marked at different locations around the chromosome. Instead, we observed that experimental evolution assays between *V. fischeri* MJ11 harboring a *Cam<sup>R</sup>* plasmid marker and each of the chromosomally-marked *V. fischeri* ES114 derivative strains resulted in transfer of the selectable markers at similar rates between each treatment, according to a 2-way ANOVA followed by a Tukey's multiple comparisons test (Fig 3.2B). While these results do not explicitly exclude the chromosomal integration of pES100 as a mechanism of transfer, they do suggest that transfer frequency is not dependent on the location of chromosomal markers in ES114, which would be unexpected from a traditional *oriT*-mediated transfer mechanism. One alternative explanation for these results could be a case where the ES114 conjugative plasmid pES100 is first acquired by MJ11, resulting in evolved MJ11



cells that have gained the ability to donate the Cam<sup>R</sup> selectable plasmid marker back to Erm<sup>R</sup>-marked ES114 cells.

### **Selectable markers are transferred between ES114 and distantly related *Vibrios* (KB8)**

The experiments described above indicate that *V. fischeri* is able to exchange selectable markers between closely-related strains; however, we wondered whether we could also detect interspecies DNA transfer between *V. fischeri* and another ecologically-relevant bacterial species. Strain KB8 was isolated from the water-column of Kaneohe Bay, HI, and was identified as a *Vibrio* sp. We also chose SS113 as a representative chromosomally-marked ES114 strain to be used throughout the manuscript. Using the same experimental evolution assay described above, we coincubated SS113 with either MJ11 or KB8 strains harboring the Kan<sup>R</sup> plasmid pVSV102, and also included treatments where SS113, MJ11, or KB8 were incubated clonally to ensure that we did not detect any spontaneous antibiotic resistance. As before, we observed no growth on the double-antibiotic selection plates from clonal incubations (Fig 3.3; Table 3.1). However, selectable markers were transferred between SS113 and KB8 at similar frequencies as were observed between SS113 and MJ11 (Fig 3.3). These results suggest that the DNA transfer we observe here is not confined to intraspecies interactions between *V. fischeri*, but that this may serve as a mechanism for *V. fischeri* to exchange DNA with more diverse microbes.

### **Conditions for transfer are not consistent with any reported HGT mechanisms in *V. fischeri*.**

Our experimental evolution assay was designed with the assumption that natural transformation in *V. fischeri* is not active under the coincubation conditions used here [41]. We initially anticipated that ES114 might donate chromosomal markers via integration of its native conjugative plasmid, pES100; however, the consistent transfer frequency of *Erm*<sup>R</sup> markers located at different points around ES114's chromosome would contradict what is known about *oriT*-mediated transfer in other systems [20, 42, 157]. To better understand how selectable antibiotic-resistance markers are exchanged in *V. fischeri*, we designed a series of experiments to test different conditional requirements for DNA transfer between SS113 and MJ11. For each experiment, clonal incubations of SS113 or MJ11 harboring the Cam<sup>R</sup> pVSV208 plasmid were included as negative controls, and no spontaneous double-antibiotic resistance was detected (Fig 3.4; Table 3.1).

While transduction has not been described in *V. fischeri* in culture, we predicted that if SS113's *Erm<sup>R</sup>* chromosomal marker was transferred to MJ11 via transduction, then cell-free spent media may be sufficient donor material to observe transfer. First, we coincubated MJ11 pVSV208 with either SS113 as described above, or 1 mL of cell-free supernatant resulting from an MJ11 + SS113 coincubation that was passed through a 0.22  $\mu$ m filter prior to the experimental evolution assay. While we detected transfer between live cultures of MJ11 pVSV208 and SS113, the cell-free supernatant was not sufficient donor material for MJ11 pVSV208 to receive the *Erm<sup>R</sup>* chromosomal marker (Fig 3.4A). These data suggest that the DNA transfer we observe here is not driven by transduction.

Although we did not expect natural competence to be active in our experimental evolution assay conditions due to the absence of chitin or overexpression of *tfoX* in either Strain 1 or Strain 2, the genes required for transformation are conserved in *V. fischeri* [41]. To test whether low-frequency natural transformation could explain the DNA transfer observed here, we incubated MJ11 pVSV208 with either SS113, or 2  $\mu$ g of SS113 gDNA and repeated the experimental evolution assay. We again detected transfer between live cultures of MJ11 pVSV208 and SS113, but the SS113 gDNA was not sufficient donor material for MJ11 pVSV208 to receive the *Erm<sup>R</sup>* chromosomal marker (Fig 3.4B). This is consistent with previous work which showed that natural transformation in *V. fischeri* is inactive under these culture conditions, and suggests that natural transformation is not driving the DNA transfer observed in our experimental evolution assays [41]. However, it is important to note that although gDNA was not a sufficient donor source, we have not ruled out the possibility that another mechanism is initiating DNA transfer via the conserved natural transformation machinery in *V. fischeri*.

To better understand genetic factors that drive gene transfer in *V. fischeri*, we next asked whether *recA* was required in either Strain 1 or Strain 2 in order to observe the transfer of selectable markers. We introduced a *recA<sup>-</sup>* mutation into both the chromosomally-marked *Erm<sup>R</sup>* SS113 strain and MJ11 harboring the *Cam<sup>R</sup>* pVSV208 plasmid. We coincubated SS113 with the MJ11 *recA<sup>-</sup>* mutant harboring pVSV208 and did not detect any transfer of the selectable *Erm<sup>R</sup>* or *Cam<sup>R</sup>* markers (Fig 3.4C). However, when we coincubated the SS113 *recA<sup>-</sup>* mutant with MJ11 pVSV208, we detected transfer of the selectable markers at frequencies similar to our positive control treatment of SS113 coincubated with MJ11 pVSV208 (Fig

3.4C). Taken together, these data suggest that to exchange selectable markers, *V. fischeri* requires *recA* in the plasmid-marked Strain 2, but not in the chromosomally-marked Strain 1.

Finally, we sought to investigate culture conditions that may affect transfer frequency in *V. fischeri*. Using SS113 and MJ11 pVSV208 as Strain 1 and Strain 2, respectively, we repeated our standard experimental evolution assay as described above and introduced different modifications to the assay with each treatment. First, the SS113 culture was heat-killed during a 15-minute incubation at 95°C prior to coincubation with MJ11 pVSV208, which resulted in no detectable transfer of the selectable markers (Fig 3.4D). Next, we replaced the 24 h coincubation step in liquid LBS media with a coincubation on LBS agar for the same period of time. When SS113 and MJ11 pVSV208 were coincubated on LBS agar, we detected transfer of the selectable markers at similar frequencies to treatments in liquid LBS (Fig 3.4D). In our last treatment, we repeated the coincubation step on LBS agar, but separated Strain 1 and Strain 2 using a 0.22  $\mu\text{m}$  filter. When cultures of SS113 and MJ11 pVSV208 were physically separated by the filter during coincubation, we did not detect any transfer of the selectable markers (Fig 3.4D). Taken together, these results suggest that DNA transfer in *V. fischeri* requires contact between live cells to occur. Further, this suggests that the DNA transfer we observe here could be a form of conjugation, characterized by a requirement for cell-cell contact, although it is unclear from this data whether it might be mediated by the conjugative plasmid pES100 as we initially predicted.

### 3.3 Discussion.

As bacteria transition from free-living to host-associated life stages, they are often forced into physical contact with both closely-related and diverse microbes. Thus, the host environment provides a unique opportunity for bacteria to compete and exchange DNA via contact-dependent mechanisms. The light organ of the Hawaiian bobtail squid, *Euprymna scolopes*, is often used as a simple model for studying host-colonization processes because the light organ is exclusively colonized by its bioluminescent symbiont, *Vibrio fischeri*. Recent work has begun to investigate interactions between *V. fischeri* strains throughout the colonization process and during coincubation; however, much of this work has focused on competitive mechanisms. Despite *V. fischeri* encoding both conserved natural transformation machinery and strain-specific conjugative plasmids, we know very little about how *V. fischeri* cells might exchange DNA during physical interactions with other strains or species of bacteria. In this study, we describe an experimental evolution assay that utilizes selectable antibiotic resistance markers to quantify DNA transfer in *V. fischeri*. Because we were interested in contact-dependent DNA exchange, we used culture conditions in which natural transformation is known to be inactive in *V. fischeri*. We selected for evolved genotypes that had acquired a selectable marker across various treatments and found that (1) Coculture results in the transfer of selectable markers both between *V. fischeri* strains and between *V. fischeri* and more diverse *Vibrio* species; and (2) the mechanism driving this gene transfer is inconsistent with any HGT mechanisms that have been previously described in *V. fischeri*.

The experimental evolution assay that we describe was designed so that the evolved phenotype for selection is the acquisition of an antibiotic resistance cassette. We propose that this assay could be modified to select for any number of evolved traits given that a counterselection for the donor genotype can be used. One avenue for future research could include using this assay to determine host-colonization factors. The *V. fischeri* MJ11 strain used in this study was isolated from the light organ of a Japanese pinecone fish and is unable to naturally colonize the Hawaiian bobtail squid, *E. scolopes*. In this example, MJ11 would be coincubated with a native *E. scolopes* isolate such as *V. fischeri* ES114. Rather than selecting for evolved isolates using a double antibiotic selection, the coculture would be used as inoculum in a squid colonization assay with a counterselection against ES114. Since MJ11 is unable to

naturally colonize the squid, we would expect that any genotypes that are isolated from colonized squid would represent MJ11 that acquired genetic factor(s) that are required to colonize *E. scolopes*. The genomes of the evolved genotypes of interest would then be sequenced and compared to the parent genomes to identify genes that were either acquired or lost that result in the ability to colonize a new host.

At this point it remains unknown whether additional chromosomal or plasmid DNA is acquired along with the selectable marker, or the mechanism by which *V. fischeri* exchanges DNA in coculture. Given the data we present here, it is plausible that either (1) ES114 donated its *Erm<sup>R</sup>* chromosomal marker to MJ11 and KB8 via an undetermined mechanism of transfer, and/or (2) MJ11 and KB8 acquired the conjugative plasmid pES100 from ES114 and subsequently transferred the *Cam<sup>R</sup>* plasmid marker back to ES114. Interestingly, previous work studying conjugation in *V. fischeri* found that plasmid transfer required *recA* in the donor strain, but not in the recipient strain [42]. We reported here that to detect transfer of selectable markers, *recA* was required in the plasmid-marked Strain 2, but not in the chromosomally-marked Strain 1 (Fig 3.4C). We initially interpreted these results to mean that *recA* was required in the “recipient” (plasmid-marked Strain 2) but not the “donor” (chromosomally-marked Strain 1); however, these results would also be consistent with our second hypothesis that Strain 2 received pES100 and then gained the ability to act as a donor, thus requiring *recA* in Strain 2.

To clarify these unknowns and to better understand the mechanism of DNA transfer we observed here, future studies should include hybrid Illumina-Nanopore sequencing of evolved genotypes. Evolved genome sequences should be compared to both input parent sequences to determine the direction of horizontal gene transfer, and to quantify any DNA transfer that occurred in addition to the exchange of the selectable markers. For example, an evolved genotype that is most similar to MJ11 or KB8 but includes the *Erm<sup>R</sup>* marker would support our first hypothesis described above, while an evolved genotype that is most similar to ES114 but includes that *Cam<sup>R</sup>* selectable plasmid would support our second hypothesis. Hybrid genomes will be important to resolve the spatial distribution of any potential DNA acquisition and will provide crucial information about the mechanism by which *V. fischeri* exchanges DNA in coculture. Patterns of gene transfer to look for would include the acquisition of multiple, discontinuous segments of DNA, which would be indicative of a mechanism similar to the Distributive Conjugal Transfer (DCT) that has been described in *Mycobacterium*. Ultimately, this work provides evidence that *V. fischeri* exchanges

DNA in conventional coculture conditions and this mechanism warrants further study and characterization so that it may be exploited as a useful tool in studying how *V. fischeri* evolved in host-like conditions when cells come into physical contact with one another.

### 3.4 Material and Methods.

#### Media and growth conditions.

*V. fischeri* strains were grown in LBS or ASWT medium at 24°C and *E. coli* strains were grown in either LB medium or Brain Heart Infusion (Difco) at 37°C. Antibiotic selection for *V. fischeri* and *E. coli* strains were as described previously [42]. Plasmids with the R6Ky origin of replication were maintained in *E. coli* strain DH5αλpir [42] and plasmid pEVS104 [158] was maintained in strain CC118λpir [159]. All other plasmids were maintained in *E. coli* strain DH5α [160].

#### Molecular techniques.

PCR was performed on a Mastercycler pro (Eppendorf) using Phusion High-fidelity DNA polymerase (New England Biolabs). PCR products were purified using the DNA Clean and Concentrator-5 kit (Zymo Research, Orange, CA). Plasmids were isolated using the ZR Plasmid Miniprep Classic Kit (Zymo Research, Orange, CA). DNA was extracted using the ZR Fungal/Bacterial DNA Miniprep Kit (Zymo Research, Orange, CA). DNA concentration was measured with a BioSpectrometer basic (Eppendorf). Sequencing was performed through Eton Biosciences.

#### Strain and plasmid construction.

For chromosomal tagging of *V. fischeri* ES114, alleles were mobilized on plasmids into the ES114 recipient by triparental mating using CC118λpir pEVS104 as a conjugative helper. Chromosomally-tagged strains were screened for the appropriate antibiotic resistance markers and verified using PCR. All primer design was based on the ES114 genome sequence unless otherwise noted were synthesized by Eton Biosciences. The MJ11 recipient was tagged for coincubation assays with either pVSV102 (Kan<sup>R</sup>, GFP+) or pVSV208 (Cam<sup>R</sup>, dsRed+) [66].

To chromosomally-tag ES114 on chromosome I, approximately 0.5 kb of the gene VF\_0608 was PCR amplified using primers SS131 and SS132 from ES114 gDNA. The resulting PCR product was cloned into the KpnI site of plasmid pEVS122, resulting in the VF\_0608 disruption construct, pBS101. The VF\_0608 disruption construct on pBS101 was moved into strain ES114, resulting in strain SS101.

To chromosomally-tag ES114 in a second location on chromosome I, approximately 0.5 kb of the gene VF\_2408 was PCR amplified using primers SS133 and SS134 from ES114 gDNA. The resulting PCR product was cloned into the KpnI site of plasmid pEVS122, resulting in the VF\_2408 disruption

construct, pBS102. The VF\_2408 disruption construct on pBS102 was moved into strain ES114, resulting in strain SS112.

To chromosomally-tag ES114 on chromosome II, approximately 0.5 kb of the gene VF\_A0239 was PCR amplified using primers SS135 and SS136 from ES114 gDNA. The resulting PCR product was cloned into the KpnI site of plasmid pEVS122, resulting in the VF\_A0239 disruption construct, pBS103. The VF\_A0239 disruption construct on pBS103 was moved into strain ES114, resulting in strain SS113.

To chromosomally-tag ES114 in a second location on chromosome II, approximately 0.5 kb of the gene VF\_A1037 was PCR amplified using primers SS137 and SS138 from ES114 gDNA. The resulting PCR product was cloned into the KpnI site of plasmid pEVS122, resulting in the VF\_A1037 disruption construct, pBS104. The VF\_A1037 disruption construct on pBS104 was moved into strain ES114, resulting in strain SS104.

To construct the Erm<sup>R</sup>-marked ES114 relaxase mutant (SS126), approximately 0.5 kb of the relaxase gene (VF\_B0050) was PCR amplified using primers SS129 and SS130 from ES114 gDNA. The resulting PCR product was cloned into the Cam<sup>R</sup> plasmid pEVS118, resulting in the relaxase disruption construct, pBS100. The relaxase disruption construct on pBS100 was moved into strain SS113, resulting in strain SS126.

### **Experimental evolution assays.**

Cultures of *V. fischeri* strains grown in LBS broth supplemented with the appropriate antibiotic at 24°C were diluted to an OD<sub>600</sub> of 1.0, and 2 µl of the mixture was transferred into 24-well plates containing 1 mL of liquid LBS medium and incubated at 24°C without shaking. After a 24 h coinubation period, Strain 1 and Strain 2 (as indicated) strains were quantified by plating serial dilutions onto LBS plates supplemented with antibiotics selective for each individual strain. Evolved transformants were isolated and transfer frequency of either chromosomal or plasmid DNA (as indicated) was quantified by plating serial dilutions onto LBS plates supplemented with antibiotics selective for both the Strain 1 and Strain 2 markers. Transfer frequency was calculated by dividing the transformant CFUs by total CFUs.



### 3.5 Figures.

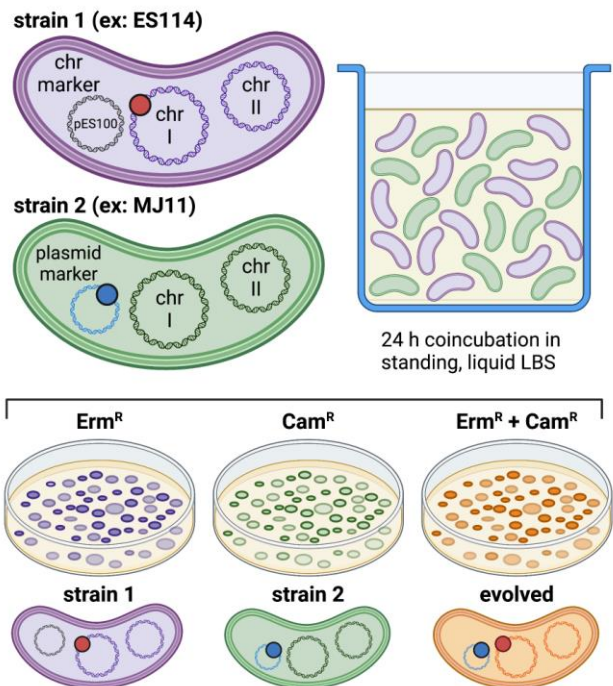


**Figure 3.1. Experimental evolution assay.** A selectable Erm<sup>R</sup> marker (red circle) was introduced to a neutral location in Strain 1, while Strain 2 harbored the selectable Cam<sup>R</sup> vector pVSV208 (blue circle). Overnight cultures of Strain 1 and Strain 2 were sub-cultured into standing, liquid LBS medium and incubated together for the duration of the experimental evolution assay. Following the 24 h assay period, serial dilutions of the mixed culture were plated onto LBS agar plates supplemented with either (1) Erm, to quantify Strain 1 CFUs; (2) Cam, to quantify Strain 2 CFUs; or (3) Erm + Cam, to quantify and isolate evolved strains that acquired the opposite selectable marker. Figure was created using BioRender with a publication license.

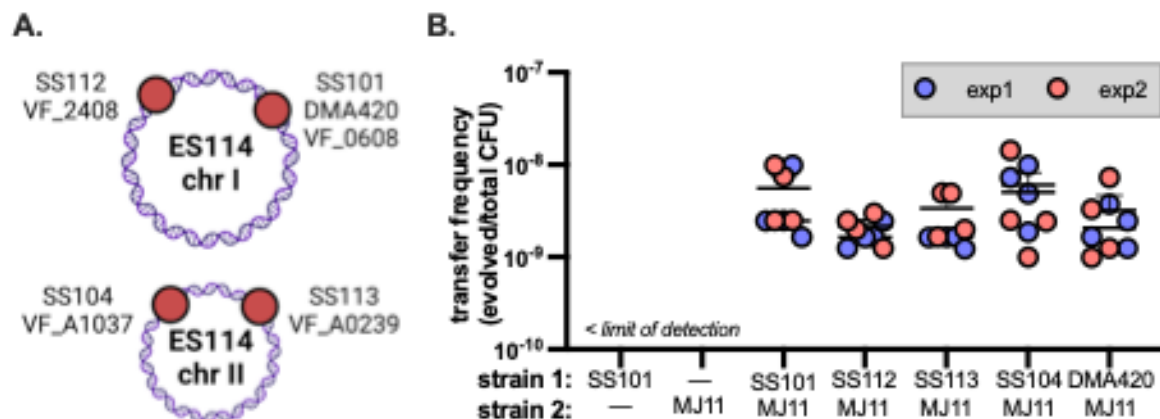


**Figure 3.2. Transfer frequency is not dependent on the location of chromosomal markers in ES114.** **A.** Location of chromosomal markers introduced into ES114. **B.** Transfer frequency of selectable markers between ES114 (Strain 1;  $Erm^R$  markers introduced around the chromosome) and MJ11 (Strain 2; harbors  $Cam^R$  pVSV208 marker). Transfer frequencies were calculated by dividing the Evolved CFU by the Total CFU. All experimental evolution assays were performed twice ( $n = 4$ ) and all data is shown; each color represents data from a separate experiment. Averaged transfer frequencies can be found in Table 3.1. Limit of detection is 200 evolved CFU/mL. Panel A was created using BioRender with a publication license.

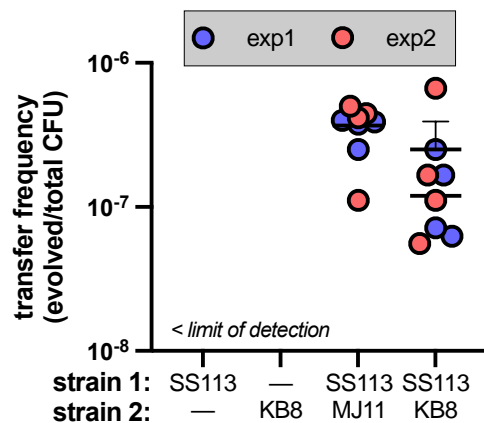


**Figure 3.3. *V. fischeri* exchanges selectable markers with *Vibrio* sp. KB8.** Transfer frequency of selectable markers between SS113 (Strain 1; ES114 harboring an  $\text{Erm}^R$  marker at VF\_A0239) and KB8 or MJ11 harboring the  $\text{Cam}^R$  pVSV208 marker (Strain 2). Transfer frequencies were calculated by dividing the Evolved CFU by the Total CFU. All experimental evolution assays were performed twice ( $n = 4$ ) and all data is shown; each color represents data from a separate experiment. Averaged transfer frequencies can be found in Table 3.1. Limit of detection is 200 evolved CFU/mL.

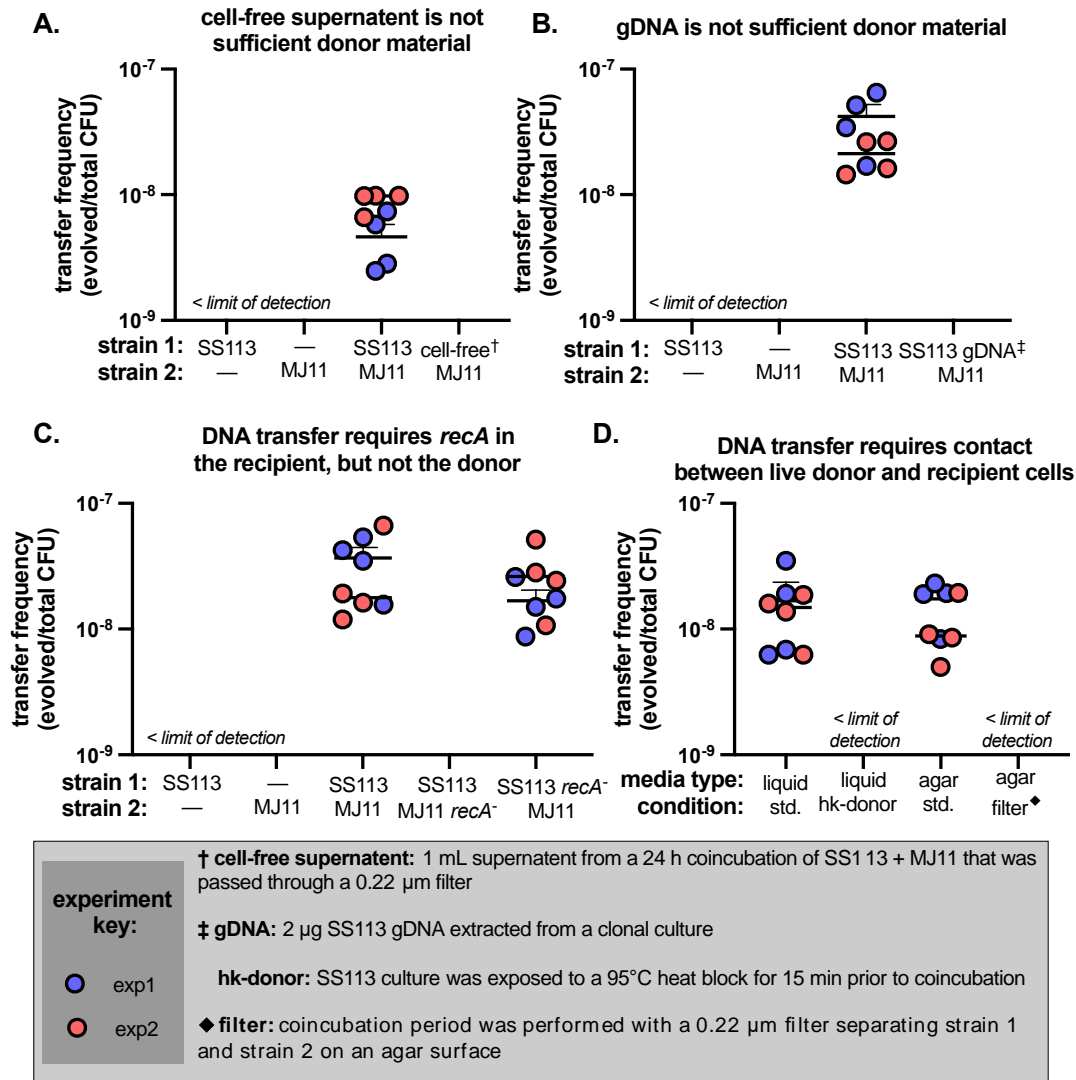


**Figure 3.4. Conditional requirements for DNA transfer in *V. fischeri*.** Transfer frequencies of selectable markers when either **(A)** cell-free supernatant from a coinoculation of SS113 (Strain 1; ES114 harboring an *Erm*<sup>R</sup> marker at VF\_A0239) and MJ11 (Strain 2; harboring the *Cam*<sup>R</sup> pVSV208 marker) or **(B)** SS113 gDNA was incubated with Strain 2. **C.** Transfer frequencies of selectable markers between Strain 1 and Strain 2 when a *recA*<sup>-</sup> mutation was introduced to either strain. **D.** Transfer frequencies of selectable markers between Strain 1 and Strain 2 when coinoculation were performed using either standard conditions, using a heat-killed Strain 1, on an agar surface, or on an agar surface with a 0.22  $\mu$ m filter separating Strain 1 and Strain 2. Transfer frequencies were calculated by dividing the Evolved CFU by the Total CFU. All experimental evolution assays were performed twice ( $n = 4$ ) and all data is shown; each color represents data from a separate experiment. Averaged transfer frequencies can be found in Table 3.1. Limit of detection is 200 evolved CFU/mL.

figure	strain 1	strain 2	assay conditions (if not std.)	avg. transfer freq	stdev transfer freq
2B	-	MJ11 pVSV208	std.	<i>nd</i>	<i>nd</i>
2B	SS101	-	std.	<i>nd</i>	<i>nd</i>
2B (not plotted)	SS112	-	std.	<i>nd</i>	<i>nd</i>
2B (not plotted)	SS113	-	std.	<i>nd</i>	<i>nd</i>
2B (not plotted)	SS104	-	std.	<i>nd</i>	<i>nd</i>
2B (not plotted)	DMA420	-	std.	<i>nd</i>	<i>nd</i>
2B	SS101	MJ11 pVSV208	std.	4.85E-09	3.59E-09
2B	SS112	MJ11 pVSV208	std.	1.96E-09	6.29E-10
2B	SS113	MJ11 pVSV208	std.	2.45E-09	1.54E-09
2B	SS104	MJ11 pVSV208	std.	5.51E-09	4.66E-09
2B	DMA420	MJ11 pVSV208	std.	2.74E-09	2.10E-09
3	SS113	-	std.	<i>nd</i>	<i>nd</i>
3 (not plotted)	-	MJ11 pVSV102	std.	<i>nd</i>	<i>nd</i>
3	-	KB8 pVSV102	std.	<i>nd</i>	<i>nd</i>
3	SS113	MJ11 pVSV102	std.	3.61E-07	1.23E-07
3	SS113	KB8 pVSV102	std.	1.94E-07	6.67E-07
4A	SS113	-	std.	<i>nd</i>	<i>nd</i>
4A	-	MJ11 pVSV208	std.	<i>nd</i>	<i>nd</i>
4A	SS113	MJ11 pVSV208	std.	6.82E-09	2.99E-09
4A	cell-free sup.	MJ11 pVSV208	std.	<i>nd</i>	<i>nd</i>
4B	SS113	-	std.	<i>nd</i>	<i>nd</i>
4B	-	MJ11 pVSV208	std.	<i>nd</i>	<i>nd</i>
4B	SS113	MJ11 pVSV208	std.	3.14E-08	1.82E-08
4B	SS113 gDNA	MJ11 pVSV208	std.	<i>nd</i>	<i>nd</i>
4C	SS113	-	std.	<i>nd</i>	<i>nd</i>
4C	-	MJ11 pVSV102	std.	<i>nd</i>	<i>nd</i>
4C	SS113	MJ11 pVSV102	std.	3.26E-08	2.03E-08
4C	SS113	MJ11 <i>recA</i> - pVSV102	std.	<i>nd</i>	<i>nd</i>
4C	SS113 <i>recA</i> -	MJ11 pVSV102	std.	2.28E-08	1.36E-08
4D (not plotted)	SS113	-	std.	<i>nd</i>	<i>nd</i>
4D (not plotted)	-	MJ11 pVSV208	std.	<i>nd</i>	<i>nd</i>
4D	SS113	MJ11 pVSV208	std.	1.52E-08	9.65E-09
4D	SS113 (hk)	MJ11 pVSV208	std.	<i>nd</i>	<i>nd</i>
4D	SS113	MJ11 pVSV208	agar	1.40E-08	6.88E-09
4D	SS113	MJ11 pVSV208	agar + filter	<i>nd</i>	<i>nd</i>

**Table 3.1. Transfer frequency summary across experiments.**

## CHAPTER 4 – Characterization of the *Lolliguncula brevis* microbiome across body sites

### 4.1 Introduction.

Symbiotic associations between bacteria and eukaryotes are found in nearly every environment, and cephalopods are often used as model systems for studying important interactions between host and symbiont. Much of this research has taken advantage of the well-characterized light organ association between the Hawaiian bobtail squid, *Euprymna scolopes*, and its bioluminescent symbiont, *Vibrio fischeri* [26, 27, 32]. This represents a highly specific symbiosis in which luminescence provided by *V. fischeri* in the light organ is thought to obscure the squid's silhouette to protect it from predators who hunt at night [150]. Recent work has characterized a more diverse set of microbes that colonize the accessory nidamental gland (ANG), a female reproductive organ found broadly in squid [161-164]. Bacteria associated with the ANG are secreted into the egg jelly coat and have been shown to protect the eggs from fungal and bacterial infections during embryonic development [165-167].

Although *E. scolopes* gill tissue has been found to exhibit changes in gene expression as a result of light organ colonization by *V. fischeri*, the squid gill microbiome itself has yet to be characterized [168]. While *Vibrios* have been found in association with both normal and ulcerated mantle tissue in *Lolliguncula brevis* squid [169], we know very little about what a healthy cephalopod microbiome might look like. One study used amplicon sequencing to characterize microbial community of *Sepia officinalis* and found a simple microbiome consisting of primarily *Vibrio* and *Piscirickettsiaceae* [170]. Given the success and reproducibility of studying symbiotic associations with squid light organs and ANGs, there remains a surprising gap in knowledge regarding squid microbiomes and how microbial community structure differs across body sites in cephalopods, or how these microbiomes might compare to the surrounding seawater.

In this study, we sought to take advantage of our proximity to coastal North Carolina and characterize the microbiome of the Atlantic brief squid, *Lolliguncula brevis*. *L. brevis* is found broadly from

the Gulf of Mexico to the Northeastern United States and is easily obtained in trawls [171-173]. Previous work has described reproducible methods for maintaining wild-caught *L. brevis* in the lab and breeding them to obtain juvenile animals [174]. *L. brevis* has been previously used to study swimming physiology and mechanics in cephalopods, and *L. brevis* specimens are often included in ecological studies of other cephalopods because of their broad distribution [171, 175]. Previous work on the ecology of *L. brevis*, along with the ability to maintain and rear wild-caught animals in the lab, makes this species a good candidate for future studies on host-symbiont interactions that could complement the work being done in *E. scolopes*. Bobtail squid (*E. scolopes*) and *Loliginid* squid (*L. brevis*) represent evolutionarily distinct groups of squid, and there is an opportunity to use these systems together to inform our understanding of conserved or diverging microbial functions to their hosts. Understanding the composition of bacteria associated with *L. brevis* will shed light on the basic ecology of squid microbiomes and will have important implications for future research design across cephalopod systems.

Here, we describe the morphology and microbiome of an undescribed body site in *L. brevis*, which we identify as the “sub-mantle tissue” (SMT). In addition, we use a combination of culture-based techniques and amplicon sequencing to characterize the microbiome of *L. brevis* mantle, gill, SMT, and ANG tissues. We find that while multiple species of *Vibrios* are cultured from *L. brevis*, they represent a relatively low percentage of the bacterial community in any given body site. Instead, the mantle, sub-mantle tissue, and ANG share a conserved microbiome that is dominated by a community of *Bradyrhizobium* spp. Further, the gill community of *L. brevis* seems to change as squid mature, and the gills of mature *L. brevis* host the core microbiome in addition to more diverse bacteria that are present in the surrounding seawater community. This work serves as a promising pilot study that establishes *L. brevis* as an exciting model for further exploration of host-symbiont interactions within cephalopod systems.

## 4.2 Results.

### ***L. brevis* collection and identification.**

To obtain the *L. brevis* specimens used in this study, otter trawls were performed regularly off the coast of Shackleford Banks, NC, USA between the summers of 2018 and 2022 (Fig 4.1A). Trawls were pulled for ~10 minutes and squid were immediately placed into 5-gallon buckets outfitted with bubblers. It was typical for some squid to be deceased upon completion of the trawl; any live squid were euthanized immediately using 5% EtOH in FSIO prior to measurement, dissection, and preservation.

Based on visual morphology, we predicted that the vast majority of animals we collected were Atlantic brief squid, *Lolliguncula brevis*, and each animal was given an “LB#” identification code. One specimen appeared morphologically distinct from the others, and we predicted that this may represent a different squid species. To confirm the genetic identity of this individual, as well as our predicted *L. brevis* specimens, we isolated genomic DNA from the eye tissue of four animals (3 predicted *L. brevis* and 1 unidentified squid) and PCR-amplified a 624-bp region of the cytochrome oxidase I (COI) gene using primers SNS07 and SNS08 [176]. Sanger sequencing of the resulting PCR-product was performed by Eton Bio, and the top BLAST hits for each sample can be found in Table 4.1. Consistent with our morphological identification, the COI sequences of LB13, LB14, and LB15 returned nearly identical matches to the COI gene sequence for *Lolliguncula brevis* in the NCBI database (Table 4.1). The fourth squid was identified as *Doryteuthis pleii* according to the same NCBI BLAST performed above and was thus given the identifier DP1 (Table 4.1). The phylogeny of these COI sequences is shown in Fig 4.1B, with the *Octopus bimaculoides* sequence used as an outgroup and the *Euprymna scolopes* and *Lolliguncula diomedea* sequences included for reference.

Previous work has shown the relationship between total weight and mantle length measurements to be a reliable indicator for *Loliginid* squid species identification [173, 174]. We obtained weight and mantle length measurements for all squid collected in this study and plotted their relationship (Fig 4.1C). Indeed, the R-squared value for all points excluding DP1 was 0.9277, with the *D. pleii* specimen representing a clear outlier. Taken together, these independent results suggest that the squid collected in this study are *L. brevis* with the exception of the single specimen, DP1 (*D. pleii*).



### ***L. brevis* dissection and body site selection**

To investigate bacterial associations with various *L. brevis* tissues, we began by dissecting out the gills and an approximately 25 mm<sup>2</sup> section of mantle tissue from each squid (Fig 4.2AB). In animals large enough to have formed sex organs, sex was determined by the presence of either sperm ducts or nidamental glands, and these animals were identified as “mature”. Animals with no visible sex organs were identified as “sub-adults”. Mature female squid often form an accessory nidamental gland (ANG), which houses a complex microbial community that is expelled onto eggs as they are laid and provides critical protection from fungus for developing embryos [161, 163, 165]. We observed these ANGs in mature female *L. brevis* and collected this tissue for subsequent amplicon sequencing (Fig 4.2CE). Given that many squid harbor symbiotic, bioluminescent *Vibrionaceae* within a light organ, we looked for the presence of light organs in *L. brevis* during routine dissection. Although one early description of *L. brevis* notes the lack of a light organ in this species, light organs are found in other closely-related *Loliginid* squids [177-179]. Interestingly, we observed a tissue structure in all *L. brevis* animals, including males, females, and sub-adults, that did not appear to be labeled in any morphological diagrams of *L. brevis*. This tissue is dense, loosely-connected within the mantle cavity, and does not appear to be physically associated with either the digestive or reproductive systems. Reminiscent of the *E. Scolopes* light organ, this tissue is found just ventral to the ink sac in both *L. brevis* and *D. pleii* and has a distinct kidney-bean shape (Fig 4.2CD). We collected this tissue for further characterization and refer to this sample type as sub-mantle tissue (SMT) throughout the manuscript. In total, we obtained tissue samples from the mantle (M), gill (G), accessory nidamental gland (ANG), and/or sub-mantle tissue (SMT) of 28 animals for subsequent work. A breakdown of tissue samples and their subsequent analysis can be found in Table 4.2.

### **Multiple *Vibrio* species are cultured from *L. brevis* gill and sub-mantle tissue**

Given our hypothesis that the sub-mantle tissue may represent a light organ-like structure, we reasoned that there may be a population of culturable *Vibrio* bacteria associated with this tissue, as is characteristic of other light organs [180-182]. We chose the gills as an additional body site for comparison of culturable microbes, expecting that constant filtration of seawater through the gills may result in a more diverse suite of culturable bacteria. Following the initial dissection, tissue samples from the gill or sub -

mantle tissue were rinsed 3x in filter-sterilized Instant Ocean (FSIO) prior to homogenization. Tissue was allowed to settle for 5 min, and serial dilutions were plated onto agar plates made with LBS media and incubated at 24°C overnight.

We were surprised to find that the majority of resulting bacterial colonies were brightly bioluminescent, whether they were isolated from the gill or the sub-mantle tissue. Approximately 300 of these isolates, both bright and dim, have been stocked down for future investigations. Previously, we sequenced the genomes of two of these isolates and identified them as *V. fischeri* (LB10\_SMT6) and *V. campbellii* (LB10\_SMT1) [14, 183].

The bright luminescence we observed in many of these isolates, along with the previously sequenced genomes of LB10\_SMT1 and LB10\_SMT6, supported our prediction that *Vibrios* may make up a significant proportion of *L. brevis*' culturable microbiome. While 16S *rRNA* sequences are often used to identify bacterial species, work in vibrios has shown that the *hsp60* sequence is a better target for identifying vibrios at the species level [184-187]. We selected 37 representative isolates: 22 from the sub-mantle tissue and 15 from the gills, including 6 isolates from our *D. pleii* specimen. Genomic DNA was extracted from each isolate, and a 554 bp region of the *hsp60* gene was PCR-amplified using primers H279 and H280 [188]. The resulting PCR products were sequenced by Eton Bio for subsequent analysis. Phylogeny of these representative isolates suggest that indeed, all of the isolates we sequenced cluster within a broad vibrio clade (Fig 4.3A). As expected, LB10\_SMT6 clustered most closely with *Vibrio fischeri*, and LB10\_SMT1 clustered most closely with *Vibrio campbellii*.

We also performed a BLAST search for all newly obtained *hsp60* sequences; the top hit from each of these searches can be found in Table 4.3. Interestingly, we observe a clade of *Vibrio* isolates that most closely cluster with the *Vibrio jasicida* reference sequence (Fig 4.3A, green font). We used FastANI to calculate the percent identity of strains across this clade, including the *V. jasicida* reference, and found that while one subset of this clade does share >98% identity with *V. jasicida* (DP1\_SMT1, DP1\_G2, LB10\_G1, LB14\_SMT7, LB10\_G3, and LB10\_G2), the remaining isolates in this clade shared only between 74 – 92% *hsp60* identity with *V. jasicida* – well below the accepted standards for species-level identification (Fig 4.3B). This analysis suggests that there exists a clade of culturable *Vibrio* sp. that are associated with *L. brevis* and *D. pleii* that related to but distinct from *Vibrio jasicida*.

There was no obvious phylogenetic grouping among isolates obtained from *L. brevis* compared to *D. pleii*, nor from isolates obtained from the gill compared to the sub-mantle tissue. Additionally, we did not isolate any bacteria from outside of the *Vibrionaceae* family. Taken together, these results suggest that there appears to be a relatively conserved group of culturable vibrios associated with both the gill and sub-mantle tissue of *L. brevis*, and this community may be similar in other *Loliginid* squid like *D. pleii*. While it is important to note that there are almost certainly other bacteria that are also associated with these tissues, our isolations were performed using LBS media that likely enriched vibrio growth and could explain why only vibrios were cultured under these conditions.

### **Sub-mantle tissue isolates are unable to colonize *E. scolopes***

Next, we asked whether the representative isolates LB10\_SMT1 (*V. campbellii*), or LB10\_SMT6 (*V. fischeri*) could colonize the light organs of juvenile *E. scolopes* during traditional host colonization assays. Freshly hatched juvenile *E. scolopes* were exposed to either no bacteria (apo), the native *E. scolopes* symbiont *V. fischeri* ES114, *L. brevis* symbionts LB10\_SMT6 or LB10\_SMT1, or KNH3 – a *V. campbellii* strain isolated from Kaneohe Bay, HI. Only the native *E. scolopes* symbiont ES114 was recovered at CFU per squid significantly higher than the apo treatment, indicating that neither the *L. brevis* isolates nor KNH3 were able to colonize *E. scolopes* squid (Fig 4.4). The results of this colonization assay suggest that different genetic factors are required to colonize *E. scolopes* light organs or *L. brevis* sub-mantle tissue.

### **Sub-mantle tissue does not have characteristics typical of light organs**

Given the initial resemblance of the sub-mantle tissue (SMT) to the *E. scolopes* light organ in regard to macroscopic morphology and apparent vibrio association, we sought to investigate further whether this tissue might be functioning as a light organ. The adult *E. scolopes* light organ is bilobed with typically one pore on either side of the organ that leads into a crypt space that houses bioluminescent symbionts [189]. Importantly, the morphology of the *E. scolopes* changes dramatically as the animal develops, and these developmental changes have not been well-described in other light organ systems [189-191]. Therefore, it is hard to predict how a light organ might look or function differently in a distantly-related squid such as *L. brevis*.

Moreover, *E. scolopes* has been shown to use light emitted by its *V. fischeri* light organ symbionts as counterillumination against predators [150]. Counterillumination requires a measurable amount of light to be emitted from the light organ in order to camouflage the animal's silhouette by matching downwelling moonlight [150, 192]. We hypothesized that if the sub-mantle tissue functioned as a light organ in *L. brevis*, we would expect to observe physical characteristics such as (1) the presence of pores on the surface of the sub-mantle tissue structure, (2) bacteria associated with crypt spaces, or (3) higher luminescence in the sub-mantle tissue compared to other tissue sites.

Sub-mantle tissues from freshly-caught *L. brevis* were dissected and immediately preserved in 4% PFA in mPBS prior to embedding in paraffin and sectioning for microscopy. Sub-mantle tissue was collected from five animals, and 5  $\mu$ m parallel sections were divided for imaging with either DIC or for fluorescence *in situ* hybridization. We imaged the entire sub-mantle tissue section using DIC and did not observe any obvious signs of pores on the surface of the SMT, and although we observe striations within the SMT (Fig 4.5A), it is unclear whether these could be a form of crypt or cavity as we observe in *E. scolopes* light organs. To identify whether bacteria are associated with the SMT, either within potential crypts or elsewhere, we used fluorescence *in situ* hybridization. Parallel sections of the same samples described above were stained with either a *dapB* Cy5-conjugated negative control probe, or an EB-16S-rRNA Cy5-conjugated probe and imaged using fluorescence microscopy. We chose the EB-16S-rRNA probe because it should identify any bacterial signal present within the tissue (Advanced Cell Diagnostics, Newark, CA). These slides were also stained with DAPI to visualize squid nuclei, and autofluorescence from the squid tissue was captured using a filter with an excitation wavelength of 467 – 498 nm and an emission wavelength of 513 – 556 nm. No Cy5 signal was detected from sections that were exposed to the *dapB* probe, as expected in our negative control (Fig 4.5B). In sections exposed to the EB-16S-rRNA probe, we observed a strong fluorescence signal dispersed throughout the SMT that was consistent in size with both single bacterial cells and potentially cell aggregates (Fig 4.5CD). Interestingly, the bacterial signal appeared to be evenly dispersed throughout the tissue rather than associating specifically within cavity spaces or on the surface of the SMT, suggesting that bacteria in the *L. brevis* SMT are not localized to individual crypts as they would be in the *E. scolopes* light organ.

To determine whether the SMT produces higher relative luminescence than other surrounding tissue types, we dissected out the SMT, gill, and mantle tissue from 17 freshly caught *L. brevis* squid and immediately measured the luminescence of each tissue type using a Promega GloMax 20/20 luminometer (Fig 4.5E). Between taking measurements for each animal, we also measured the luminescence of “blank” tubes containing 1 mL of seawater collected from the trawl site. There was no statistical difference between the luminescence of the blank treatment and either the SMT, gill, or mantle tissue samples according to a Dunnett’s multiple comparison test. To provide context to these relative luminescence values, we also used the same luminometer to perform luminescence curves of representative isolates that were grown in culture. *V. fischeri* strains ES114 and MJ11 were isolated from the light organs of *Euprymna scolopes* squid and *Monocentris japonica* fish, respectively, and are known to be bioluminescent in culture [193-195]. The ES114  $\Delta luxC-G$  strain represents a dark mutant that is missing essential genes for bioluminescence [195]. LB10\_SMT1 and LB10\_SMT6 were chosen as representative *L. brevis* sub-mantle tissue isolates; while LB10\_SMT1 is brightly luminescent in culture, LB10\_SMT6 is not visibly luminescent [14, 183]. Peak luminescence values for each strain indicate that indeed, LB10\_SMT1 produces more luminescence than even ES114 or MJ11, and LB10\_SMT6 was not statistically different from the ES114  $\Delta luxC-G$  dark mutant (Fig 4.5E) according to a one-way ANOVA followed by a Tukey multiple comparisons test. In combination with our luminescence measurements of fresh *L. brevis* tissue, these results suggest that, while at least some *L. brevis* isolates have the potential to produce bright luminescence in culture, they do not appear to luminesce in the host under these conditions. This is in contrast to the *E. scolopes* light organ, which emits measurable light produced by its bacterial symbionts.

Taken together, we found no indication that the *L. brevis* sub-mantle tissue is functioning as a light organ, at least in the traditional sense. We did not observe pores on the surface of the tissue structure, and while there are striations within the tissue that may form cavities or crypts, they are not densely filled with bacteria as we would expect from a colonized light organ. Additionally, the relative luminescence of sub-mantle tissue is similar to surrounding tissue and seawater, despite housing isolates with the potential to luminesce in culture. Nevertheless, we consistently isolate bioluminescent vibrios

from the sub-mantle tissue and gills of *L. brevis*, and fluorescence *in situ* hybridization indicates a strong bacterial association within the SMT that warrants further investigation.

## **Amplicon Sequencing**

### **Body site selection and sample collection.**

To gain a more robust understanding of the complete microbial community across *L. brevis* body sites, we turned to amplicon sequencing. Given the strong association between vibrios and other squid hosts, along with our cultured isolates from *L. brevis*, we anticipated many vibrio taxa would be present in *L. brevis* samples. Although the 16S rRNA gene is a common amplicon target region for broad bacterial communities, the *hsp60* gene provides more reliable identification of vibrio taxa at the species level and has been used previously for vibrio-specific community analysis [184, 185, 188].

We collected six *L. brevis* squid for amplicon sequencing - three that were identified as mature females, and three sub-adults. Mantle, gill, and sub-mantle tissue samples were taken from all animals, and ANG samples were also collected from mature females. All samples were frozen in liquid N<sub>2</sub> in the field immediately following dissection, where they remained until gDNA extractions were performed upon returning to the lab. Seawater was also collected in duplicate from either Bogue Sound (inshore) or the trawl site (offshore) (Fig 4.1A). Each 500 mL seawater sample was passed through a 0.22 µm filter, and gDNA extractions were performed on the biomass captured by the filter. Additionally, we included a “blank” kit control sample with no DNA added prior to extraction. Genomic DNA from each sample was used for *hsp60*-targeted amplicon sequencing; see Fig 4.6 for a complete sample breakdown and primer sequences used for amplicon sequencing. DNA extractions were performed using a Zymo Bacterial/Fungal DNA Miniprep Kit (Zymo Research, Irvine, CA). Library prep and 300 bp paired-end sequencing was performed by UNC’s High-Throughput Sequencing Facility (UNC-HTSF) on a MiSeq platform.

### **Bacterial community bioinformatics pipeline.**

The bioinformatics pipeline combined the Quantitative Insights into Microbial Ecology (QIIME2 2, Version 2022.2) and DADA2 (Version 1.24.0) packages [196-198]. Reads were trimmed, filtered, denoised, and chimeric reads were removed from each sample using DADA2. A complete .Rmd file with all parameters and computational methods can be found at

[https://drive.google.com/file/d/1sAfid\\_ohQAS0B30W6ApO1wLxyR2kbEXf/view?usp=sharing](https://drive.google.com/file/d/1sAfid_ohQAS0B30W6ApO1wLxyR2kbEXf/view?usp=sharing) . Figure 4.6 includes a summary workflow for bioinformatic analysis, and Table 4.4 shows the number of reads retained per sample at each DADA2 step for *hsp60* samples.

For *hsp60* amplicon samples, the larger 554 bp target amplicon size meant that forward and reverse reads did not merge post-trimming; thus, only the forward reads are examined for *hsp60* samples in this analysis and were trimmed to a length of 254 bp. Our analysis produced 5,795,169 raw reads, from which we identified 13,636 total ASVs. Although the *hsp60* gene has been used as an amplicon target previously, taxonomic reference databases for *hsp60* were not readily available with published works. Following the workflow described in Dubois et al. 2022, I created a new *hsp60* reference database using 26,217 reference FASTA sequences that were obtained from cpnDB.ca on 1/11/2023 [199-201]. In addition to the FASTA sequences obtained from cpnDB.ca, the reference database created for this study also included the newly obtained *hsp60* sequences of cultured *L. brevis* isolates that were included in Fig 4.3. Taxonomy of *hsp60* samples was assigned using the hybrid VSEARCH-sklearn function in QIIME2, with unique ASVs as the query input, reference reads and taxonomy from the *hsp60* reference database described above, and a confidence cutoff parameter of 0.7, as recommended by Bokulich et al. 2018 [202]. The output of this QIIME2 taxonomic assignment was then imported into R (Version 4.1.2) as a Phyloseq (Version 1.38.0) object for downstream analysis [203].

### **Community composition based on *hsp60* amplicon sequences.**

In analyzing our amplicon sequencing data, we first sought to visualize the broad community composition of all samples according to their *hsp60* sequence. Specific taxa were renamed in broad categories for the stacked bar plot in Figure 4.7. Taxa designated as “Unassigned at Kingdom Level” indicates taxa that did not receive any taxonomic identification, even at the kingdom level. “Unidentified Bacteria” indicates taxa that were assigned as “k\_\_Bacteria” at the kingdom level but received no further taxonomic designation. All other taxa are indicated at the family level, and log<sub>10</sub>-transformed relative abundance is indicated on the x-axis, and individual samples are labeled by treatment on the y-axis.

Because we had previously cultured vibrios from *L. brevis* specimens across multiple body sites, we were surprised to see that *Vibrionaceae* represents a conserved but minority taxa across all samples, including samples from the water column (Fig 4.7). We were also surprised that the “Unidentified

Bacteria” group made up such a large proportion of the microbial community. Most studies that use *hsp60* amplicon targets have been focused on the vibrio community; therefore, vibrios are very well represented in *hsp60* reference sequences, and reference sequences for more diverse taxa are limited.

Perhaps most interesting at the community level is the strong presence of *Nitrobacteraceae* across all *L. brevis* samples. We initially speculated that the presence of *Nitrobacteraceae* could be a result of contamination from our DNA extraction kits; however, *Nitrobacteraceae* is absent in our kitcon sample and makes up < 0.1 % of the relative seawater community compared to ~ 1 – 45% of the relative *L. brevis* community across individual samples.

#### ***hsp60* rarefaction and alpha diversity measures.**

Rarefaction analysis is typically used to estimate the richness within and between sequenced samples and gives an indication of whether sequencing depth was sufficient to capture the diversity of taxa within a sample [204, 205]. A curve on a rarefaction plot indicates that sufficient samples depth reached saturation, and it is unlikely that new taxa would be identified by increasing the sample depth; in contrast, an ascending graph implies that the sample has an insufficient sampling depth to infer true taxa diversity. A rarefaction plot for the *hsp60* amplicon samples in this study indicates that a sufficient sampling depth was reached for all samples (Fig 4.8A). While we include a rarefaction plot for visualization, recent works argue that rarefaction is not justifiable and we do not use rarified datasets for subsequent analysis [206].

Next, we plotted the Chao1 and Shannon alpha diversity measures for all *hsp60* amplicon samples (Fig 4.8B). The Chao1 index is a qualitative measure of species richness that estimates the number of species in a sample, while the Shannon index measures both the richness and evenness within a sample. Generally, we observe higher diversity and evenness in SMT and mantle samples compared to other samples, although we did not perform statistics across alpha-diversity measures as some treatments contain only one or two samples.

#### ***L. brevis* samples are distinct from seawater and kitcon samples at the community-level.**

The dendrogram in Fig 4.9A depicts the variance-stabilized Euclidean distance calculated between all *hsp60* amplicon samples. Individual samples are labeled by treatment and color-coded by



body site. Most samples clustered together by treatment; we observe a distinct grouping of the mature gill and ANG communities that were most similar to the seawater community.

To more clearly quantify and visualize this separation, we performed a PCoA analysis using the Bray-Curtis distance metric across body sites (Fig 4.9B). Individual points represent samples that are color-coded by treatment, and ellipses are drawn around sub-adult, mature, and seawater groupings. Again, we observe a very clear separation between *L. brevis*, seawater, and kitcon samples, with the mature ANG and gill samples clustering more closely with the seawater community compared to other *L. brevis* body sites. While the distinct grouping of mature ANG and gill samples stands out visually in the PCoA plot, it is also very interesting that the mantle and sub-mantle tissue samples are so similar. This similarity indicates that there may be a conserved core microbiome that is shared between these (and other) body sites.

#### ***L. brevis* hosts a distinct, conserved microbial community.**

While the distance metrics described above identified a distinct separation between the *L. brevis* and surrounding seawater community, we sought to better understand the taxa driving this separation. We used a PCA plot to visualize individual samples that were color-coded by treatment and added ellipses based on squid maturity or seawater variables. Further, we included the top 10 family-level taxa as vectors according to their principle component association (Fig 4.10). This plot suggests that taxa including *Nitrobacteraceae*, *Roseobacteraceae*, and *Endozoicomonadaceae*, among others, are enriched in *L. brevis* samples compared to the seawater samples, which were dominated by *Synechococcaceae*, *Pelagibacteraceae*, and *Streptomyetaceae*.

#### **Core microbiome of *L. brevis* is dominated by *Nitrobacteraceae*, *Vibrionaceae*, and unidentified bacteria.**

To understand the taxa driving similarities between the remaining *L. brevis* samples, we sought to characterize the core microbiome that is conserved across *L. brevis* body sites. Taxa were filtered and identified as belonging to the core microbiome by representing > 5% of total reads across > 80% of all *L. brevis* samples. This analysis identified 507 conserved ASVs that passed our filtering criteria. The relative abundance of this core community was plotted at the family level using a stacked bar plot (Fig 4.11). This plot indicates that *Nitrobacteraceae* (*Bradyrhizobium* spp.) and unidentified bacteria make up the majority

of core taxa, along with a low abundance but still conserved group of *Vibrionaceae* (*Aliivibrio* spp.). It is important to note that any assigned bacteria here are indeed conserved taxa but may or may not actually represent a single genus.

For a higher resolution view of the microbiome sampled here, we identified the top 100 families across all samples by abundance and plotted the relative abundance of each taxa on a heat map (Fig 4.12A). Columns are labeled across the bottom of the plot by sample ID (kitcon = kit control; LB# = *L. brevis* samples; IW/OW = seawater samples), and the dendrogram across the top of the plot represents the Euclidean distance between samples. According to this plot, it is clear that *Nitrobacteraceae* and taxa that were unidentified at the kingdom level were heavily enriched in *L. brevis* samples compared to the kitcon or seawater treatments. While *Vibrionaceae* and unidentified bacteria were also identified in the core *L. brevis* microbiome, it is harder to interpret their association with *L. brevis* because these taxa make up a similar relative abundance in the seawater samples.

We also identified the top 100 unique ASVs across all samples by abundance and plotted the relative abundance of each taxa on a heat map (Fig 4.12B). The plot is labeled as described above, except that rows indicate unique ASVs rather than families. This plot identifies ~30 unique ASVs that are heavily enriched in *L. brevis* samples compared to the kitcon or seawater treatments and were taxonomically identified as primarily *Bradyrhizobium* spp. (*Nitrobacteraceae* family) or uncultured bacteria (Unidentified Bacteria). Taken together, these data provide ample evidence that *Bradyrhizobium* spp. and several specific, unidentified bacterial ASVs make up a core microbiome in *L. brevis* that is highly-conserved across the SMT, mantle, gill, and ANG body sites.

### 4.3 Discussion.

The Atlantic brief squid, *Loliguncula brevis*, represents an easily obtained *Loliginid* squid that is found broadly from the Gulf of Mexico to the coastal Northeastern United States [171-173]. While not typically sold commercially, *L. brevis* has been used as a model system for understanding cephalopod swimming mechanics and its ecology is relatively well-studied compared to other cephalopods [173, 207-209]. Previous work has described methods for maintaining *L. brevis* in aquaculture, including methods for breeding wild-caught adults to obtain juvenile animals [174, 210]. This broad ecological knowledge of *L. brevis* makes it an excellent candidate for future research, and this study sought to exploit our proximity to the North Carolina coast to expand our limited knowledge of *Loliginid* squid microbiomes. Here, we used a combination of culture-based assays, ultrastructure and fluorescence microscopy, and amplicon sequencing to characterize the microbiome of *L. brevis* mantle, gill, sub-mantle tissue, and ANG body sites. Further, we provide a physical description of an undescribed tissue site in *L. brevis*, which we identify as the “sub-mantle tissue” (SMT).

During routine dissections of *L. brevis*, we observed a distinct tissue site within the mantle cavity that we were unable to find mention of in the literature. This tissue was present in the same location in all animals we collected regardless of sex or maturity and was physically reminiscent of the well-studied light organ in *Euprymna scolopes*. However, freshly dissected SMT did not luminesce any more than the surrounding mantle tissue, gill tissue, or seawater. Further, we did not observe any pores or crypts associated with the SMT by ultrastructure microscopy, suggesting that the SMT is unlikely a functioning light organ, at least as we know it. It is also possible that the SMT represents a vestigial light organ, and future work should focus on identifying a function for the SMT and its associated bacteria. While the general function of the SMT remains unknown, fluorescence *in situ* hybridization was used to observe bacteria that were physically associated with the SMT. We cultured multiple species of bioluminescent vibrios that were associated with both the SMT and gill tissue of *L. brevis*. This included a clade of vibrios that were most closely related to *Vibrio jasicida* but seem to represent a group of host-associated vibrios that have not yet been described at the species level.

The genomes of two SMT isolates collected for this study have been sequenced, and the strains were identified as *Vibrio fischeri* (LB10\_SMT6), and *Vibrio campbellii* (LB10\_SMT1) [14, 183]. These

strains, along with a *Vibrio campbellii* strain that was isolated from Kaneohe Bay, HI (KNH6) were unable to colonize juvenile *E. scolopes* during a host-colonization assay. This suggests that different genetic factors are required for colonizing *E. scolopes* and *L. brevis*, providing further evidence that *L. brevis* could be exploited as a model system to complement work being done in *E. scolopes*.

The results of our juvenile *E. scolopes* colonization assay (Fig 4.4) suggest that *L. brevis* and its microbial symbionts could be used in combination with the *E. scolopes* light organ symbiosis to better understand the evolution of host-symbiont partnerships. I predict that the experimental evolution assay described in chapter 3 of this dissertation could be used to coincubate native *E. scolopes* symbionts with *L. brevis* isolates that are unable to naturally colonize *E. scolopes* squid, such as LB10\_SMT6 or LB10\_SMT1. Using a counterselection against the native squid symbiont, the mixed culture would be used as inoculum during juvenile *E. scolopes* colonization assays as described above. If essential host-colonization factors are exchanged during this coincubation period, then presumably only evolved *L. brevis* isolates that acquired genetic factors required for *E. scolopes* colonization would be recovered from colonized animals. Those evolved genotypes could then be isolated and their genomic sequences compared to each parent strain to understand genes that are enriched or depleted in evolved strains that gained the ability to colonize a new host.

Because we had previously isolated only *Vibrio* sp. from *L. brevis*, and *Vibrio* sp. are often studied in association with squid and other hosts, we expected *Vibrio* sp. to make up the majority of the *L. brevis* microbiome. However, amplicon sequencing using an ~554 bp *hsp60* target (primer pairs H279/H280 and H1612/H1613 [188]) revealed that while vibrios are indeed present and conserved across *L. brevis* samples, they are a minority taxa within the community. Instead, the *L. brevis* core microbiome is dominated by *Bradyrhizobium* and unknown bacteria that are found in high abundance across all body sites. *Bradyrhizobium* represents a genus of Gram-negative nitrogen-fixers that are most commonly identified in soil and are known for forming symbiotic relationships with legumes where they fix nitrogen in exchanges for carbohydrates from the plant [211-213]. Although *Bradyrhizobium* is known to be host (plant)-associated and is represented in marine systems, to our knowledge this is the first direct association between *Bradyrhizobium* and a marine invertebrate. Given that cephalopods continuously excrete nitrogen waste is it tempting to speculate that this could provide a critical source of nitrogen that

would drive the association between *L. brevis* and *Bradyrhizobium*. Future studies should attempt to isolate *Bradyrhizobium* from *L. brevis* and include research questions that address this relationship to better understand the association between *Bradyrhizobium* and *L. brevis* that we describe here.

In addition to the core microbiome, the gills of mature *L. brevis* also host more diverse taxa that most closely resemble the surrounding seawater community. Gills constantly filter seawater as the animal breathes and diverse taxa have the opportunity to become associated with the gill tissue, making it unsurprising that the gills host a more diverse microbial community compared to other body sites. Interestingly, we observe a distinct shift in the microbial community of sub-adult vs. mature *L. brevis* gills, which suggests that this community may change over time. Future research should seek to understand this community shift and how microbial partners may be displaced or acquired over time.

This study was somewhat limited by our use of the *hsp60* amplicon target, and we propose that future work should build on this pilot study to gain a more robust understanding of squid microbial communities. While the *hsp60* gene makes an excellent amplicon target for identifying vibrios at the species level, *hsp60* reference sequences for more diverse taxa remain very limited. This explains why so many of our ASVs were only identified taxonomically at the kingdom level. This study identified a conserved microbiome in *L. brevis*, but we were unsuccessful in culturing these unknown bacteria. Phylogeny of ASV sequences designated as unknown bacteria in the *L. brevis* core microbiome suggest that they may be most closely related to *Bradyrhizobium*, but it would be worth resequencing these samples using a 16S amplicon target or revisiting this data as more *hsp60* reference sequences become available. Using multiple 16S amplicon targets in combination could also potentially allow for more successful species-level taxonomic identification. Future amplicon studies should take the availability of reference sequences into consideration during study design, and keep in mind how research questions might change with a limited reference database.

#### **4.4 Materials and Methods.**

##### **Animal collection.**

At the time of this study, cephalopod work does not require any specific IACUC statements or permits for animal collection. However, we made every effort to make sure that animals were collected

responsibly and treated with care. All animals were collected by otter trawl ~3 miles offshore from Shackelford Banks, NC. Live squid were anesthetized using 5% EtOH in FSIO prior to dissection.

#### **Bacterial isolation from squid.**

Immediately following dissection of fresh *L. brevis* specimens, tissue samples were rinsed 3x in FSIO. Tissue was homogenized using a sterile pestle in a 1.5 mL tube, and tissue was left undisturbed for ~5 min to settle prior to plating. Serial dilutions were then spread plated onto LBS agar plates using sterile glass beads and incubated overnight at 24 °C. Individual colonies were restreaked at least 2x to ensure clonal isolation before stocking down for subsequent use. Bacteria were isolated from at least 20 *L. brevis* individuals and 1 *D. pleii* individual and include isolates from the mantle, gill, and sub-mantle tissue (SMT).

#### **Isolate identification based on *hsp60* sequence.**

Genomic DNA was extracted from 37 squid isolates and ~554 bp of the *hsp60* sequence was PCR-amplified using primers H279 and H280. The resulting PCR product was then sequenced by Eton Biosciences. Sequences were aligned by Clustal and subsequently trimmed, and the resulting trimmed alignment was used to create a phylogenetic tree.

#### **Luminescence curves of *L. brevis* isolates.**

To measure peak luminescence in culture, isolates were streaked out onto LBS agar plates and incubated at 24 °C overnight. Three individual colonies of each strain were subsequently used to inoculate liquid LBS cultures for biological replication and again incubated at 24 °C overnight, with shaking. The following day, cultures were diluted 1:1000 into ASWT and relative luminescence units (RLU) and corresponding optical density (OD<sub>600</sub>) were measured at 30 min time intervals over the course of 6 hours. Peak luminescence was calculated by dividing the RLU/OD<sub>600</sub>.

#### **Luminescence measurements of *L. brevis* tissue.**

Immediately following dissection of freshly caught *L. brevis*, tissue samples were placed in a 1.5 mL tube with ~1 mL fresh seawater and relative luminescence was measured. Blank samples consisted of 1 mL fresh seawater obtained from the trawl site with no tissue added. These measurements were performed in the field within 30 minutes of animal collection.

### **Microscopy of *L. brevis* sub-mantle tissue.**

Immediately following dissection, the SMT of 6 individual *L. brevis* squid were preserved in 4% PFA in mPBS and stored on ice until returning to the lab. Preserved tissue was then embedded in paraffin and 5  $\mu$ m parallel sections were obtained from each sample to be used for either ultrastructure or fluorescence microscopy.

*Ultrastructure microscopy.* DIC images were obtained on an inverted Nikon Ti-2 microscope outfitted with a Hamamatsu ORCA Fusion sCMOS camera. To capture the entire SMT section, 17x10 fields of view were imaged and stitched together with 15% overlap to produce the final images in this manuscript.

*Fluorescence microscopy.* Sections were prepared for fluorescence *in situ* hybridization with either a *dapB* Cy5-conjugated probe as a negative control, DAPI to stain the host (squid) nuclei, or an EB-16S-*rRNA* Cy5-conjugated probe. Each section was imaged on an inverted Nikon Ti-2 microscope outfitted with a Hamamatsu ORCA Fusion sCMOS camera. Brightness and contrast adjustments were made uniformly across all images in FIJI [63].

#### 4.5 Figures.

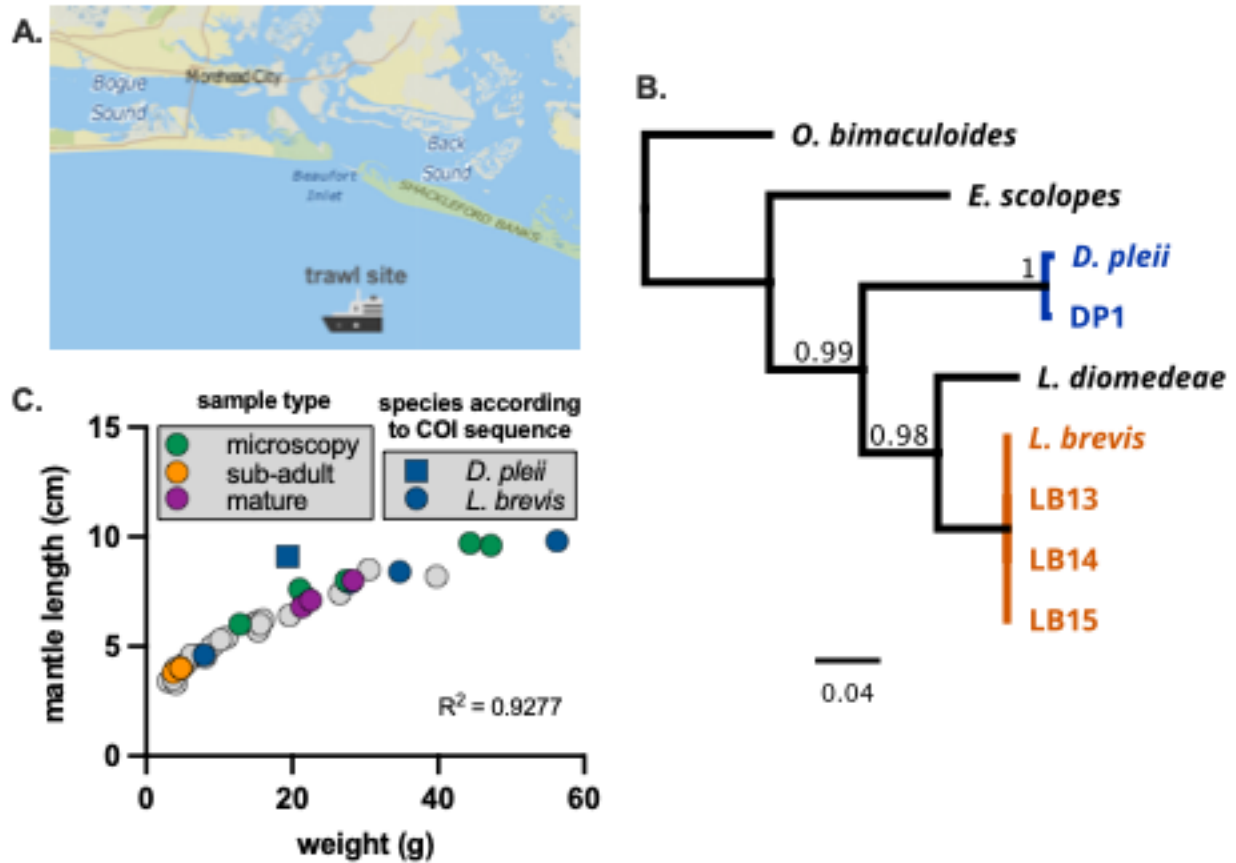


**Figure 4.1. *L. brevis* collection and identification.** **A.** Map of trawl site where squid were collected off the coast of Shackleford Banks, NC, USA. **B.** Phylogeny of representative squid obtained for this study, constructed using COI gene sequence and FastTree. **C.** Weight (g) vs. mantle length (cm) plot of squid obtained for this study. Each data point represents measurements taken from an individual animal ( $n = 38$ ). Shape indicates the squid species; COI gene was sequenced from individuals colored blue (square = *Doryteuthis pleii*; circle = *Loliguncula brevis*). Color indicates the subsequent method performed on each sample (green = microscopy; sub-adult = amplicon; mature = amplicon; gray = weight/length measurement only). A simple linear regression of weight vs. mantle length of *L. brevis* resulted in an  $R^2$ -value of 0.9277.



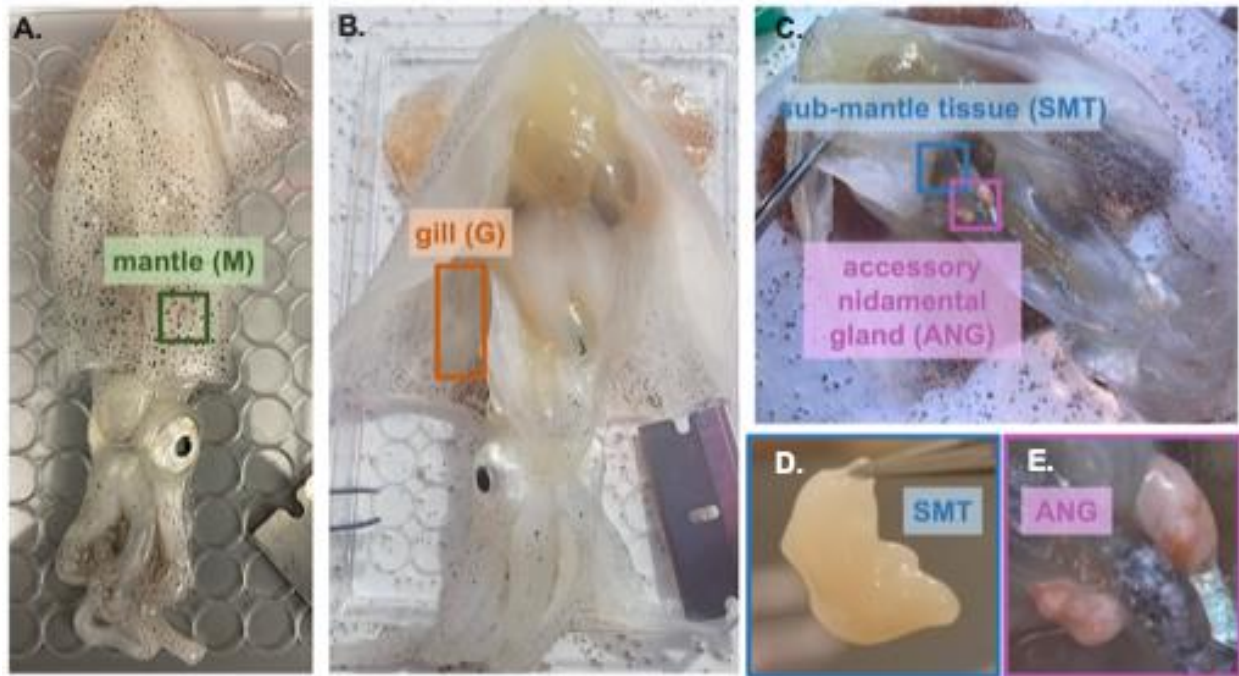


**Figure 4.2. *L. brevis* dissection and body site selection.** **A.** Undissected *L. brevis* with mantle sampling location indicated by green box. **B.** Mature, female *L. brevis* specimen that has been dissected to show the gill sampling location, indicated by orange box. **C.** Mature, female *L. brevis* specimen with the nidamental gland removed to indicate the sampling locations for the **D.** sub-mantle tissue (blue box), and **E.** accessory nidamental gland (pink box). All specimens were anaesthetized in 5% EtOH in FSIO prior to dissection and imaging.

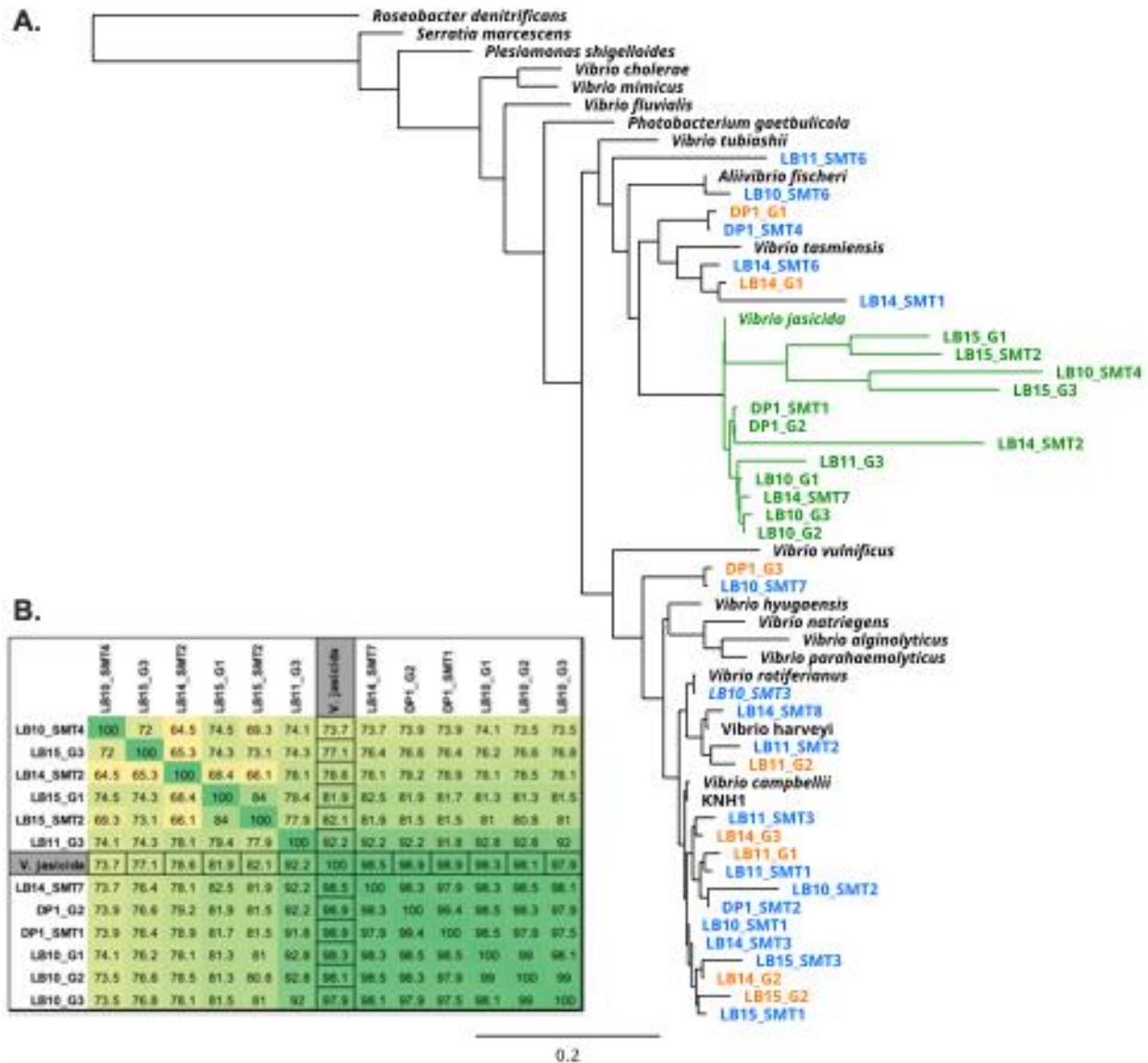


**Figure 4.3. Phylogeny of *Vibrionaceae* species cultured from *L. brevis* gill and sub-mantle tissue.**  
**A.** Phylogenetic tree constructure using the *hsp60* gene sequence of 37 isolates that were cultured from either the gill (orange) or sub-mantle tissue (blue) of four *L. brevis* (LB) and one *D. pleii* (DP) specimens. Twenty additional *hsp60* gene sequences were obtained from NCBI and included on the phylogenetic tree for reference (black). *V. jasicida* clade isolates are colored green. All *hsp60* sequences were aligned using Clustal, trimmed, and the resulting phylogeny was calculated using FastTree and visualized in Geneious. The top BLAST result for each isolate included on this tree, along with the accession numbers for all reference sequences, can be found in Table 4.3. **B.** Pairwise FastANI comparison between the *hsp60* gene sequences of all members of the *V. jasicida* clade identified in (A).

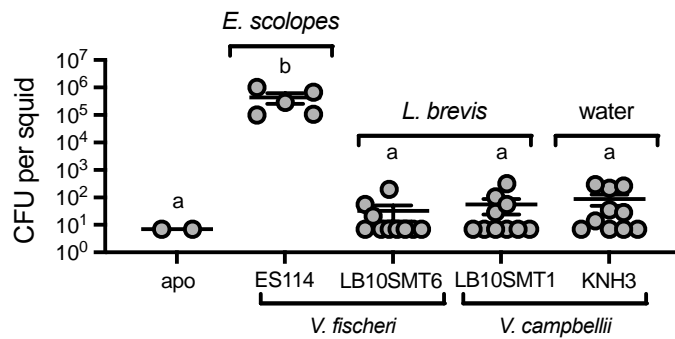


**Figure 4.4. Vibrios isolated from *L. brevis* sub-mantle tissue are unable to colonize juvenile *E. scolopes*.** Results of juvenile *E. scolopes* colonization assays with strains *V. fischeri* ES114, *V. fischeri* LB10SMT6, *V. campbellii* LB10SMT1, and *V. campbellii* KNH3 as inoculum. Each data point represents the CFUs per squid calculated for an individual squid from CFUs collected at 24 h after initial exposure to inoculum. The isolation source of each inoculum strain is indicated directly above the treatment. Letters indicate significantly different CFUs per squid between treatments (one-way ANOVA with Tukey's multiple-comparison posttest:  $P < 0.01$ ). Experiment was performed twice; representative data shown here ( $n = 37$ ). Data for this section was collected and analyzed in collaboration with Katie Bultman in Mark Mandel's lab at University of WI – Madison.

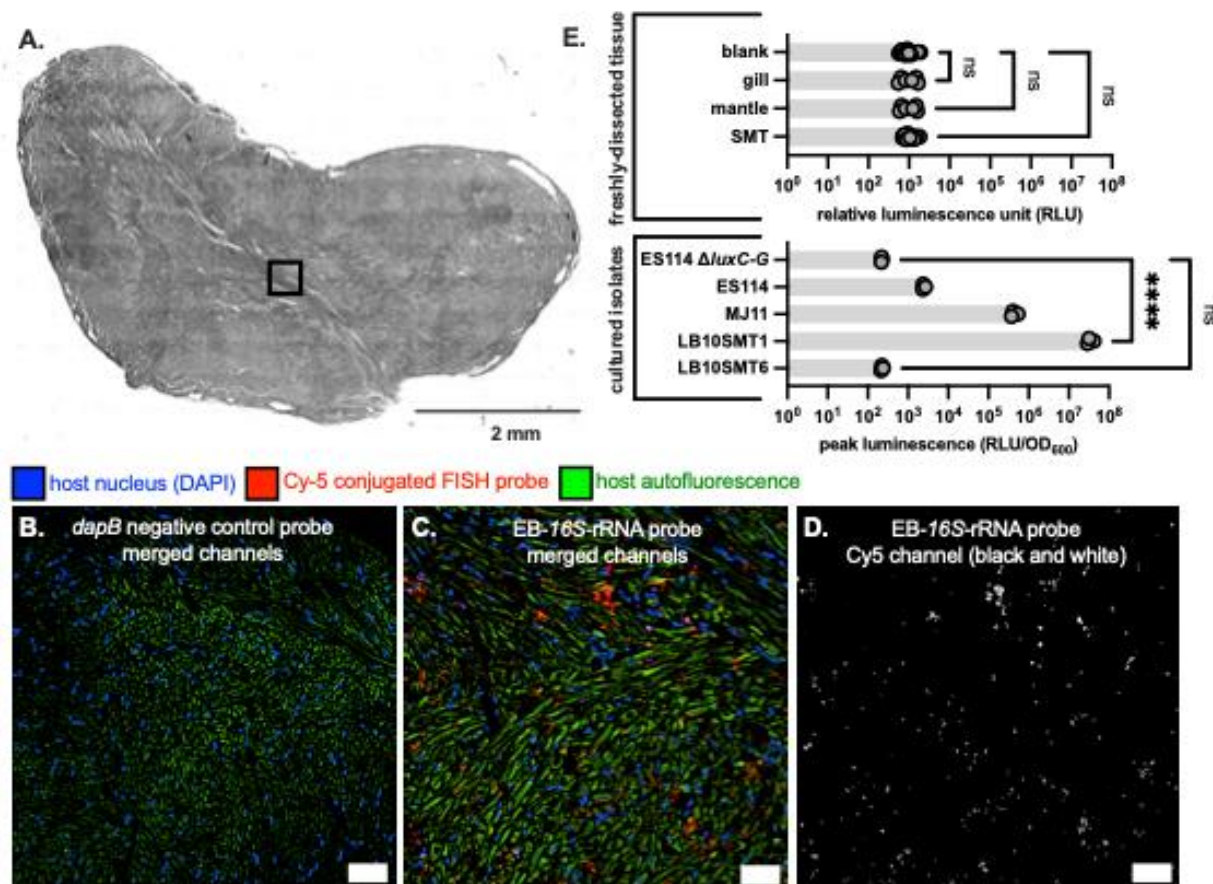


**Figure 4.5. Sub-mantle tissue is not characteristic of other light organs.** **A.** Stitched DIC micrograph of fixed, paraffin-embedded section of *L. brevis* sub-mantle tissue. Physical map of the sub-mantle tissue as imaged by light microscopy. To capture the entire organ, 17 x 10 fields of view were imaged using a DIC filter cassette and stitched with 15% overlap. Scale bar = 2 mm. Black box represents relative size and location of panels (B) – (D) compared to the overall sub-mantle tissue structure. **B.** Merged micrograph of *L. brevis* sub-mantle tissue section including the *dapB* Cy5-conjugated fluorescence *in situ* hybridization (FISH) probe used as a negative control (red; signal absent), squid nuclei (blue; DAPI), or squid connective tissue (green; autofluorescence). **C.** Merged micrograph of *L. brevis* sub-mantle tissue section including the EB-16S-rRNA Cy5 conjugated FISH probe (red; a combination of single-cells and aggregates are observed), squid nucleos (blue; DAPI), or squid connective tissue (green; autofluorescence). **D.** Single-channel micrograph of the EB-16S-rRNA Cy5 conjugated FISH probe from panel (C); red signal has been false-colored white for more visible contrast. Scale bar for panels (B) – (D) = 50  $\mu$ m. All microscopy was performed on parallel sections of sub-mantle tissue obtained from five individual *L. brevis* specimens. **E.** Relative luminescence of freshly dissected *L. brevis* tissue, measured in the field within 1 h of collection. Blank represents 1 mL fresh seawater from the trawl site. Peak luminescence of isolates in culture, calculated for all strains by (lum/OD<sub>600</sub>) at OD<sub>600</sub> = 1.8. Experiment was repeated twice (n = 3), representative data shown here. All measurements in (E) were collected using the same luminometer.

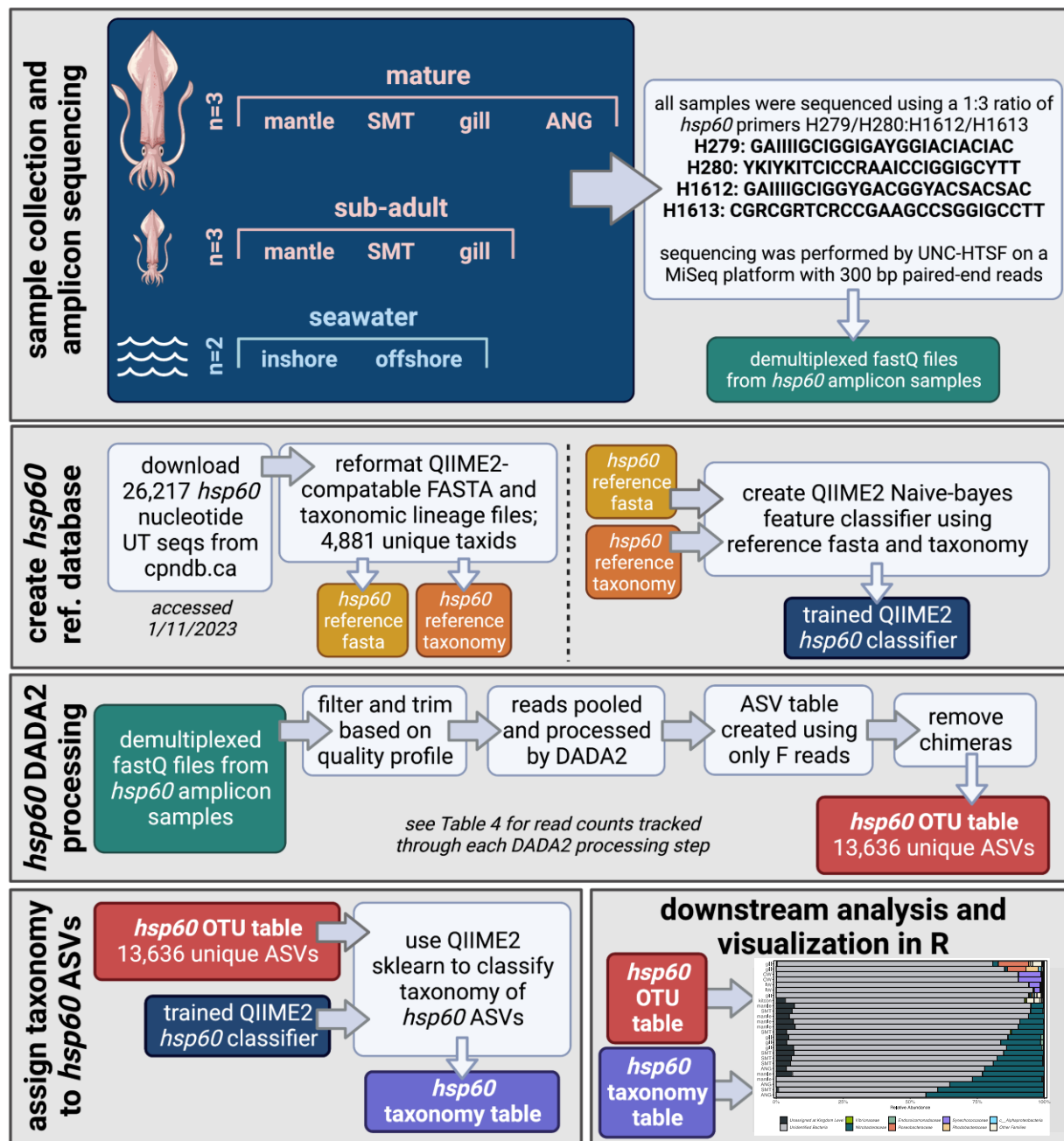
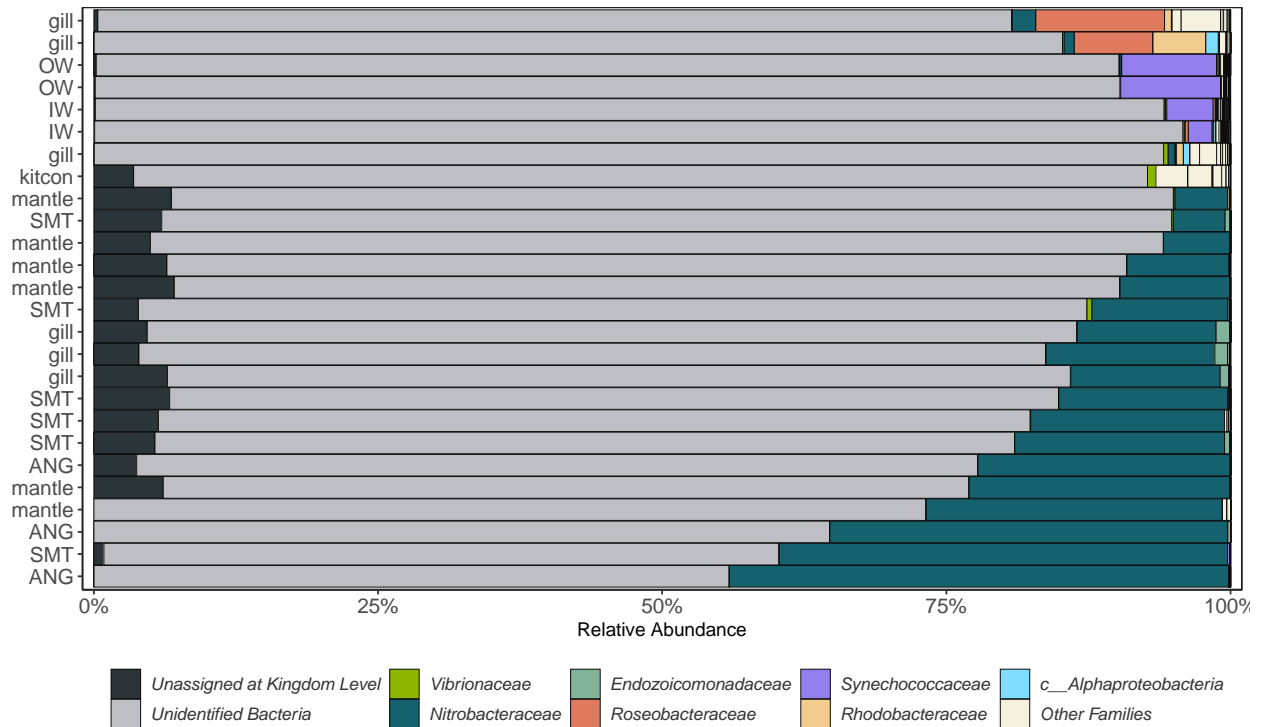
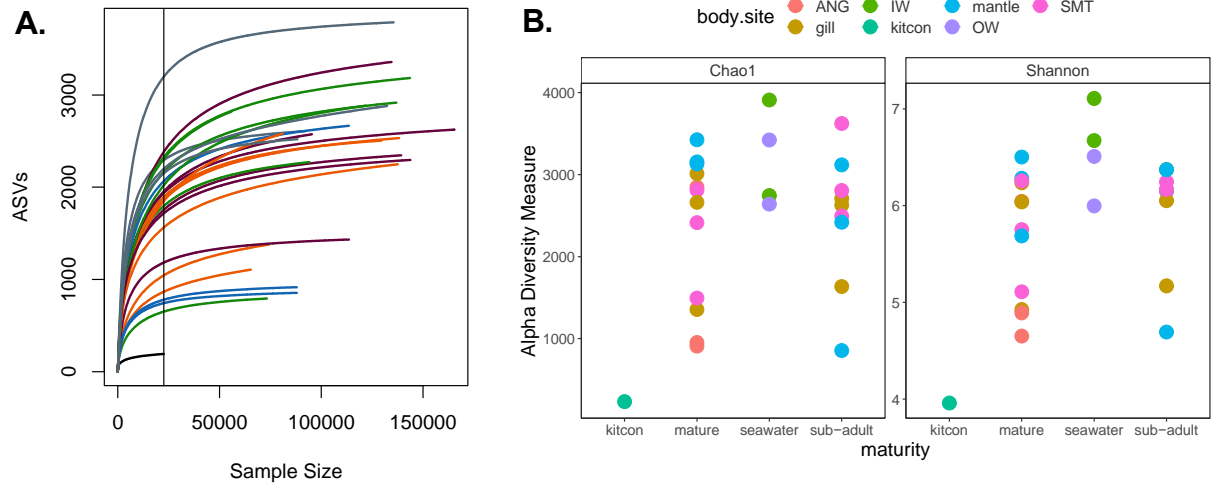


Figure 4.6. Amplicon sequencing and bioinformatic processing workflow.



**Figure 4.7. Community composition based on hsp60 amplicon sequences.** Relative abundance of taxa across all samples. Samples are ordered based on Euclidean distance and labeled by body site. Unique ASVs were renamed and clustered based on their best taxonomic match. “Unassigned at Kingdom Level” indicates ASVs that did not receive any taxonomic identification, even at the Kingdom level. “Unidentified Bacteria” indicates ASVs that were identified as bacteria at the Kingdom level but received no further taxonomic designation. The top 7 Families identified across all samples by abundance are indicated with unique colors; all other ASVs received Family-level taxonomic identification and are grouped and labeled as “Other Families”.





**Figure 4.8. Rarefaction and alpha diversity measures for *hsp60* amplicon samples.** **A.** Rarefaction curve for all samples that were used for *hsp60* amplicon sequencing. X-axis indicates sample size (reads per sample), y-axis indicates number of ASVs identified, and the solid vertical line indicates the minimum reads from a single sample (sample ID = kitcon). Lines are color-coded based on body site using the same color palette as **(B)**. **B.** Chao1 and Shannon alpha diversity measures for all *hsp60* amplicon samples. Samples are grouped by maturity (or seawater/kitcon as indicated) on the x-axis, and color-coded by body site.

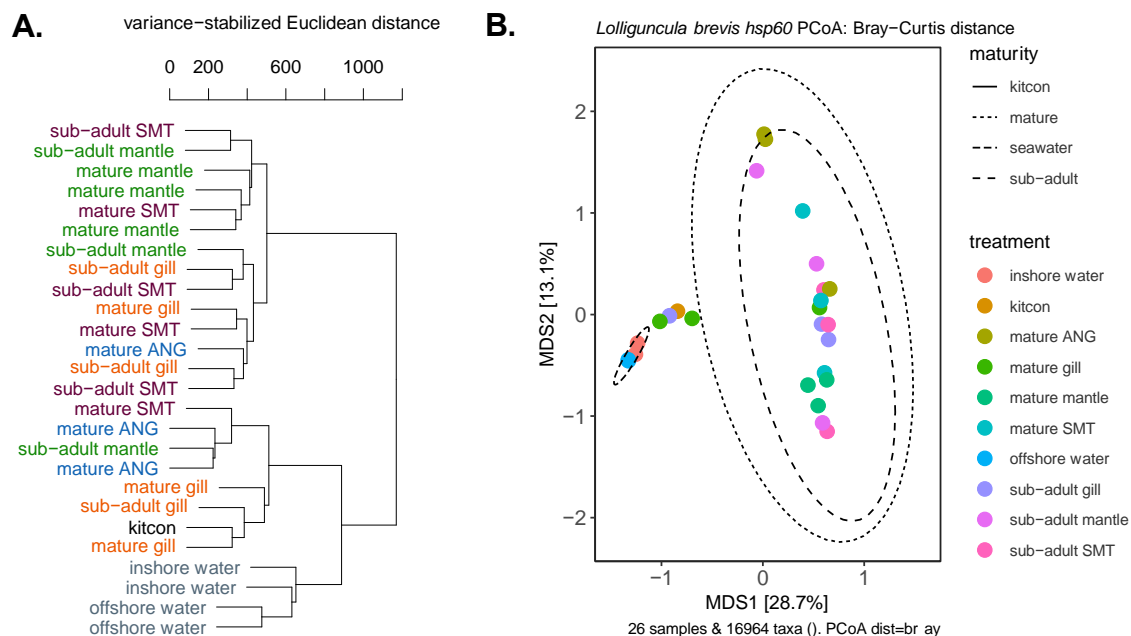


**Figure 4.9. *L. brevis* samples are distinct from seawater and kitcon samples at the community-level.** **A.** Dendrogram depicting the variance-stabilized Euclidean distance between samples. Samples are labeled by treatment and color-coded by body site. Purple = SMT; green = mantle; orange = gill; blue = ANG; black = kit control (kitcon); gray = seawater. **B.** PCoA plot using the Bray-Curtis distance calculation of all samples. Treatments are color-coded and ellipses were plotted according to the maturity/seawater variable.



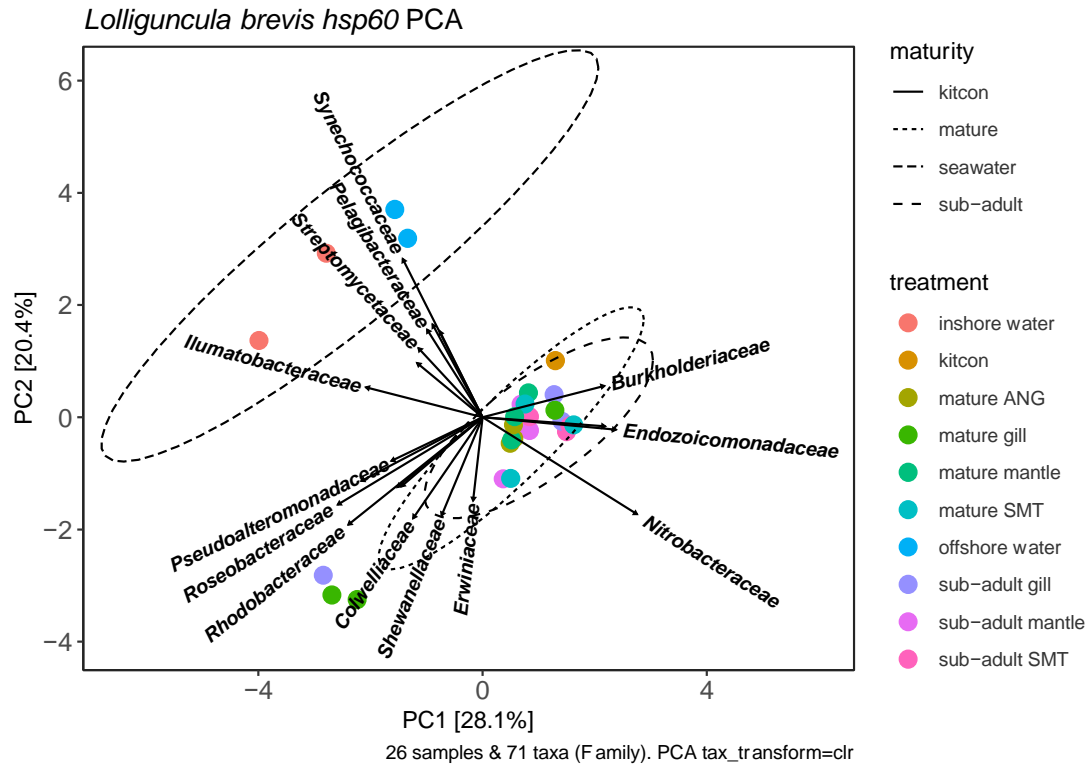


**Figure 4.10. *L. brevis* hosts a distinct, conserved microbial community.** PCA plot comparing the community similarity across treatments according to body site and maturity. Treatments are color-coded and ellipses are plotted according to the maturity/seawater variable. The top 13 families driving these groupings are labeled and indicated as vectors.

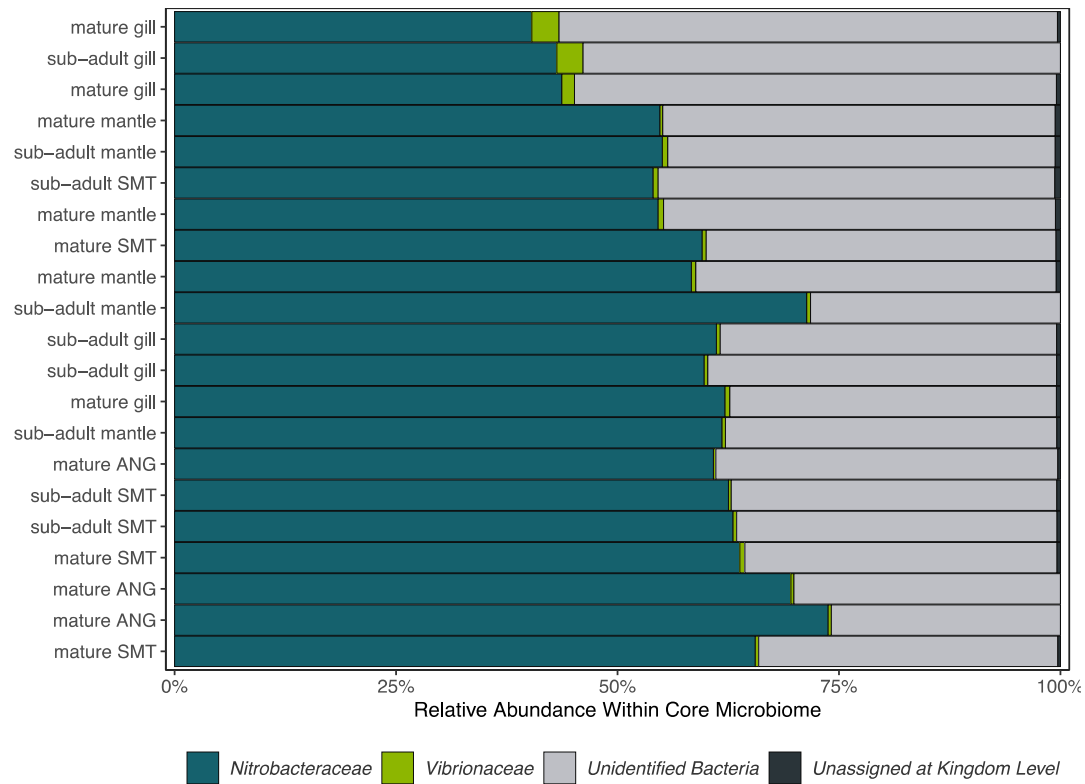


**Figure 4.11. Core microbiome of *L. brevis*.** A stacked bar plot showing the core microbial community as identified by 0.005 detection and 0.8 prevalence parameters across all squid samples at the family level. Relative abundance was calculated as a percentage of the core community. Bars are labeled by treatment and ordered by Euclidean distance.

A.

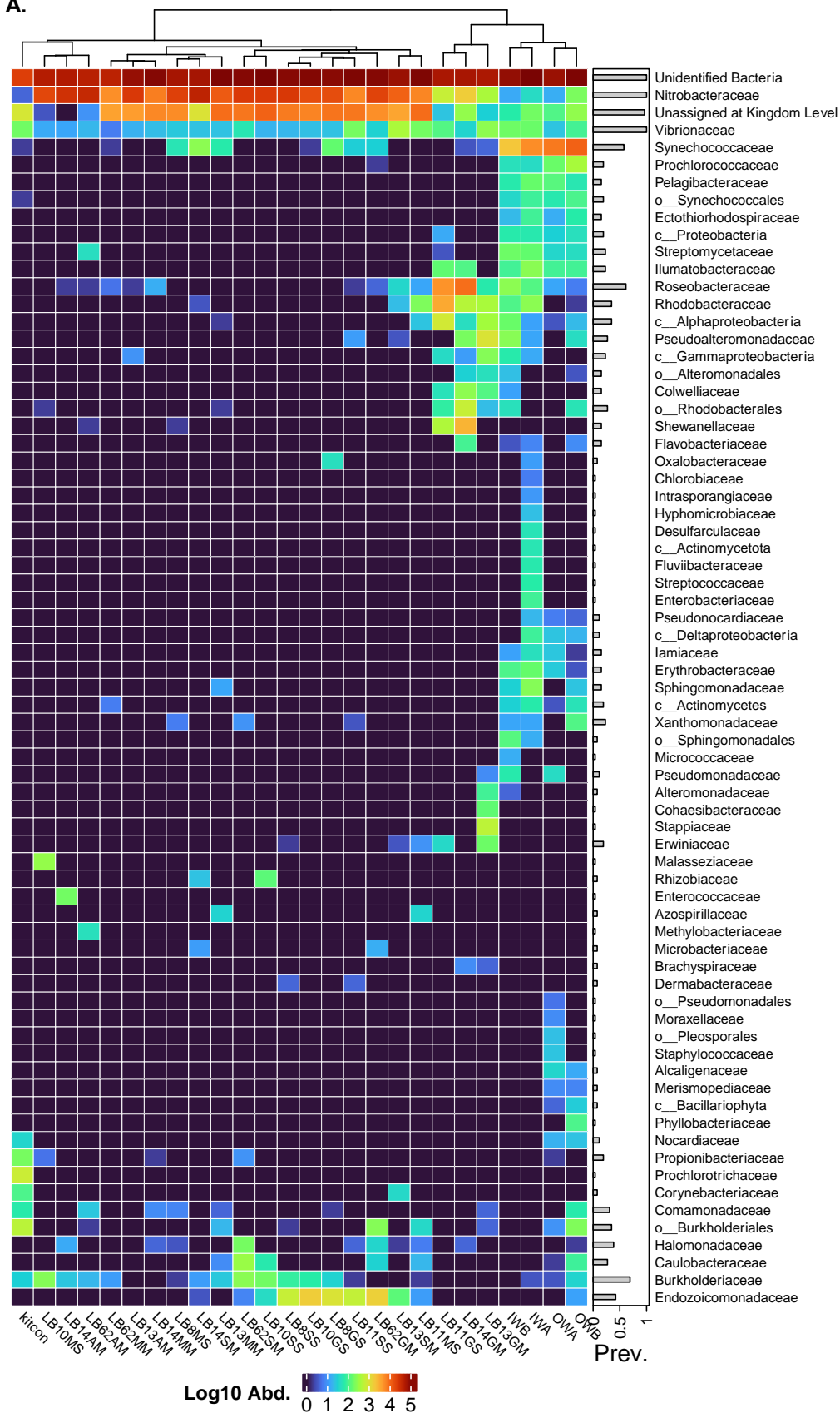




**Figure 4.12. Top 100 taxa across all hsp60 amplicon samples.** A heat plot showing the top 100 unique families **(A)** or ASVs **(B)** across all *hsp60* amplicon samples from this study. Each column is labeled by Sample ID. The dendrogram across the top of the plot represents the *Euclidean* distance between samples. Prev. indicates the prevalence of each taxa across samples, i.e. Prev = 1 indicates that the taxa is conserved across all samples.

				top NCBI BLAST hit						
query		date accessed	scientific name	max	total	query	E	%	acc. length	accession ID
Squid ID	length (bp)			score	score	cover	value	identity	(bp)	
DP1	624	1/17/23	<i>Doryteuthis pleii</i>	1151	1151	84%	0	99.22%	658	AY039619.1
LB13	624	1/17/23	<i>Lolliguncula brevis</i>	1160	1160	84%	0	99.53%	657	KU905932.1
LB14	624	1/17/23	<i>Lolliguncula brevis</i>	1160	1160	84%	0	99.53%	657	KU905932.1
LB15	624	1/17/23	<i>Lolliguncula brevis</i>	1168	1168	84%	0	99.69%	657	KU905932.1

**Table 4.1. Squid COI NCBI BLAST hits.**

body site:	mantle		gill		sub-mantle tissue		ANG	seawater		
maturity:	sub-adult	mature	sub-adult	mature	sub-adult	mature	mature	inshore	offshore	kit con.
luminescence	6		6		15	2			17	
DIC microscopy						5				
FISH microscopy						5				
16S amplicon seq			3	3			3	2	2	1
<i>hsp60</i> amplicon seq	3	3	3	3	3	3	3	2	2	1

Table 4.2. Squid sample breakdown.

				top NCBI BLAST hit										
Internal ID	Manuscript ID	squid host	body site	date accessed	scientific name	max score	total score	query cover	E value	% identity	acc. length (bp)	accession ID	reference	
LB10LO4	LB10_SMT4	<i>Lolliguncula brevis</i>	sub-mantle tissue (SMT)	1/17/23	<i>Vibrio sp.</i> ED002	473	473	66%	1.00E-128	86.36%	3645534	CP080238.1	this study	
LB15G3	LB15_G3	<i>Lolliguncula brevis</i>	gill (G)	1/17/23	<i>Vibrio jasicida</i> 090810c	545	545	71%	3.00E-150	89.37%	3690481	CP025792.1	this study	
LB14LO2	LB14_SMT2	<i>Lolliguncula brevis</i>	sub-mantle tissue (SMT)	1/17/23	<i>Vibrio jasicida</i> 090810c	584	584	84%	6.00E-162	87.10%	3690481	CP025792.1	this study	
LB15G1	LB15_G1	<i>Lolliguncula brevis</i>	gill (G)	1/17/23	<i>Vibrio jasicida</i> 090810c	623	623	83%	1.00E-173	88.63%	3690481	CP025792.1	this study	
LB7G3	DP1_G3	<i>Doryteuthis pleii</i>	gill (G)	1/17/23	<i>Vibrio sp.</i> B1REV9	939	939	84%	0	99.42%	1894653	HG992745.1	this study	
LB10LO7	LB10_SMT7	<i>Lolliguncula brevis</i>	sub-mantle tissue (SMT)	1/17/23	<i>Vibrio sp.</i> B1REV9	948	948	84%	0	99.24%	1894653	HG992745.1	this study	
LB11LO2	LB11_SMT2	<i>Lolliguncula brevis</i>	sub-mantle tissue (SMT)	1/17/23	<i>Vibrio harveyi</i>	922	922	85%	0	98.30%	624	DQ279074.1	this study	
LB11G2	LB11_G2	<i>Lolliguncula brevis</i>	gill (G)	1/17/23	<i>Vibrio harveyi</i>	924	924	83%	0	99.03%	3713225	CP025537.1	this study	
LB14LO8	LB14_SMT8	<i>Lolliguncula brevis</i>	sub-mantle tissue (SMT)	1/17/23	<i>Vibrio sp.</i> SCSIO 43155	955	955	85%	0	99.43%	3568316	CP071852.1	this study	
LB10LO2	LB10_SMT2	<i>Lolliguncula brevis</i>	sub-mantle tissue (SMT)	1/17/23	<i>Vibrio owensii</i>	815	815	84%	0	94.84%	3797023	CP025796.1	this study	
LB15G2	LB15_G2	<i>Lolliguncula brevis</i>	gill (G)	1/17/23	<i>Vibrio campbellii</i>	900	900	85%	0	97.19%	3524636	CP033134.1	this study	
LB11G1	LB11_G1	<i>Lolliguncula brevis</i>	gill (G)	1/17/23	<i>Vibrio sp.</i> B1ASS3	950	950	85%	0	99.24%	4055171	HG992742.1	this study	
LB11LO1	LB11_SMT1	<i>Lolliguncula brevis</i>	sub-mantle tissue (SMT)	1/17/23	<i>Vibrio sp.</i> B1ASS3	952	952	84%	0	99.62%	4055171	HG992742.1	this study	
LB15LO3	LB15_SMT3	<i>Lolliguncula brevis</i>	sub-mantle tissue (SMT)	1/17/23	<i>Vibrio campbellii</i>	941	941	84%	0	99.23%	3524636	CP033134.1	this study	
LB11LO3	LB11_SMT3	<i>Lolliguncula brevis</i>	sub-mantle tissue (SMT)	1/17/23	<i>Vibrio campbellii</i>	946	946	84%	0	99.43%	3581305	CP025953.1	this study	
LB10LO3	LB10_SMT3	<i>Lolliguncula brevis</i>	sub-mantle tissue (SMT)	1/17/23	<i>Vibrio rotiferianus</i>	966	966	85%	0	99.81%	3326271	CP018312.1	this study	
LB15LO1	LB15_SMT1	<i>Lolliguncula brevis</i>	sub-mantle tissue (SMT)	1/17/23	<i>Vibrio campbellii</i>	942	942	85%	0	99.05%	3524636	CP033134.1	this study	
LB7LO2	DP1_SMT2	<i>Doryteuthis pleii</i>	sub-mantle tissue (SMT)	1/17/23	<i>Vibrio owensii</i>	944	944	84%	0	99.42%	3797023	CP02576.1	this study	
LB14G3	LB14_G3	<i>Lolliguncula brevis</i>	gill (G)	1/17/23	<i>Vibrio campbellii</i>	955	955	85%	0	99.43%	3524636	CP033134.1	this study	
LB14G2	LB14_G2	<i>Lolliguncula brevis</i>	gill (G)	1/17/23	<i>Vibrio campbellii</i>	955	955	85%	0	99.43%	3524636	CP033134.1	this study	
LB14LO3	LB14_SMT3	<i>Lolliguncula brevis</i>	sub-mantle tissue (SMT)	1/17/23	<i>Vibrio campbellii</i>	966	966	86%	0	99.25%	3524636	CP033134.1	this study	
LB10LO1	LB10_SMT1	<i>Lolliguncula brevis</i>	sub-mantle tissue (SMT)	1/17/23	<i>Vibrio campbellii</i>	966	966	86%	0	99.62%	3469516	CP026321.1	Septer et al. 2020	
LB15LO2	LB15_SMT2	<i>Lolliguncula brevis</i>	sub-mantle tissue (SMT)	1/17/23	<i>Vibrio hyugaensis</i>	689	689	83%	0	90.93%	3530957	CP025794.1	this study	
LB11G3	LB11_G3	<i>Lolliguncula brevis</i>	gill (G)	1/17/23	<i>Vibrio jasicida</i> 090810c	839	839	84%	0	95.78%	3690481	CP025792.1	this study	
LB14LO7	LB14_SMT7	<i>Lolliguncula brevis</i>	sub-mantle tissue (SMT)	1/17/23	<i>Vibrio hyugaensis</i>	953	953	84%	0	99.81%	3530957	CP025794.1	this study	
LB7G2	DP1_G2	<i>Doryteuthis pleii</i>	gill (G)	1/17/23	<i>Vibrio jasicida</i> 090810c	946	946	84%	0	99.42%	3690481	CP025792.1	this study	
LB7LO1	DP1_SMT1	<i>Doryteuthis pleii</i>	sub-mantle tissue (SMT)	1/17/23	<i>Vibrio jasicida</i> 090810c	935	935	83%	0	99.23%	3690481	CP025792.1	this study	
LB10G1	LB10_G1	<i>Lolliguncula brevis</i>	gill (G)	1/17/23	<i>Vibrio jasicida</i> 090810c	929	929	83%	0	99.22%	3690481	CP025792.1	this study	
LB10G2	LB10_G2	<i>Lolliguncula brevis</i>	gill (G)	1/17/23	<i>Vibrio jasicida</i> 090810c	950	950	84%	0	99.62%	3690481	CP025792.1	this study	
LB10G3	LB10_G3	<i>Lolliguncula brevis</i>	gill (G)	1/17/23	<i>Vibrio jasicida</i> 090810c	950	950	84%	0	99.62%	3690481	CP025792.1	this study	
LB11LO6	LB11_SMT6	<i>Lolliguncula brevis</i>	sub-mantle tissue (SMT)	1/17/23	<i>Vibrio zhuhaiensis</i>	878	878	83%	0	97.30%	3329049	AP019660.1	this study	
LB10LO6	LB10_SMT6	<i>Lolliguncula brevis</i>	sub-mantle tissue (SMT)	1/17/23	<i>Aliivibrio fischeri</i> MJ11	922	922	83%	0	98.84%	2905029	CP001139.1	Suria et al. 2022	
LB14LO1	LB14_SMT1	<i>Lolliguncula brevis</i>	sub-mantle tissue (SMT)	1/17/23	<i>Vibrio sp.</i> THAF190c	754	754	84%	0	92.93%	3313709	CP045338.1	this study	
LB7G1	DP1_G1	<i>Doryteuthis pleii</i>	gill (G)	1/17/23	<i>Vibrio sp.</i> PID32_28	833	833	74%	0	99.35%	500	KM574571.1	this study	
LB7LO4	DP1_SMT4	<i>Doryteuthis pleii</i>	sub-mantle tissue (SMT)	1/17/23	<i>Vibrio sp.</i> PID32_28	839	839	75%	0	99.35%	500	KM574571.1	this study	
LB14G1	LB14_G1	<i>Lolliguncula brevis</i>	gill (G)	1/17/23	<i>Vibrio sp.</i> THAF190c	928	928	84%	0	99.03%	3313709	CP045338.1	this study	
LB14LO6	LB14_SMT6	<i>Lolliguncula brevis</i>	sub-mantle tissue (SMT)	1/17/23	<i>Vibrio fortis</i>	880	880	84%	0	97.12%	3262072	AP025487.1	this study	

Table 4.3. Cultured isolates *hsp60* NCBI BLAST hits.



<i>hsp60</i>								final % reads
<b>samples</b>	<b>treatment</b>	<b>dada2_input</b>	<b>filtered</b>	<b>denoisedF</b>	<b>denoisedFpool</b>	<b>nonchim</b>	<b>retained</b>	
<b>IWA</b>	inshore water	274686	165967	148403	148403	137155	49.9	
<b>IWB</b>	inshore water	176142	111204	100199	100199	92882	52.7	
<b>kitcon</b>	kit control	109487	35027	32592	32592	25224	23	
<b>LB13AM</b>	mature ANG	221000	133858	122991	122991	113892	51.5	
<b>LB14AM</b>	mature ANG	196076	106911	99658	99658	87932	44.8	
<b>LB62AM</b>	mature ANG	205855	108193	100563	100563	87958	42.7	
<b>LB13GM</b>	mature gill	145752	88518	76609	76609	65297	44.8	
<b>LB14GM</b>	mature gill	223879	126740	97091	97091	80763	36.1	
<b>LB62GM</b>	mature gill	267034	162396	151589	151589	137617	51.5	
<b>LB13MM</b>	mature mantle	292253	171764	158181	158181	144206	49.3	
<b>LB14MM</b>	mature mantle	227536	142879	129947	129947	122202	53.7	
<b>LB62MM</b>	mature mantle	112325	66707	61014	61014	56094	49.9	
<b>LB13SM</b>	mature SMT	191367	113900	103445	103445	95650	50	
<b>LB14SM</b>	mature SMT	223822	133016	123110	123110	113563	50.7	
<b>LB62SM</b>	mature SMT	282020	168158	156797	156797	143730	51	
<b>OWA</b>	offshore water	176466	113771	98216	98216	88270	50	
<b>OWB</b>	offshore water	268118	164523	150334	150334	135093	50.4	
<b>LB8GS</b>	sub-adult gill	270891	153839	142782	142782	129973	48	
<b>LB10GS</b>	sub-adult gill	261397	163699	151419	151419	138515	53	
<b>LB11GS</b>	sub-adult gill	166901	104426	89259	89259	74278	44.5	
<b>LB8MS</b>	sub-adult mantle	189001	111109	102613	102613	94217	49.9	
<b>LB10MS</b>	sub-adult mantle	178647	92858	86217	86217	73336	41.1	
<b>LB11MS</b>	sub-adult mantle	268832	163938	151359	151359	137148	51	
<b>LB8SS</b>	sub-adult SMT	281704	164504	153345	153345	139798	49.6	
<b>LB10SS</b>	sub-adult SMT	326872	197375	182617	182617	165952	50.8	
<b>LB11SS</b>	sub-adult SMT	257106	162344	147105	147105	134727	52.4	

**Table 4.4. *hsp60* read counts tracked through DADA2 processing steps.**

## CONCLUDING REMARKS

Symbioses between bacteria and their eukaryotic hosts can be found in nearly any environment, and despite incredible diversity across systems, the mechanisms by which bacteria evolve and compete during host-colonization remain largely conserved. Host environments provide a unique physical niche where symbionts are forced into contact with other microbes and have the opportunity to compete for colonization sites or exchange DNA via contact-mediated mechanisms. The light organ of *Euprymna scolopes* squid is colonized exclusively by the bioluminescent bacterium *Vibrio fischeri* and has long been used as a model for studying host-colonization processes because of its simplified microbiome. *V. fischeri* encodes a type VI secretion system – a contact-dependent killing mechanism that *V. fischeri* uses to compete for colonization sites within the squid light organ. Additionally, *V. fischeri* encodes both conserved and strain-specific mechanisms for horizontal gene transfer. Despite decades of research studying the light organ association between *V. fischeri* and *E. scolopes*, questions remain about the diversity of host-associated bacteria and how competition and HGT impact their ability to colonize light organ niche.

Given that squid have already proven to be excellent model systems for studying host-symbiont interactions, it is surprising that we do not have a better understanding of squid microbiomes across different body sites. As described above, the light organ of Hawaiian bobtail squid is colonized exclusively by *Vibrio fischeri*. More diverse *Vibrios* have been isolated from the light organs of other squid species; however, the Hawaiian bobtail squid remains the primary model squid host for studying symbioses. Recent work has also characterized the accessory nidamental gland (ANG) of *E. scolopes* and its associated microbial community. The ANG is a female reproductive organ that has been described in several *Sepiolid* and *Loliginid* squid species and hosts a diverse bacterial community that is excreted into the egg jelly coat as they are laid and has been shown in *E. scolopes* to protect against bacterial and fungal infection during embryo development. While both the light organ and ANG have been studied

separately, these organs are not conserved across all squid species, and we do not understand how the microbial communities of light organs, ANGs, or more conserved body sites differ within individual squid.

To that end, the overarching goal of my dissertation work was to use creative approaches to design and implement new tools to further our understanding of microbial interactions within symbioses. The first three chapters of my dissertation utilize the *E. scolopes* – *V. fischeri* light organ association as a model system. In chapter one, I designed a novel fluorescence microscopy assay and analysis workflow for quantifying contact-dependent killing at the single-cell level. In chapter two, I combined this assay with a subcellular model for T6SS interactions; the results of this study revealed that strains with the ability to activate T6SS more quickly will dominate competitive interactions, even if both strains are lethal. In my third chapter, I designed an experimental evolution assay that uses selectable antibiotic markers to quantify gene transfer between *V. fischeri* strains during coculture. The results of this study revealed that the conditions required for DNA transfer in our experimental evolution assay are inconsistent with any mechanism of gene transfer that has previously been described in *V. fischeri*. In my final chapter, I characterized the microbiome of the Atlantic brief squid, *Lolliguncula brevis* across multiple body sites and found that *L. brevis* hosts a very conserved microbiome that is dominated by *Bradyrhizobium*, *Aliivibrio*, and unidentified bacteria. This chapter serves as a pilot study for understanding broader squid-symbiont associations and warrants future work to further address the findings I describe here.

In future amplicon-based studies where the broader microbial community is not yet known, I recommend starting with a 16S amplicon target before proceeding with an amplicon target like *hsp60* that has not been properly validated across diverse taxa. Reference repositories for 16S *rRNA* sequences are maintained regularly and contain much more diverse sequence representation, which likely would have resulted in better taxonomic identification of the *L. brevis* community. This pilot study was an incredible learning experience, and I conclude this dissertation with many more questions and ideas than concrete answers. Ultimately, the work I present in my dissertation is a culmination of how I have grown as a scientist over the past seven years, and I hope that my contributions to the squid symbiosis community will drive us forward in answering new and more complex research questions as we continue to learn more about how these systems function.

## REFERENCES

1. Oulhen, N., B.J. Schulz, and T.J. Carrier, *English translation of Heinrich Anton de Bary's 1878 speech, 'Die Erscheinung der Symbiose' ('De la symbiose')*. Symbiosis, 2016. **69**(3): p. 131-139.
2. Goffredi, S.K., et al., *Evolutionary innovation: a bone-eating marine symbiosis*. Environmental Microbiology, 2005. **7**(9): p. 1369-1378.
3. Goffredi, S.K., S.B. Johnson, and R.C. Vrijenhoek, *Genetic diversity and potential function of microbial symbionts associated with newly discovered species of Osedax polychaete worms*. Applied and environmental microbiology, 2007. **73**(7): p. 2314-2323.
4. Kneip, C., et al., *Nitrogen fixation in eukaryotes—new models for symbiosis*. BMC Evolutionary Biology, 2007. **7**(1): p. 1-12.
5. Fiore, C.L., et al., *Nitrogen fixation and nitrogen transformations in marine symbioses*. Trends in microbiology, 2010. **18**(10): p. 455-463.
6. Masson-Boivin, C. and J.L. Sachs, *Symbiotic nitrogen fixation by rhizobia—the roots of a success story*. Current Opinion in Plant Biology, 2018. **44**: p. 7-15.
7. Silverman, J.M., et al., *Structure and regulation of the type VI secretion system*. Annual review of microbiology, 2012. **66**: p. 453.
8. Ho, B.T., T.G. Dong, and J.J. Mekalanos, *A view to a kill: the bacterial type VI secretion system*. Cell host & microbe, 2014. **15**(1): p. 9-21.
9. Granato, E.T., T.A. Meiller-Legrand, and K.R. Foster, *The evolution and ecology of bacterial warfare*. Current biology, 2019. **29**(11): p. R521-R537.
10. Singh, R.P. and K. Kumari, *Bacterial type VI secretion system (T6SS): an evolved molecular weapon with diverse functionality*. Biotechnology Letters, 2023: p. 1-23.
11. Vacheron, J., et al., *T6SS contributes to gut microbiome invasion and killing of an herbivorous pest insect by plant-beneficial Pseudomonas protegens*. The ISME journal, 2019. **13**(5): p. 1318-1329.
12. Chen, C., X. Yang, and X. Shen, *Confirmed and potential roles of bacterial T6SSs in the intestinal ecosystem*. Frontiers in microbiology, 2019. **10**: p. 1484.
13. Steele, M.I., et al., *The gut microbiota protects bees from invasion by a bacterial pathogen*. Microbiology spectrum, 2021. **9**(2): p. e00394-21.
14. Suria, A.M., et al., *Prevalence and diversity of type VI secretion systems in a model beneficial symbiosis*. Frontiers in Microbiology, 2022. **13**.
15. Coulthurst, S., *The Type VI secretion system: a versatile bacterial weapon*. Microbiology, 2019. **165**(5): p. 503-515.
16. Henry, L.M., et al., *Horizontally transmitted symbionts and host colonization of ecological niches*. Current biology, 2013. **23**(17): p. 1713-1717.

17. Hall, R.J., et al., *Horizontal gene transfer as a source of conflict and cooperation in prokaryotes*. Frontiers in Microbiology, 2020. **11**: p. 1569.
18. Thomas, C.M. and K.M. Nielsen, *Mechanisms of, and barriers to, horizontal gene transfer between bacteria*. Nature reviews microbiology, 2005. **3**(9): p. 711-721.
19. Arnold, B.J., I.-T. Huang, and W.P. Hanage, *Horizontal gene transfer and adaptive evolution in bacteria*. Nature Reviews Microbiology, 2022. **20**(4): p. 206-218.
20. Ippen-Ihler, K. and E. Minkley Jr, *The conjugation system of F, the fertility factor of Escherichia coli*. Annual review of genetics, 1986. **20**(1): p. 593-624.
21. Gray, T.A. and K.M. Derbyshire, *Blending genomes: distributive conjugal transfer in mycobacteria, a sexier form of HGT*. Molecular microbiology, 2018. **108**(6): p. 601-613.
22. Dordet-Frisoni, E., et al., *Mycoplasma chromosomal transfer: a distributive, conjugative process creating an infinite variety of mosaic genomes*. Frontiers in Microbiology, 2019. **10**: p. 2441.
23. Adelberg, E.A. and J. Pittard, *Chromosome transfer in bacterial conjugation*. Bacteriological reviews, 1965. **29**(2): p. 161-172.
24. Hanlon, R.T., et al., *Laboratory culture of the sepiolid squid Euprymna scolopes: a model system for bacteria-animal symbiosis*. The Biological Bulletin, 1997. **192**(3): p. 364-374.
25. Stabb, E.V., *The Vibrio fischeri–Euprymna scolopes light organ symbiosis*. The biology of vibrios, 2006: p. 204-218.
26. Visick, K.L., E.V. Stabb, and E.G. Ruby, *A lasting symbiosis: how Vibrio fischeri finds a squid partner and persists within its natural host*. Nature Reviews Microbiology, 2021. **19**(10): p. 654-665.
27. Nyholm, S.V. and M.J. McFall-Ngai, *A lasting symbiosis: how the Hawaiian bobtail squid finds and keeps its bioluminescent bacterial partner*. Nature Reviews Microbiology, 2021. **19**(10): p. 666-679.
28. Ruby, E.G. and K.-H. Lee, *The Vibrio fischeri-Euprymna scolopes light organ association: current ecological paradigms*. Applied and environmental microbiology, 1998. **64**(3): p. 805-812.
29. Haygood, M.G., *Light a organ symbioses in fishes*. Critical reviews in microbiology, 1993. **19**(4): p. 191-216.
30. Mandel, M.J. and A.K. Dunn, *Impact and influence of the natural Vibrio-squid symbiosis in understanding bacterial–animal interactions*. Frontiers in microbiology, 2016. **7**: p. 1982.
31. Mandel, M.J., et al., *A single regulatory gene is sufficient to alter bacterial host range*. Nature, 2009. **458**(7235): p. 215-218.
32. Visick, K.L. and M.J. McFall-Ngai, *An exclusive contract: specificity in the Vibrio fischeri-Euprymna scolopes partnership*. Journal of Bacteriology, 2000. **182**(7): p. 1779-1787.

33. Septer, A.N., et al., *The haem-uptake gene cluster in Vibrio fischeri is regulated by Fur and contributes to symbiotic colonization*. Environmental microbiology, 2011. **13**(11): p. 2855-2864.
34. Sun, Y., et al., *Intraspecific competition impacts Vibrio fischeri strain diversity during initial colonization of the squid light organ*. Applied and environmental microbiology, 2016. **82**(10): p. 3082-3091.
35. Bongrand, C. and E.G. Ruby, *Achieving a multi-strain symbiosis: strain behavior and infection dynamics*. The ISME journal, 2019. **13**(3): p. 698-706.
36. Bongrand, C., et al., *Using colonization assays and comparative genomics to discover symbiosis behaviors and factors in Vibrio fischeri*. Mbio, 2020. **11**(2): p. e03407-19.
37. Brooks, J.F., et al., *Global discovery of colonization determinants in the squid symbiont Vibrio fischeri*. Proceedings of the National Academy of Sciences, 2014. **111**(48): p. 17284-17289.
38. Speare, L., et al., *Bacterial symbionts use a type VI secretion system to eliminate competitors in their natural host*. Proceedings of the National Academy of Sciences, 2018. **115**(36): p. E8528-E8537.
39. Speare, L., et al., *Environmental viscosity modulates interbacterial killing during habitat transition*. MBio, 2020. **11**(1): p. e03060-19.
40. Smith, S., et al., *Activation of the Type VI Secretion System in the Squid Symbiont Vibrio fischeri Requires the Transcriptional Regulator TasR and the Structural Proteins TssM and TssA*. Journal of bacteriology, 2021. **203**(21): p. e00399-21.
41. Pollack-Berti, A., M.S. Wollenberg, and E.G. Ruby, *Natural transformation of Vibrio fischeri requires tfoX and tfoY*. Environmental microbiology, 2010. **12**(8): p. 2302-2311.
42. Dunn, A.K., M.O. Martin, and E.V. Stabb, *Characterization of pES213, a small mobilizable plasmid from Vibrio fischeri*. Plasmid, 2005. **54**(2): p. 114-134.
43. Speare, L. and A.N. Septer, *Coincubation assay for quantifying competitive interactions between Vibrio fischeri isolates*. J Vis Exp, 2019.
44. Frost, I., et al., *Cooperation, competition and antibiotic resistance in bacterial colonies*. The ISME journal, 2018. **12**(6): p. 1582-1593.
45. Stubbendieck, R.M., C. Vargas-Bautista, and P.D. Straight, *Bacterial communities: interactions to scale*. Frontiers in microbiology, 2016. **7**: p. 1234.
46. Souza, D.P., et al., *Bacterial killing via a type IV secretion system*. Nature communications, 2015. **6**(1): p. 1-9.
47. Anderson, M.C., et al., *Shigella sonnei encodes a functional T6SS used for interbacterial competition and niche occupancy*. Cell host & microbe, 2017. **21**(6): p. 769-776. e3.

48. Basler, M., B. Ho, and J. Mekalanos, *Tit-for-tat: type VI secretion system counterattack during bacterial cell-cell interactions*. Cell, 2013. **152**(4): p. 884-894.
49. Guillemette, R., et al., *Insight into the resilience and susceptibility of marine bacteria to T6SS attack by Vibrio cholerae and Vibrio coralliilyticus*. PloS one, 2020. **15**(1): p. e0227864.
50. Hachani, A., N.S. Lossi, and A. Filloux, *A visual assay to monitor T6SS-mediated bacterial competition*. JoVE (Journal of Visualized Experiments), 2013(73): p. e50103.
51. Hibbing, M.E., et al., *Bacterial competition: surviving and thriving in the microbial jungle*. Nature reviews microbiology, 2010. **8**(1): p. 15-25.
52. Ruhe, Z.C., D.A. Low, and C.S. Hayes, *Bacterial contact-dependent growth inhibition*. Trends in microbiology, 2013. **21**(5): p. 230-237.
53. Wood, D.W. and L.S. Pierson III, *The phzI gene of Pseudomonas aureofaciens 30–84 is responsible for the production of a diffusible signal required for phenazine antibiotic production*. Gene, 1996. **168**(1): p. 49-53.
54. Smith, W.P., et al., *The evolution of the type VI secretion system as a disintegration weapon*. PLoS biology, 2020. **18**(5): p. e3000720.
55. Chen, L., et al., *Composition, function, and regulation of T6SS in Pseudomonas aeruginosa*. Microbiological research, 2015. **172**: p. 19-25.
56. Sana, T.G., K.A. Lugo, and D.M. Monack, *T6SS: The bacterial "fight club" in the host gut*. PLoS pathogens, 2017. **13**(6): p. e1006325.
57. Basler, M., *Type VI secretion system: secretion by a contractile nanomachine*. Philosophical Transactions of the Royal Society B: Biological Sciences, 2015. **370**(1679): p. 20150021.
58. Joshi, A., et al., *Rules of engagement: the type VI secretion system in Vibrio cholerae*. Trends in microbiology, 2017. **25**(4): p. 267-279.
59. Nadell, C.D., K. Drescher, and K.R. Foster, *Spatial structure, cooperation and competition in biofilms*. Nature Reviews Microbiology, 2016. **14**(9): p. 589-600.
60. Stubbendieck, R.M. and P.D. Straight, *Multifaceted interfaces of bacterial competition*. Journal of bacteriology, 2016. **198**(16): p. 2145-2155.
61. Septer, A.N., *The Vibrio-squid symbiosis as a model for studying interbacterial competition*. Msystems, 2019. **4**(3): p. e00108-19.
62. Tischler, A.H., K.M. Hodge-Hanson, and K.L. Visick, *Vibrio fischeri–squid symbiosis*. eLS, 2019: p. 1-9.
63. Schindelin, J., et al., *Fiji: an open-source platform for biological-image analysis*. Nature methods, 2012. **9**(7): p. 676-682.

64. Boettcher, K. and E. Ruby, *Depressed light emission by symbiotic Vibrio fischeri of the sepiolid squid Euprymna scolopes*. Journal of Bacteriology, 1990. **172**(7): p. 3701-3706.
65. Doino, J.A. and M.J. McFall-Ngai, *A transient exposure to symbiosis-competent bacteria induces light organ morphogenesis in the host squid*. The Biological Bulletin, 1995. **189**(3): p. 347-355.
66. Dunn, A.K., et al., *New rfp-and pES213-derived tools for analyzing symbiotic Vibrio fischeri reveal patterns of infection and lux expression in situ*. Applied and environmental microbiology, 2006. **72**(1): p. 802-810.
67. Lambertsen, L., C. Sternberg, and S. Molin, *Mini-Tn7 transposons for site-specific tagging of bacteria with fluorescent proteins*. Environmental microbiology, 2004. **6**(7): p. 726-732.
68. Koch, B., L.E. Jensen, and O. Nybroe, *A panel of Tn7-based vectors for insertion of the gfp marker gene or for delivery of cloned DNA into Gram-negative bacteria at a neutral chromosomal site*. Journal of microbiological methods, 2001. **45**(3): p. 187-195.
69. Peterson, B.W., et al., *Bacterial cell surface damage due to centrifugal compaction*. Applied and environmental microbiology, 2012. **78**(1): p. 120-125.
70. Salomon, D., et al., *Vibrio parahaemolyticus type VI secretion system 1 is activated in marine conditions to target bacteria, and is differentially regulated from system 2*. PLoS one, 2013. **8**(4): p. e61086.
71. Sana, T.G., et al., *Salmonella Typhimurium utilizes a T6SS-mediated antibacterial weapon to establish in the host gut*. Proceedings of the National Academy of Sciences, 2016. **113**(34): p. E5044-E5051.
72. Bachmann, V., et al., *Bile salts modulate the mucin-activated type VI secretion system of pandemic Vibrio cholerae*. PLoS neglected tropical diseases, 2015. **9**(8): p. e0004031.
73. Ishikawa, T., et al., *Pathoadaptive conditional regulation of the type VI secretion system in Vibrio cholerae O1 strains*. Infection and immunity, 2012. **80**(2): p. 575-584.
74. Johnson, M.B. and A.K. Criss, *Fluorescence microscopy methods for determining the viability of bacteria in association with mammalian cells*. JoVE (Journal of Visualized Experiments), 2013(79): p. e50729.
75. Stiefel, P., et al., *Critical aspects of using bacterial cell viability assays with the fluorophores SYTO9 and propidium iodide*. BMC microbiology, 2015. **15**(1): p. 1-9.
76. Ch, D., *On the origin of species by means of natural selection, or the preservation of favoured races in the struggle for life*. London: J. Murray, 1859. **502**.
77. Ma, L.-S., et al., *Agrobacterium tumefaciens deploys a superfamily of type VI secretion DNase effectors as weapons for interbacterial competition in planta*. Cell host & microbe, 2014. **16**(1): p. 94-104.



78. Verster, A.J., et al., *The landscape of type VI secretion across human gut microbiomes reveals its role in community composition*. Cell host & microbe, 2017. **22**(3): p. 411-419. e4.
79. Fu, Y., B.T. Ho, and J.J. Mekalanos, *Tracking Vibrio cholerae cell-cell interactions during infection reveals bacterial population dynamics within intestinal microenvironments*. Cell host & microbe, 2018. **23**(2): p. 274-281. e2.
80. Perault, A.I., et al., *Host adaptation predisposes Pseudomonas aeruginosa to type VI secretion system-mediated predation by the Burkholderia cepacia complex*. Cell host & microbe, 2020. **28**(4): p. 534-547. e3.
81. Leiman, P.G., et al., *Type VI secretion apparatus and phage tail-associated protein complexes share a common evolutionary origin*. Proceedings of the National Academy of Sciences, 2009. **106**(11): p. 4154-4159.
82. Veesler, D. and C. Cambillau, *A common evolutionary origin for tailed-bacteriophage functional modules and bacterial machineries*. Microbiology and Molecular Biology Reviews, 2011. **75**(3): p. 423-433.
83. Zoued, A., et al., *Architecture and assembly of the Type VI secretion system*. Biochimica et Biophysica Acta (BBA)-Molecular Cell Research, 2014. **1843**(8): p. 1664-1673.
84. Russell, A.B., S.B. Peterson, and J.D. Mougous, *Type VI secretion system effectors: poisons with a purpose*. Nature reviews microbiology, 2014. **12**(2): p. 137-148.
85. Gerc, A.J., et al., *Visualization of the serratia type VI secretion system reveals unprovoked attacks and dynamic assembly*. Cell reports, 2015. **12**(12): p. 2131-2142.
86. Allsopp, L.P., et al., *Causalities of war: the connection between type VI secretion system and microbiota*. Cellular microbiology, 2020. **22**(3): p. e13153.
87. Speare, L., et al., *A Putative Lipoprotein Mediates Cell-Cell Contact for Type VI Secretion System-Dependent Killing of Specific Competitors*. Mbio, 2022. **13**(2): p. e03085-21.
88. Mariano, G., et al., *A family of Type VI secretion system effector proteins that form ion-selective pores*. Nature communications, 2019. **10**(1): p. 1-15.
89. Gallegos-Monterrosa, R. and S.J. Coulthurst, *The ecological impact of a bacterial weapon: microbial interactions and the Type VI secretion system*. FEMS Microbiology Reviews, 2021. **45**(6): p. fuab033.
90. Basler, á., et al., *Type VI secretion requires a dynamic contractile phage tail-like structure*. Nature, 2012. **483**(7388): p. 182-186.
91. Borgeaud, S., et al., *The type VI secretion system of Vibrio cholerae fosters horizontal gene transfer*. Science, 2015. **347**(6217): p. 63-67.
92. Ringel, P.D., D. Hu, and M. Basler, *The role of type VI secretion system effectors in target cell lysis and subsequent horizontal gene transfer*. Cell reports, 2017. **21**(13): p. 3927-3940.

93. Thomas, J., et al., *Horizontal gene transfer of functional type VI killing genes by natural transformation*. MBio, 2017. **8**(4): p. e00654-17.
94. Lin, L., et al., *Abundance of bacterial Type VI secretion system components measured by targeted proteomics*. Nature communications, 2019. **10**(1): p. 1-11.
95. Vettiger, A. and M. Basler, *Type VI secretion system substrates are transferred and reused among sister cells*. Cell, 2016. **167**(1): p. 99-110. e12.
96. Pissaridou, P., et al., *The Pseudomonas aeruginosa T6SS-VgrG1b spike is topped by a PAAR protein eliciting DNA damage to bacterial competitors*. Proceedings of the National Academy of Sciences, 2018. **115**(49): p. 12519-12524.
97. Navarro-Garcia, F., et al., *Type VI secretion system in pathogenic Escherichia coli: structure, role in virulence, and acquisition*. Frontiers in microbiology, 2019. **10**: p. 1965.
98. Cianfanelli, F.R., L. Monlezun, and S.J. Coulthurst, *Aim, load, fire: the type VI secretion system, a bacterial nanoweapon*. Trends in microbiology, 2016. **24**(1): p. 51-62.
99. Wong, M.J., et al., *Microbial herd protection mediated by antagonistic interaction in polymicrobial communities*. Applied and environmental microbiology, 2016. **82**(23): p. 6881-6888.
100. McNally, L., et al., *Killing by Type VI secretion drives genetic phase separation and correlates with increased cooperation*. Nature communications, 2017. **8**(1): p. 1-11.
101. Speare, L., et al., *Host-Like Conditions Are Required for T6SS-Mediated Competition among Vibrio fischeri Light Organ Symbionts*. Msphere, 2021. **6**(4): p. e01288-20.
102. Wu, C.F., et al., *Effector loading onto the VgrG carrier activates type VI secretion system assembly*. EMBO reports, 2020. **21**(1): p. e47961.
103. Unterweger, D., et al., *The Vibrio cholerae type VI secretion system employs diverse effector modules for intraspecific competition*. Nature communications, 2014. **5**(1): p. 1-9.
104. Volfson, D., et al., *Biomechanical ordering of dense cell populations*. Proceedings of the National Academy of Sciences, 2008. **105**(40): p. 15346-15351.
105. Short, M.B., et al., *A statistical model of criminal behavior*. Mathematical Models and Methods in Applied Sciences, 2008. **18**(supp01): p. 1249-1267.
106. Volkening, A. and B. Sandstede, *Modelling stripe formation in zebrafish: an agent-based approach*. Journal of the Royal Society Interface, 2015. **12**(112): p. 20150812.
107. Ghosh, P., et al., *Mechanically-driven phase separation in a growing bacterial colony*. Proceedings of the National Academy of Sciences, 2015. **112**(17): p. E2166-E2173.
108. Jayathilake, P.G., et al., *A mechanistic Individual-based Model of microbial communities*. PloS one, 2017. **12**(8): p. e0181965.
109. Acemel, R.D., F. Govantes, and A. Cuetos, *Computer simulation study of early bacterial biofilm development*. Scientific reports, 2018. **8**(1): p. 1-9.

110. Glen, C.M., M.L. Kemp, and E.O. Voit, *Agent-based modeling of morphogenetic systems: Advantages and challenges*. PLoS computational biology, 2019. **15**(3): p. e1006577.
111. Borenstein, D.B., et al., *Established microbial colonies can survive type VI secretion assault*. PLoS computational biology, 2015. **11**(10): p. e1004520.
112. Wilmoth, J.L., et al., *A microfluidics and agent-based modeling framework for investigating spatial organization in bacterial colonies: the case of Pseudomonas aeruginosa and H1-Type VI secretion interactions*. Frontiers in microbiology, 2018. **9**: p. 33.
113. Smith, W.P., et al., *The evolution of tit-for-tat in bacteria via the type VI secretion system*. Nature communications, 2020. **11**(1): p. 1-11.
114. Bernard, C.S., et al., *Nooks and crannies in type VI secretion regulation*. Journal of bacteriology, 2010. **192**(15): p. 3850-3860.
115. Clemens, D.L., et al., *Atomic structure of T6SS reveals interlaced array essential to function*. Cell, 2015. **160**(5): p. 940-951.
116. Lazzaro, M., M.F. Feldman, and E. García Vescovi, *A transcriptional regulatory mechanism finely tunes the firing of type VI secretion system in response to bacterial enemies*. MBio, 2017. **8**(4): p. e00559-17.
117. Saak, C.C., M.A. Zepeda-Rivera, and K.A. Gibbs, *A single point mutation in a TssB/VipA homolog disrupts sheath formation in the type VI secretion system of Proteus mirabilis*. PLoS One, 2017. **12**(9): p. e0184797.
118. Rigney, D.R., *Stochastic model of constitutive protein levels in growing and dividing bacterial cells*. Journal of Theoretical Biology, 1979. **76**(4): p. 453-480.
119. Paulsson, J., *Models of stochastic gene expression*. Physics of life reviews, 2005. **2**(2): p. 157-175.
120. Rudnicki, R. and A. Tomsaki, *On a stochastic gene expression with pre-mRNA, mRNA and protein contribution*. Journal of Theoretical Biology, 2015. **387**: p. 54-67.
121. Thattai, M., *Universal Poisson statistics of mRNAs with complex decay pathways*. Biophysical journal, 2016. **110**(2): p. 301-305.
122. Mukherji, S. and E.K. O'Shea, *Mechanisms of organelle biogenesis govern stochastic fluctuations in organelle abundance*. Elife, 2014. **3**: p. e02678.
123. Amir, A., *Cell size regulation in bacteria*. Physical review letters, 2014. **112**(20): p. 208102.
124. Gupta, S., et al., *The cost of bacterial predation via type VI secretion system leads to predator extinction under environmental stress*. Iscience, 2021. **24**(12): p. 103507.
125. Manera, K., et al., *Sensing of intracellular Hcp levels controls T6SS expression in Vibrio cholerae*. Proceedings of the National Academy of Sciences, 2021. **118**(25): p. e2104813118.

126. Toska, J., B.T. Ho, and J.J. Mekalanos, *Exopolysaccharide protects Vibrio cholerae from exogenous attacks by the type 6 secretion system*. Proceedings of the National Academy of Sciences, 2018. **115**(31): p. 7997-8002.
127. Hersch, S.J., et al., *Envelope stress responses defend against type six secretion system attacks independently of immunity proteins*. Nature microbiology, 2020. **5**(5): p. 706-714.
128. Le, N.-H., et al., *Peptidoglycan editing provides immunity to Acinetobacter baumannii during bacterial warfare*. Science Advances, 2020. **6**(30): p. eabb5614.
129. Crisan, C.V., et al., *Glucose confers protection to Escherichia coli against contact killing by Vibrio cholerae*. Scientific reports, 2021. **11**(1): p. 1-11.
130. Veening, J.-W., W.K. Smits, and O.P. Kuipers, *Bistability, epigenetics, and bet-hedging in bacteria*. Annual review of microbiology, 2008. **62**(1): p. 193-210.
131. Losick, R. and C. Desplan, *Stochasticity and cell fate*. science, 2008. **320**(5872): p. 65-68.
132. Pájaro, M., et al., *Transient hysteresis and inherent stochasticity in gene regulatory networks*. Nature communications, 2019. **10**(1): p. 1-7.
133. Stabb, E.V., K.A. Reich, and E.G. Ruby, *Vibrio fischeri genes hvnA and hvnB encode secreted NAD<sup>+</sup>-glycohydrolases*. Journal of Bacteriology, 2001. **183**(1): p. 309-317.
134. Smith, S. and A.N. Septer, *Quantification of Interbacterial Competition using Single-Cell Fluorescence Imaging*. JoVE (Journal of Visualized Experiments), 2021(175): p. e62851.
135. Sachs, J.L., R.G. Skophammer, and J.U. Regus, *Evolutionary transitions in bacterial symbiosis*. Proceedings of the National Academy of Sciences, 2011. **108**(supplement\_2): p. 10800-10807.
136. Cury, J., M. Touchon, and E.P. Rocha, *Integrative and conjugative elements and their hosts: composition, distribution and organization*. Nucleic acids research, 2017. **45**(15): p. 8943-8956.
137. Juhas, M., D.W. Crook, and D.W. Hood, *Type IV secretion systems: tools of bacterial horizontal gene transfer and virulence*. Cellular microbiology, 2008. **10**(12): p. 2377-2386.
138. Sørensen, S.J., et al., *Studying plasmid horizontal transfer in situ: a critical review*. Nature Reviews Microbiology, 2005. **3**(9): p. 700-710.
139. Cabezón, E., et al., *Towards an integrated model of bacterial conjugation*. FEMS microbiology reviews, 2015. **39**(1): p. 81-95.
140. Firth, N., K. Ippen-Ihler, and R.A. Skurray, *Structure and function of the F factor and mechanism of conjugation*. Escherichia coli and Salmonella: cellular and molecular biology, 2nd ed. ASM Press, Washington, DC, 1996: p. 2377-2401.
141. Parsons, L.M., C.S. Jankowski, and K.M. Derbyshire, *Conjugal transfer of chromosomal DNA in Mycobacterium smegmatis*. Molecular microbiology, 1998. **28**(3): p. 571-582.

142. Wang, J., et al., *Chromosomal DNA transfer in Mycobacterium smegmatis is mechanistically different from classical Hfr chromosomal DNA transfer*. Molecular microbiology, 2005. **58**(1): p. 280-288.
143. Wang, J., L.M. Parsons, and K.M. Derbyshire, *Unconventional conjugal DNA transfer in mycobacteria*. Nature genetics, 2003. **34**(1): p. 80-84.
144. Gray, T.A., et al., *Distributive conjugal transfer in mycobacteria generates progeny with meiotic-like genome-wide mosaicism, allowing mapping of a mating identity locus*. PLoS biology, 2013. **11**(7): p. e1001602.
145. Ochman, H. and N.A. Moran, *Genes lost and genes found: evolution of bacterial pathogenesis and symbiosis*. Science, 2001. **292**(5519): p. 1096-1099.
146. Finan, T.M., *Evolving insights: symbiosis islands and horizontal gene transfer*. Journal of bacteriology, 2002. **184**(11): p. 2855.
147. Nakamura, Y., et al., *Biased biological functions of horizontally transferred genes in prokaryotic genomes*. Nature genetics, 2004. **36**(7): p. 760-766.
148. McFall-Ngai, M.J., *The importance of microbes in animal development: lessons from the squid-vibrio symbiosis*. Annual review of microbiology, 2014. **68**: p. 177-194.
149. Nyholm, S.V. and M. McFall-Ngai, *The winnowing: establishing the squid–vibrio symbiosis*. Nature Reviews Microbiology, 2004. **2**(8): p. 632-642.
150. Jones, B. and M. Nishiguchi, *Counterillumination in the hawaiian bobtail squid, Euprymna scolopes Berry (Mollusca: Cephalopoda)*. Marine Biology, 2004. **144**(6): p. 1151-1155.
151. Yip, E.S., et al., *The symbiosis regulator RscS controls the syp gene locus, biofilm formation and symbiotic aggregation by Vibrio fischeri*. Molecular microbiology, 2006. **62**(6): p. 1586-1600.
152. Pankey, M.S., et al., *Host-selected mutations converging on a global regulator drive an adaptive leap towards symbiosis in bacteria*. Elife, 2017. **6**.
153. Boettcher, K.J. and E.G. Ruby, *Occurrence of plasmid DNA in the sepiolid squid symbiont Vibrio fischeri*. Current Microbiology, 1994. **29**: p. 279-286.
154. Ruby, E.G., et al., *Complete genome sequence of Vibrio fischeri: a symbiotic bacterium with pathogenic congeners*. Proceedings of the National Academy of Sciences, 2005. **102**(8): p. 3004-3009.
155. Gross, J.D. and L. Caro, *Genetic Transfer in Bacterial Mating: What mechanism insures the orderly transfer of DNA from donor to recipient cells?* Science, 1965. **150**(3704): p. 1679-1684.
156. Adin, D.M., K.L. Visick, and E.V. Stabb, *Identification of a cellobiose utilization gene cluster with cryptic  $\beta$ -galactosidase activity in Vibrio fischeri*. Applied and environmental microbiology, 2008. **74**(13): p. 4059-4069.

157. Wollman, E.-L., F. Jacob, and W. Hayes. *Conjugation and genetic recombination in Escherichia coli K-12*. in *Cold Spring Harbor symposia on quantitative biology*. 1956. Cold Spring Harbor Laboratory Press.
158. Stabb, E.V. and E.G. Ruby, *RP4-based plasmids for conjugation between Escherichia coli and members of the Vibrionaceae*, in *Methods in enzymology*. 2002, Elsevier. p. 413-426.
159. Herrero, M., V. de Lorenzo, and K.N. Timmis, *Transposon vectors containing non-antibiotic resistance selection markers for cloning and stable chromosomal insertion of foreign genes in gram-negative bacteria*. *Journal of bacteriology*, 1990. **172**(11): p. 6557-6567.
160. Hanahan, D., *Studies on transformation of Escherichia coli with plasmids*. *Journal of molecular biology*, 1983. **166**(4): p. 557-580.
161. Barbieri, E., et al., *Phylogenetic characterization of epibiotic bacteria in the accessory nidamental gland and egg capsules of the squid Loligo pealei (Cephalopoda: Loliginidae)*. *Environmental Microbiology*, 2001. **3**(3): p. 151-167.
162. Collins, A.J., et al., *Diversity and partitioning of bacterial populations within the accessory nidamental gland of the squid Euprymna scolopes*. *Applied and environmental microbiology*, 2012. **78**(12): p. 4200-4208.
163. Kaufman, M.R., et al., *Bacterial symbionts colonize the accessory nidamental gland of the squid Loligo opalescens via horizontal transmission*. *The Biological Bulletin*, 1998. **194**(1): p. 36-43.
164. Bloodgood, R.A., *The squid accessory nidamental gland: ultrastructure and association with bacteria*. *Tissue and cell*, 1977. **9**(2): p. 197-208.
165. Kerwin, A.H. and S.V. Nyholm, *Symbiotic bacteria associated with a bobtail squid reproductive system are detectable in the environment, and stable in the host and developing eggs*. *Environmental microbiology*, 2017. **19**(4): p. 1463-1475.
166. Kerwin, A.H., et al., *Shielding the next generation: symbiotic bacteria from a reproductive organ protect bobtail squid eggs from fungal fouling*. *MBio*, 2019. **10**(5): p. e02376-19.
167. Gromek, S.M., et al., *Leisingera sp. JC1, a bacterial isolate from Hawaiian bobtail squid eggs, produces indigoidine and differentially inhibits vibrios*. *Frontiers in microbiology*, 2016. **7**: p. 1342.
168. Moriano-Gutierrez, S., et al., *Critical symbiont signals drive both local and systemic changes in diel and developmental host gene expression*. *Proceedings of the National Academy of Sciences*, 2019. **116**(16): p. 7990-7999.
169. Ford, L.A., et al., *Bacterial populations of normal and ulcerated mantle tissue of the squid, Lolliguncula brevis*. *Journal of invertebrate pathology*, 1986. **48**(1): p. 13-26.
170. Lutz, H.L., et al., *A simple microbiome in the European common cuttlefish, Sepia officinalis*. *Msystems*, 2019. **4**(4): p. e00177-19.

171. Bartol, I., R. Mann, and M. Vecchione, *Distribution of the euryhaline squid Lolliguncula brevis in Chesapeake Bay: effects of selected abiotic factors*. Marine Ecology Progress Series, 2002. **226**: p. 235-247.
172. Laughlin, R.A. and R.J. Livingston, *Environmental and trophic determinants of the spatial/temporal distribution of the brief squid (Lolliguncula brevis) in the Apalachicola estuary (North Florida, USA)*. Bulletin of Marine Science, 1982. **32**(2): p. 489-497.
173. Jackson, G., et al., *Age, growth, and maturation of Lolliguncula brevis (Cephalopoda: Loliginidae) in the northwestern Gulf of Mexico with a comparison of length-frequency versus statolith age analysis*. Canadian Journal of Fisheries and Aquatic Sciences, 1997. **54**(12): p. 2907-2919.
174. Hanlon, R.T., R.F. Hixon, and W.H. Hulet, *Survival, growth, and behavior of the loliginid squids Loligo plei, Loligo pealei, and Lolliguncula brevis (Mollusca: Cephalopoda) in closed sea water systems*. The Biological Bulletin, 1983. **165**(3): p. 637-685.
175. Martins, R.S. and J.A.A. Perez, *The ecology of loliginid squid in shallow waters around Santa Catarina Island, southern Brazil*. Bulletin of Marine Science, 2007. **80**(1): p. 125-145.
176. Gebhardt, K. and T. Knebelsberger, *Identification of cephalopod species from the North and Baltic Seas using morphology, COI and 18S rDNA sequences*. Helgoland Marine Research, 2015. **69**(3): p. 259-271.
177. Nishiguchi, M., J. Lopez, and S.v. Boletzky, *Enlightenment of old ideas from new investigations: more questions regarding the evolution of bacteriogenic light organs in squids*. Evolution & development, 2004. **6**(1): p. 41-49.
178. Anderson, F.E., et al., *Lights out: the evolution of bacterial bioluminescence in Loliginidae*. Hydrobiologia, 2014. **725**(1): p. 189-203.
179. Guerrero-Ferreira, R. and M. Nishiguchi, *Ultrastructure of light organs of loliginid squids and their bacterial symbionts: A novel model system for the study of marine symbioses*. Vie et Milieu (Paris, France: 1980), 2009. **59**(3-4): p. 307.
180. Wollenberg, M. and E. Ruby, *Population structure of Vibrio fischeri within the light organs of Euprymna scolopes squid from two Oahu (Hawaii) populations*. Applied and Environmental Microbiology, 2009. **75**(1): p. 193-202.
181. Fidopiastis, P.M., S. Von Boletzky, and E.G. Ruby, *A new niche for Vibrio logei, the predominant light organ symbiont of squids in the genus Sepiola*. Journal of Bacteriology, 1998. **180**(1): p. 59-64.
182. Margaret J, M.-N., *Consequences of evolving with bacterial symbionts: insights from the squid-vibrio associations*. Annual Review of Ecology and Systematics, 1999. **30**(1): p. 235-256.
183. Septer, A.N., et al., *Draft Genome Sequence of a Harveyi Clade Bacterium Isolated from Lolliguncula brevis Squid*. Microbiology Resource Announcements, 2020. **9**(8): p. e00078-20.

184. Jesser, K.J. and R.T. Noble, *Vibrio ecology in the Neuse River Estuary, North Carolina, characterized by next-generation amplicon sequencing of the gene encoding heat shock protein 60 (hsp60)*. Applied and Environmental Microbiology, 2018. **84**(13): p. e00333-18.
185. King, W.L., et al., *Pearl oyster bacterial community structure is governed by location and tissue-type, but Vibrio species are shared among oyster tissues*. Frontiers in Microbiology, 2021. **12**: p. 723649.
186. King, W.L., et al., *A new high throughput sequencing assay for characterizing the diversity of natural Vibrio communities and its application to a Pacific Oyster mortality event*. Frontiers in Microbiology, 2019. **10**: p. 2907.
187. Kwok, A.Y., et al., *Phylogenetic study and identification of human pathogenic Vibrio species based on partial hsp 60 gene sequences*. Canadian journal of microbiology, 2002. **48**(10): p. 903-910.
188. Hill, J.E., J.R. Town, and S.M. Hemmingsen, *Improved template representation in cpn60 polymerase chain reaction (PCR) product libraries generated from complex templates by application of a specific mixture of PCR primers*. Environmental microbiology, 2006. **8**(4): p. 741-746.
189. McFall-Ngai, M. and M.K. Montgomery, *The anatomy and morphology of the adult bacterial light organ of Euprymna scolopes Berry (Cephalopoda: Sepiolidae)*. The Biological Bulletin, 1990. **179**(3): p. 332-339.
190. Sycuro, L.K., E.G. Ruby, and M. McFall-Ngai, *Confocal microscopy of the light organ crypts in juvenile Euprymna scolopes reveals their morphological complexity and dynamic function in symbiosis*. Journal of Morphology, 2006. **267**(5): p. 555-568.
191. Essock-Burns, T., et al., *Bacterial quorum-sensing regulation induces morphological change in a key host tissue during the Euprymna scolopes-Vibrio fischeri symbiosis*. MBio, 2021. **12**(5): p. e02402-21.
192. Johnsen, S., E.A. Widder, and C.D. Mobley, *Propagation and perception of bioluminescence: factors affecting counterillumination as a cryptic strategy*. The Biological Bulletin, 2004. **207**(1): p. 1-16.
193. Septer, A.N., N.L. Lyell, and E.V. Stabb, *The iron-dependent regulator Fur controls pheromone signaling systems and luminescence in the squid symbiont Vibrio fischeri ES114*. Applied and environmental microbiology, 2013. **79**(6): p. 1826-1834.
194. Lyell, N.L., et al., *Bright mutants of Vibrio fischeri ES114 reveal conditions and regulators that control bioluminescence and expression of the lux operon*. Journal of bacteriology, 2010. **192**(19): p. 5103-5114.
195. Bose, J.L., et al., *Contribution of rapid evolution of the luxR-luxI intergenic region to the diverse bioluminescence outputs of Vibrio fischeri strains isolated from different environments*. Applied and environmental microbiology, 2011. **77**(7): p. 2445-2457.
196. Hall, M. and R.G. Beiko, *16S rRNA gene analysis with QIIME2*. Microbiome analysis: methods and protocols, 2018: p. 113-129.



197. Estaki, M., et al., *QIIME 2 enables comprehensive end-to-end analysis of diverse microbiome data and comparative studies with publicly available data*. Current protocols in bioinformatics, 2020. **70**(1): p. e100.
198. Callahan, B.J., et al., *DADA2: High-resolution sample inference from Illumina amplicon data*. Nature methods, 2016. **13**(7): p. 581-583.
199. Dubois, B., et al., *A detailed workflow to develop QIIME2-formatted reference databases for taxonomic analysis of DNA metabarcoding data*. BMC Genomic Data, 2022. **23**(1): p. 53.
200. Hill, J.E., et al., *cpnDB: a chaperonin sequence database*. Genome research, 2004. **14**(8): p. 1669-1675.
201. Vancuren, S.J. and J.E. Hill, *Update on cpnDB: a reference database of chaperonin sequences*. Database, 2019. **2019**.
202. Bokulich, N.A., et al., *Optimizing taxonomic classification of marker gene amplicon sequences*. PeerJ Preprints, 2018. **6**: p. e3208v2.
203. McMurdie, P.J. and S. Holmes, *phyloseq: an R package for reproducible interactive analysis and graphics of microbiome census data*. PloS one, 2013. **8**(4): p. e61217.
204. Birks, H.J.B. and J. Line, *The use of rarefaction analysis for estimating palynological richness from Quaternary pollen-analytical data*. The Holocene, 1992. **2**(1): p. 1-10.
205. Weiss, S., et al., *Normalization and microbial differential abundance strategies depend upon data characteristics*. Microbiome, 2017. **5**: p. 1-18.
206. McMurdie, P.J. and S. Holmes, *Waste not, want not: why rarefying microbiome data is inadmissible*. PLoS computational biology, 2014. **10**(4): p. e1003531.
207. Bartol, I.K., M.R. Patterson, and R. Mann, *Swimming mechanics and behavior of the shallow-water brief squid Lolliguncula brevis*. Journal of Experimental Biology, 2001. **204**(21): p. 3655-3682.
208. Wells, M., et al., *Respiratory and cardiac performance in Lolliguncula brevis (Cephalopoda, Myopsida): the effects of activity, temperature and hypoxia*. Journal of Experimental Biology, 1988. **138**(1): p. 17-36.
209. McCormick, L.R. and J.H. Cohen, *Pupil light reflex in the Atlantic brief squid, Lolliguncula brevis*. Journal of Experimental Biology, 2012. **215**(15): p. 2677-2683.
210. Hanlon, R.T., *Maintenance, rearing, and culture of teuthoid and sepioid squids*, in *Squid as experimental animals*. 1990, Springer. p. 35-62.
211. Zablotowicz, R.M. and K.N. Reddy, *Impact of glyphosate on the Bradyrhizobium japonicum symbiosis with glyphosate-resistant transgenic soybean: a minireview*. Journal of Environmental Quality, 2004. **33**(3): p. 825-831.

212. Hennecke, H., *Nitrogen fixation genes involved in the Bradyrhizobium japonicum-soybean symbiosis*. FEBS letters, 1990. **268**(2): p. 422-426.
213. Meena, R.S., et al., *Response and interaction of Bradyrhizobium japonicum and arbuscular mycorrhizal fungi in the soybean rhizosphere*. Plant Growth Regulation, 2018. **84**: p. 207-223.